

Dielectric Actuation Techniques at the Nanoscale: Piezoelectricity and Flexoelectricity

Thèse N° 7238

Présentée le 19 décembre 2019

à la Faculté des sciences et techniques de l'ingénieur
Laboratoire de systèmes nano-électromécaniques
Programme doctoral en microsystemes et microélectronique

pour l'obtention du grade de Docteur ès Sciences

par

Kaitlin Marie HOWELL

Acceptée sur proposition du jury

Dr D. Briand, président du jury
Prof. L. G. Villanueva Torrijo, directeur de thèse
Dr M. Moridi, rapporteur
Prof. G. Catalan, rapporteur
Prof. N. Quack, rapporteur

2019

Knowledge is power... Knowledge is happiness.
— Thomas Jefferson

To my mother, my father and, last but certainly not least, my husband. . .

Acknowledgements

Completing a PhD is similar to a journey: the destination is only part of the equation. When I started this adventure, I had no idea how much it would shape my life and who I am. Having passed the crucible, I find that I am the better for it; however, I would never have made it this far without the many who supported me in my brightest and darkest hours.

This PhD would not have been possible without the support and advice of my thesis director Guillermo, with whom I laughed, cried and sometimes discussed scientific work with. Thank you for having confidence in me, especially when I didn't.

My lab mates are equally deserving of thanks, both for their scientific assistance as well as fun moments eating raclette and beating Guillermo at laser tag. The long hours in the cleanroom and office were easier to when sharing them with you. To Annalisa, Andrea, Damien, Faizan, Marsha, Marco, Shirin, Soumya and Tom, thank you for everything.

I supervised several fantastic master students during my PhD and am eternally grateful to them for their hard work and laughing at my bad jokes. Elliot, Giulio, Roman, Silvan and Tamara, thank you for your time and energy!

Whenever I found myself overwhelmed by my lack of knowledge in material science, I could count on the members of the former Ceramics Laboratory to come to my aid. I want to thank Dragan and Robin in particular for explaining the nuances of dielectrics, ferroelectrics and everything in-between.

None of the fabrication for my PhD would have been possible without the support and advice from the CMi staff. Thank you for helping me at all hours of the day and your patience with my many, many questions.

During my six years at EPFL, I've been lucky enough to meet so many people that I can call my friends. Shout out to my PhD Rep buddies, including Arnaud, Leo, Margaux, Samuel and Vivek, as well as my bouldering/climbing friends, including Chris, Lorenz and Matthieu. To my girlfriends, including Francesca, Irene and Soumya, thanks for the fun evenings eating and drinking together! To Clemens and Stee, thanks for the fantastic conversations about science, politics and Star Wars.

My PhD is dedicated in part to my family, in particular my mom and dad, who supported me from afar and whenever we could be together. It hasn't been easy sometimes but you all were and continue to be my bedrock. I love you all.

During my PhD, I overcome my hesitation in dating an office mate and fell in love with the man who has become my life partner. This PhD is also dedicated to Samuel Howell, for his continual support and faith in myself through thick and thin. Thank you for being you.

Abstract

Micro- and nanoelectromechanical systems (MEMS/NEMS) have long shown their potential to disrupt the established technologies. Over the past 15 years, MEMS have become fundamental components in filters, accelerometers, gyroscopes and gas sensors. MEMS are now an essential part of most of the electronic devices we own. However, their smaller counterpart, NEMS, are still far from industrialization due to two challenges: their fabrication and the transduction of their motion.

One transduction technique to control the motion of NEMS is piezoelectricity, which can be directly integrated, has low power consumption and exhibits linear transduction. Piezoelectric aluminum nitride (AlN) deposited by reactive sputtering has been applied in several MEMS applications and recently in NEMS. There is a good understanding of the sputtering parameters and substrate conditions needed to fabricate high quality micrometer thick AlN films, but less is known for nanometer thick films.

One part of the thesis was focused on the impact of reactive sputtering parameters and substrate conditions on the c-axis texture and piezoelectric coefficients of 50-100 nm thick AlN films. We found that substrate temperature, sputtering power and type as well as quality of substrate have a strong impact on AlN c-axis texture. By optimizing these conditions, we were able to fabricate 50 nm thick AlN films with crystalline and piezoelectric properties similar to micrometer thick films. Recently, AlN doped with scandium (AlScN) has been developed due to its larger piezoelectric coefficients compared to undoped AlN. We found a strong influence of two sputtering parameters, argon gas concentration and substrate bias, on the c-axis texture and density of abnormal grains in 1 micrometer thick $\text{Al}_{0.6}\text{Sc}_{0.4}\text{N}$ films.

A fundamental issue in piezoelectric NEMS is that an asymmetric thickness cross section is necessary to create a flexural curvature and the asymmetry will reduce with decreasing system thickness. To avoid this issue, an alternative transduction technique based on flexoelectricity can be implemented, which has three advantages over piezoelectricity: it is theorized to exist in all dielectrics, it is predicted that its coefficients do not decrease with decreasing film thickness and any thickness cross section can be used to fabricate flexural NEMS.

Most experimental work in flexoelectricity has been on ferroelectric or paraelectric materials; little research has been conducted on materials like CMOS-compatible, high-k dielectrics which could replace piezoelectric thin films in NEMS. Therefore, another part of this thesis focused on the fabrication and characterization of flexoelectric actuators based on amorphous hafnium oxide (HfO_2). The fabricated 40 nm thick HfO_2 films were non-ferroelectric and an effective flexoelectric coefficient of 37 pC/m was measured.

Abstract

The final part of the thesis analyzed the potential curvature generation of piezoelectric and flexoelectric films with nanoscale thicknesses, as well as provided a better understanding of the relationship between experimental flexoelectric coefficients and relative permittivity. Based on these analyses, we envision that flexoelectric thin films based on high-k dielectric materials with relative permittivities between 50-100 are a promising alternative to piezoelectric thin films in nanoscale actuation.

Keywords: NEMS, Piezoelectricity, Flexoelectricity, Hafnium Oxide, High-K Dielectrics, Aluminum Nitride, Aluminum Scandium Nitride, Sputtering, Actuators, Microfabrication

Résumé

Les systèmes micro- et nano-électromécaniques (MEMS/NEMS) ont depuis longtemps démontré leur capacité à surpasser les technologies établies. Durant les 15 dernières années, les MEMS sont devenus des composants importants dans les filtres, accéléromètres, gyroscopes, ou encore capteurs de gaz. Ils sont dorénavant présents dans la plupart des appareils électroniques de tout un chacun. Néanmoins, leur équivalent à l'échelle nanométrique, les NEMS, sont encore loin d'une production à grande échelle pour deux raisons : leur fabrication et la transduction de leur mouvement.

Une technique de transduction pour contrôler le mouvement des NEMS est la piézoélectricité, qui peut être intégrée directement dans le système, consomme peu d'énergie et démontre un comportement linéaire. Le nitrure d'aluminium (AlN) piézoélectrique déposé par pulvérisation réactive est déjà appliqué à plusieurs applications MEMS, et plus récemment aussi aux NEMS. Les paramètres de pulvérisation, ainsi que les conditions nécessaires au niveau du substrat sont bien maîtrisés pour la fabrication de couches d'AlN à l'échelle micrométrique mais moins est connues pour des couches nanométriques.

Une partie de cette thèse se concentre sur l'impact des paramètres de pulvérisation réactive et des conditions du substrat sur la texture axe-c et les coefficients piézoélectriques pour des couches d'AlN d'une épaisseur de 50 à 100 nm. Nous avons découvert que la température du substrat, la puissance et le type ainsi que la qualité du substrat ont un effet important sur la texture axe-c de l'AlN. Suite à une optimisation des différents paramètres, nous avons été capables de fabriquer des couches d'AlN de 50 nm d'épais avec des propriétés cristallines et piézoélectriques similaires à celles des couches d'échelles micrométriques. Récemment, l'AlN dopé avec du scandium (AlScN) a été développé en raison de ses coefficients piézoélectriques plus élevés que l'AlN non dopé. Nous avons découvert une influence importante de deux paramètres de pulvérisation, la concentration d'argon et la polarisation du substrat, sur la texture axe-c et la densité de grains irréguliers dans des couches épaisses d' $\text{Al}_{0.6}\text{Sc}_{0.4}\text{N}$ de 1 micrometer.

Un problème fondamental dans les NEMS piézoélectriques est la section transversale asymétrique nécessaire pour créer une courbure en flexion. Cette asymétrie va diminuer lorsque l'épaisseur de la couche du système est réduite. Afin d'éviter ce problème, un mode de transduction alternatif peut être implémenté : il s'agit de la flexoélectricité, qui a trois avantages sur la piézoélectricité : elle existe en théorie dans tous les matériaux diélectriques, il est prédit que ses coefficients ne sont pas altérés par une réduction de l'épaisseur de la couche, et toutes les épaisseurs de la section transversales peuvent servir pour la fabrication de NEMS en flexion.

L'essentiel des travaux expérimentaux sur la flexoélectricité a été développé sur les matériaux ferroélectriques et paraélectriques; peu de recherche a été conduite sur des matériaux compatibles CMOS tels que les diélectriques high-k, qui pourraient remplacer les fines couches piézoélectriques dans les NEMS. Pour cette raison, une autre partie de cette thèse se concentre sur la fabrication et caractérisation d'actuateurs flexoélectriques basés sur l'oxyde d'hafnium (HfO_2) amorphe. Les couches d' HfO_2 fabriquées étaient épaisses de 40 nm, non ferroélectriques, et leurs mesures ont indiqué un coefficient flexoélectrique effectif de 37 pC/m.

La partie finale de cette thèse a analysé la génération de courbure de couches piézoélectriques et flexoélectriques de dimensions nanométriques, et offre une meilleure compréhension de la relation entre les coefficients flexoélectriques expérimentaux et la permittivité relative. En nous basant sur ces résultats, nous envisageons que les fines couches flexoélectriques fabriquées avec des matériaux diélectriques high-k (permittivité relative entre 50 et 100) seront une alternative prometteuse aux fines couches piézoélectriques pour l'actuation à l'échelle nanométrique.

Mots clés : NEMS, piézoélectricité, flexoélectricité, oxyde d'hafnium, diélectriques high-k, nitrure d'aluminium, nitrure d'aluminium scandium, pulvérisation, actuateurs, micro-fabrication.

Zusammenfassung

Seit geraumer Zeit haben Mikro- und Nano-Elektromechanische Systeme (MEMS/NEMS) ihr Vermögen bewiesen, etablierten Technologien weit überlegen zu sein. Insbesondere haben sich während der letzten 15 Jahre MEMS Komponenten in Filtern, Beschleunigungssensoren und Gassensoren als wichtige Bestandteile durchgesetzt, und sind heute in elektronischen Geräten allgegenwärtig. NEMS hingegen - das miniaturisierte Pendant zu MEMS - sind aus folgenden Gründen noch weit von der Marktreife entfernt: herausfordernde Herstellung hochqualitativer Dünnschichten und Schwierigkeiten zur effizienten Bewegungsübertragung. Zur Bewegungsübertragung in NEMS wird häufig der piezoelektrische Effekt benutzt. Direkte Integration, niedriger Leistungsverbrauch und Linearität zwischen elektrischer Spannung und mechanischer Bewegung machen piezoelektrische Aktoren attraktiv. Das wohl meistbenutzte Material ist durch reaktive Kathodenzerstäubung abgeschiedenes Aluminiumnitrid (AlN). Während die Herstellung dicker AlN Filme mit hoher Qualität eine etablierte Technologie ist, gibt es wenig Forschungsarbeit zur Herstellung und Charakterisierung von Dünnschichten. Ein Teil dieser Doktorarbeit beschäftigt sich deshalb mit dem Einfluss der Beschichtungsparameter und der Wahl des Substratmaterials auf die Textur der c-Achse und den piezoelektrischen Koeffizienten von AlN Dünnschichten unter 100 nm. Systematische Untersuchungen ergaben, dass die Substrattemperatur, die eingespeiste Leistung der Kathodenzerstäubung sowie das Material des Substrates einen bedeutenden Einfluss auf die AlN c-Achsen Textur haben. Mittels Optimierung dieser Parameter war es möglich 50 nm dicke kristalline AlN Schichten mit piezoelektrischen Eigenschaften ähnlich denen von Mikrometer dicken Schichten herzustellen. Scandium-dopiertes AlN (AlScN) hat kürzlich grosses Interesse hervorgerufen, weil es einen vergleichsweise hohen piezoelektrischen Koeffizienten aufweist. Untersuchungen zeigten einen starken Einfluss des Gasflusses und Substratbias auf die Textur der c-Achse und Dichte von fehlerhaften Kristallkörner in 1 Mikrometer dicken $\text{Al}_{0.6}\text{Sc}_{0.4}\text{N}$ Filmen. Trotzdem, ein entscheidender Nachteil von piezoelektrischen NEMS ist die Notwendigkeit eines asymmetrischen Schichtbaus um eine Biegung des Aktors zu erzeugen. Mit abnehmender Dicke des Aktors, verringert sich jedoch die Wirkung der Asymmetrie. Der flexoelektrische Effekt bietet eine Alternative zum piezoelektrischen Effekt mit einigen Vorteilen in NEMS: er ist in allen dielektrischen Materialien vorhanden, der flexoelektrische Koeffizient bleibt gleich mit abnehmender Schichtdicke und es benötigt keine Asymmetrie im Schichtaufbau um eine Biegung zu erzeugen. Bis anhin wurde nur wenig Forschung an CMOS-kompatiblen high-k Dielektrika betrieben. Daher befasst sich der zweite Teil dieser Arbeit mit der Herstellung und Charakterisierung

Zusammenfassung

flexoelektrischer Aktoren basierend auf CMOS-kompatiblen, amorphem Hafniumdioxid (HfO_2). Wichtige Erkenntnisse unserer Untersuchungen sind, dass die hergestellten 40 nm dicken HfO_2 Schichten nicht ferroelektrisch sind und dass ein effektiver flexoelektrischer Koeffizient von 37 pC/m gemessen wurde.

Im letzten Teil der Arbeit wurde die Biegungserzeugung von verschiedenen piezoelektrischen und flexoelektrischen Dünnschichten für NEMS verglichen, um die Beziehung zwischen den experimentell gemessenen flexoelektrischen Koeffizienten und der relativen Permittivität besser zu verstehen. Basierend auf dieser Analyse, sehen wir flexoelektrische Dünnschichten basierend auf high-k Dielektrika mit relativen Permittivitäten zwischen 50-100 als eine vielversprechende Alternative zu piezoelektrischen Dünnschichten für die Bewegungserzeugung im Nanometer Bereich.

Stichwörter: NEMS, Piezoelektrizität, Flexoelektrizität, High-K Dielektrika, Hafniumdioxid, Aluminiumnitrid, Aluminiumscandiumnitrid, kathodenzerstäubung, Aktor, Mikrofabrikation

Contents

Acknowledgements	i
Abstract	iii
Table of Contents	xi
List of Figures	xiv
List of Tables	xv
1 Introduction	1
1.1 Piezoelectric Thin Films for NEMS	2
1.1.1 Piezoelectricity and Piezoelectric Materials	2
1.1.2 Sputtering Technique and Sputtered Thin Film Structure	5
1.1.3 Characterization of Piezoelectric Thin Films	7
1.1.4 AlN Thin Films and Piezoelectric Applications	8
1.1.5 AlN Reactive Sputtering Optimization	11
1.1.6 Conclusion on AlN Reactive Sputtering Optimization	16
1.1.7 AlScN Thin Films and Piezoelectric Applications	16
1.1.8 AlScN Reactive Sputtering Optimization	18
1.1.9 Conclusion on AlScN Reactive Sputtering Optimization	20
1.1.10 Sub-100 nm AlN and AlScN Thin Films for Nanoscale Transduction	21
1.2 Flexoelectric Thin Films for NEMS	22
1.2.1 Theory of the Flexoelectric Effect	22
1.2.2 Experimental Characterization of the Flexoelectric Effect	24
1.2.3 Flexoelectric Transduction as an Alternative to Piezoelectric Transduction	27
1.3 Outline of Thesis	28
2 Sputtering Optimization of AlN and Al_{0.6}Sc_{0.4}N Thin Films	31
2.1 Material Characterization Techniques	31
2.1.1 X-Ray Diffraction	31
2.1.2 Thin Film Residual Stress	33
2.1.3 Film Thickness and Crystal Texture	33
2.2 AlN Deposition Experiments	34
2.2.1 Influence of Sputtering Machine Parameters on AlN C-Axis Texture	35

Contents

2.2.2	Influence of Seed Layers on AlN C-Axis Texture and Piezoelectric Response	37
2.2.3	Influence of Substrate and Sputtering System on AlN Rocking Curve FWHM	40
2.2.4	Conclusions on AlN Sputtering Optimization	42
2.3	Al _{0.6} Sc _{0.4} N Deposition Experiments	43
2.3.1	Impact of Ar Gas Concentration and Substrate Bias on Al _{0.6} Sc _{0.4} N Film Properties	43
2.3.2	Study on Columnar Grain Texture and Density of Abnormal Grains	47
2.3.3	Conclusions on Al _{0.6} Sc _{0.4} N Sputtering Optimization	49
2.3.4	Etch Tests on Al _{0.6} Sc _{0.4} N Thin Films	50
2.4	Conclusion	51
3	Flexoelectric Actuators Based on Amorphous HfO₂	53
3.1	Motivation for Flexoelectric Actuation with High-K Dielectrics	53
3.2	Fabrication	54
3.2.1	Process Flow	54
3.2.2	Mask Design	56
3.2.3	Bottom Mo Electrode Liftoff	57
3.2.4	HfO ₂ and Top Mo Electrode Deposition and Patterning	58
3.2.5	Electrode Pad Liftoff and Dicing	59
3.2.6	Fabrication Issues during Wafer Level Fabrication	59
3.2.7	Patterning and Release of Flexoelectric Actuators	61
3.2.8	Fencing During Chip Level Fabrication	62
3.3	Fabrication Results	63
3.3.1	Run 1	63
3.3.2	Run 2	64
3.3.3	Run 3	66
3.4	Electrical Characterization	67
3.4.1	DC Measurements	67
3.4.2	Capacitance and Polarization Measurements	69
3.5	Crystallographic Characterization	71
3.6	Flexoelectric Coefficient Characterization	72
3.6.1	Experimental Setup	72
3.6.2	Method to Measure the Flexoelectric Actuators	73
3.6.3	Flexoelectric Coefficient Analysis	76
3.7	Conclusion	80
4	Discussion and Conclusion	81
4.1	Sputtering Optimization of AlN And Al _{0.6} Sc _{0.4} N Thin Films	81
4.2	Flexoelectric Actuation with Amorphous HfO ₂	83
4.3	Analysis of Relationship Between Experimental Flexoelectric Coefficients from Literature and Relative Permittivity	84
4.4	Piezoelectric versus Flexoelectric Curvature Generation at the Nanoscale	87
4.5	Conclusion	91

A Appendix	93
A.1 Supplementary Formulas	94
A.1.1 Flexural Rigidity	94
A.1.2 Residual Stress Calculation	94
A.1.3 Two Term Gaussian for XRD Analysis	95
A.1.4 Lorentzian Fit	95
A.1.5 Theoretical Thermomechanical Noise Spectral Density	95
A.1.6 Responsivity in LDV Measurements	96
A.1.7 Effective Piezoelectric Coefficients due to Secondary Phenomena	96
A.2 Matlab Codes used in Doctoral Work	98
A.3 AlN Wafer Catalog	102
A.4 Al _{0.6} Sc _{0.4} N Wafer Catalog	103
A.5 Etch Test Tables	104
A.6 Wafer Level Runcard	105
A.7 Wafer Level Mask Design	107
A.8 Supplementary SEM Electrode Images from Flexoelectric Actuator Fabrication	108
A.9 Supplementary Data on DC Measurements	108
A.10 Theta2theta Curves of HfO ₂ on Si Substrates and Pt-Coated Substrates	110
A.11 Designed versus Measured Cantilever Lengths	111
A.12 Designed versus Effective Cantilever Lengths	111
A.13 Expanded Flexoelectric and Effective Piezoelectric Coefficient Results	112
A.14 Supplementary Data from Chapter 4 Flexoelectric Coefficient Analysis	113
A.15 Supplementary Data from Chapter 4 Flexoelectric Coefficient Analysis	114
A.16 Data from Chapter 4 Curvature Generation Analysis	115
Bibliography	117
Contributions to Doctoral Work	135
Photographic Credits	137
Curriculum Vitae	139

List of Figures

1.1	Breakdown of dielectrics and aluminum nitride (AlN) crystal structure	4
1.2	Reactive sputtering and structure zone model for sputtered thin films	7
1.3	C-axis texture versus piezoelectric response in AlN thin films	9
1.4	AlN thin film applications	10
1.5	AlScN thin film applications	17
1.6	Abnormal grain growth in AlScN thin films	20
1.7	Piezoelectric versus flexoelectric-based flexural actuators	21
1.8	State of the art in measured flexoelectric coefficients	27
2.1	Methods to measure XRD theta2theta and rocking curves	32
2.2	Influence of sputtering power and temperature on AlN rocking curve FWHM .	36
2.3	Influence of AlN seed layer thickness on AlN actuation layer rocking curve FWHM and piezoelectric response	38
2.4	Gaussian analysis to deconvolute the (0002) theta2theta diffraction peak	39
2.5	Influence of seed layers, bottom electrode layers and bottom electrode sputter- ing system on AlN c-axis texture	42
2.6	Influence of Ar gas concentration and substrate bias voltage on properties of aluminum scandium nitride (AlScN) thin films	45
2.7	Influence of Ar gas concentration on Al _{0.6} Sc _{0.4} N c-axis texture	47
2.8	Ar gas concentration versus abnormal grain density	48
2.9	Density of abnormal grains versus substrate bias voltage and Ar gas concentration	49
3.1	Flexoelectric actuator process flow	55
3.2	Cantilever electrode and chip level mask designs	56
3.3	Wafer level fabrication results	57
3.4	Issues encountered during wafer level fabrication	60
3.5	Dry fencing source tests	63
3.6	Run 1 fabrication results	64
3.7	Run 2 fabrication results	65
3.8	Run 3 fabrication results	67
3.9	DC measurements of Mo/HfO ₂ film stack	68
3.10	Capacitance-voltage and tangent loss measurements of Mo/HfO ₂ film stack . .	70
3.11	Polarization-electric field measurements of Mo/HfO ₂ film stack	70

List of Figures

3.12 XRD theta2theta curves of HfO ₂ thin films on Mo electrode layers	71
3.13 Experimental setup for measuring cantilever deformation in vacuum	73
3.14 Example of a frequency sweep and TMN measurement	74
3.15 Example of cantilever deformation results versus AC drive and DC bias	75
3.16 Average flexoelectric coefficient from measurements on five chips	78
4.1 Experimental flexoelectric coefficient analysis from literature	86
4.2 State of the art in piezoelectric and flexoelectric curvature generation	89
4.3 Piezoelectric versus flexoelectric curvature generation at the nanoscale	90
A.1 AlN wafer catalog	102
A.2 AlScN wafer catalog	103
A.3 Etch tests results for HfO ₂ , TiO ₂ and Mo thin films	104
A.4 Wafer Level Runcard Part 1	105
A.5 Wafer Level Runcard Part 2	106
A.6 Wafer level mask design	107
A.7 Supplementary SEM images of electrode with fabricated cantilevers	108
A.8 Repeated IV sweeps to confirm IV behavior	109
A.9 Auxiliary HfO ₂ XRD Characterization	110
A.10 Supplementary data from Chapter 4 flexoelectric coefficient analysis	114

List of Tables

1.1	Piezoelectric materials	5
1.2	Measured flexoelectric materials	25
2.1	Tested AlN sputtering parameters	35
2.2	Tested substrate conditions on AlN c-axis texture	41
2.3	Sputtering parameters during $\text{Al}_{0.6}\text{Sc}_{0.4}\text{N}$ deposition experiments	44
2.4	$\text{Al}_{0.6}\text{Sc}_{0.4}\text{N}$ dry etching tests	51
3.1	Chip level fabrication run comparison	62
3.2	Layer thicknesses in symmetric and asymmetric thickness cross sections	65
3.3	Electrical resistance from top to bottom electrode through the HfO_2 layer	69
3.4	Calculated flexoelectric and effective piezoelectric coefficients on five chips	79
4.1	Power law fitting results for experimental flexoelectric coefficients	85
A.1	Resistance of top and bottom Mo electrodes before and after chip level fabrication	108
A.2	Designed and fabricated cantilever lengths	111
A.3	Designed and effective cantilever lengths	111
A.4	Calculated flexoelectric and effective piezoelectric coefficients	112
A.5	Experimental flexoelectric coefficients from literature for Chapter 4 analysis	113
A.6	Comparison of HfO_2 , TiO_2 and AlN curvature generation at the nanoscale	115

1 Introduction

Micro- and nanotechnologies are today integrated into many devices of our day to day life, from the cell phones and computers we use to work and communicate with, to sensors we use to interact with our environment. After Richard P. Feynman's pivotal 1959 talk 'There's Plenty of Room at the Bottom', an enormous development in micro- and nanotechnologies occurred, particularly in microelectromechanical systems (MEMS) and micro/nanoelectronics. However, nanoelectromechanical systems (NEMS), the natural successor to MEMS, have not yet been investigated much beyond the academic environment but offer several advantages to their larger counterparts.

At the intersection between quantum and classical mechanics, NEMS are a source of unique dynamics and physical/chemical interactions. Due to their dimensions, they are also effective sensors with a host of attractive characteristics, such as large quality factors and high resonance frequencies, as well as low effective masses and heat capacities. Despite the many issues surrounding NEMS, such as the difficulty in their fabrication and in integrating NEMS with larger systems, many research groups have invested in developing nanofabrication techniques as well as applying NEMS in the photonics, electronics and biomedical fields [1, 2, 3].

To actuate and sense the motion of NEMS, various physical phenomena are possible, including thermoelastic actuation [4, 5] and piezoresistive detection [6], as well as magnetomotive [7], electrostatic [8], and piezoelectric transduction [9, 10]. While each method has its advantages and disadvantages [2], piezoelectricity, in particular implemented with non-ferroelectric thin films, offers several advantages, including straightforward integration, low power consumption, linear behavior and scalability to the nanoscale [11, 12, 13].

By decreasing the dimensions of sensors to the nanoscale, their sensitivity can increase due to the reduced effective mass and larger surface to volume ratio [1]. The flexural curvature of nanoscale actuators can also increase with decreasing device thickness, due to lower flexural rigidity [14]. However, the integration of piezoelectric thin films into NEMS is still a challenge due to the difficulty in fabricating high quality piezoelectric thin films at the nanoscale.

Flexoelectric actuation is undergoing research as an alternative to piezoelectric actuation at the nanoscale and offers three advantages over piezoelectricity: it is theorized to exist in all dielectrics, its coefficients theoretically do not decrease with decreasing film thickness and, particular for flexural NEMS, an asymmetry of the thickness cross section is not necessary to generate a curvature. Most of the experimental work on the flexoelectric effect has been in ferroelectrics and paraelectrics; recently, a flexoelectric nanoactuator was demonstrated with paraelectric strontium titanate (SrTiO_3) [15, 16]. However, little research has been completed on dielectrics which are complementary metal-oxide-semiconductor (CMOS)-compatible and could be envisioned to replace piezoelectric thin films.

In this thesis, AlN and AlScN piezoelectric thin films, as well as flexoelectric thin films based on amorphous hafnium oxide (HfO_2), are investigated for actuating NEMS. Therefore, this chapter will first go into the theory of piezoelectricity, the state of the art in MEMS and NEMS piezoelectric actuation and a review of the influence of reactive sputtering parameters and substrate conditions in the growth of AlN and AlScN thin films at the micro- and nanoscale. Then, the theory behind the flexoelectric effect is discussed, along with a review of the calculated and experimental flexoelectric coefficients for a number of dielectrics. Finally, the motivations are provided for further research in optimizing the reactive sputtering of AlN and AlScN, as well as investigating the flexoelectric effect in high-k dielectrics such as HfO_2 .

1.1 Piezoelectric Thin Films for NEMS

In this section, the state of the art on reactive sputtering of AlN and AlScN is analyzed and the motivations are outlined for this thesis' work on AlN and AlScN thin films for NEMS. First, a brief review is completed on piezoelectricity and piezoelectric materials. Then, thin film deposition with sputtering is described in detail. Afterwards, a summary is given of the state of the art in AlN and AlScN thin film applications and the reactive sputtering optimization seen in literature to achieve highly c-axis textured thin films. Finally, the motivations for continuing research on reactive sputtering optimization at nanoscale thicknesses is provided.

1.1.1 Piezoelectricity and Piezoelectric Materials

Piezoelectricity, which was discovered by Jacques and Pierre Curie in 1880, is an electromechanical phenomenon occurring in certain crystalline materials with non-centrosymmetry. In these materials, an applied mechanical stress generates electrical charges and an applied electric field generates a mechanical strain. This phenomenon is utilized in applications varying from medical devices, automotive sensing and electronic components. For example, electronic filters based on piezoelectric resonators are present in every modern cellphone [17]. In MEMS and NEMS applications, piezoelectric thin films are an essential part of filters and oscillators [18], ultrasonic transducers [19], and sensors [13].

The generalized constitutive equations for the piezoelectric effect are:

$$P_i = \chi_{ij} E_j + e_{ijk} \sigma_{jk} \quad (1.1)$$

$$\sigma_{ij} = c_{ijkl} \epsilon_{kl} + e_{ijk} E_k \quad (1.2)$$

Where the tensors are defined as: P is the polarization, σ is the mechanical stress, χ is the electric susceptibility, which is related to relative permittivity ϵ_r by $\chi_e = \epsilon_r - 1$, E is the electric field, ϵ is the mechanical strain, and e is the piezoelectric stress coefficient. Equations 1.1 and 1.2 describe the direct and converse piezoelectric effects, respectively [20].

Piezoelectricity can be used for actuation and sensing in MEMS/NEMS by generating a mechanical stress due to an applied electric field or generating a polarization due to an applied mechanical strain, respectively. To generate a curvature in flexural MEMS/NEMS, the thickness cross section should be comprised of a piezoelectric layer sandwiched between electrode layers and the neutral axis should be displaced from the center of the piezoelectric layer. This displacement of the neutral axis is necessary to translate the strain generated by the converse piezoelectric effect into a strain gradient across the thickness cross section, which in turn generates the flexural curvature. The generated bending moment M due to the converse piezoelectric effect in flexural MEMS/NEMS is equal to [2]:

$$M(t) = \frac{d_{31} w Z_P V_{AC}}{C_{11}} \quad (1.3)$$

Where $M(t)$ is the bending moment, d_{31} is the piezoelectric strain coefficient, w is the width of the beam, Z_P is the difference between neutral axis and center of the piezoelectric layer in the thickness cross section, V_{AC} is the applied alternating current (AC) drive and C_{11} is the elastic constant of the piezoelectric thin film. Curvature κ and bending moment M defined as $\kappa = \frac{M(t)}{\langle EI_{z,y0} \rangle}$, the bending curvature generated by a piezoelectric layer in a cantilever is:

$$\kappa = \frac{e_{31} Z_P V_{AC}}{D_f} \quad (1.4)$$

Where D_f is the flexural rigidity, which is the resistance of the cantilever to bending; the equation for the flexural rigidity can be found in Appendix A.1.1.

Piezoelectric materials are a subset of dielectrics, which are comprised of any polarizable material with electrically insulating properties. In general, dielectric polarization occurs through four physical phenomena within the dielectric material: ionic, electronic/atomic, dipolar and space charges [21]. An overview of different dielectric materials is shown in Figure 1.1 A, including piezoelectrics, pyroelectrics and ferroelectrics.

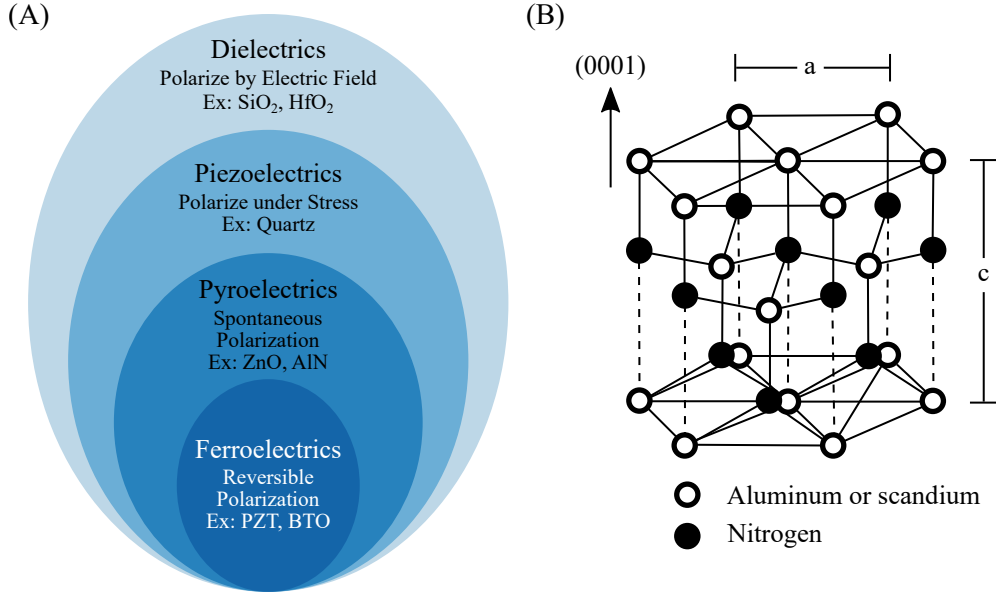


Figure 1.1 – (A) Sub-classes of dielectric materials with prominent characteristics and example materials. (B) Hexagonal crystal structure of AlN or AlScN with a Sc atomic concentration less than 43%, as well as an indication of (0001) c-axis orientation. Hollow and solid circles denote aluminum/scandium and nitrogen atoms, respectively. Adapted with permission from [22].

The piezoelectric effect occurs in non-centrosymmetric materials, meaning that some axes within the crystal lattice cannot be mirrored. Non-piezoelectric piezoelectric materials, like quartz, do not polarize unless under stress. Pyroelectrics, like AlN and zinc oxide (ZnO), have a permanent dipole moment oriented along the polar axis of the unit cell. Other piezoelectric and pyroelectric materials include quartz, gallium nitride and lithium niobate [23]. Below the Curie temperature, ferroelectrics maintain a spontaneous, non-zero electrical polarization whose direction can be modified by a sufficiently high applied electric field [24, 25].

Both single crystal and polycrystalline dielectric materials can be piezoelectric; depending on the crystal structure of the material, its behavior can be dielectric, piezoelectric or ferroelectric. For pyroelectric, polycrystalline materials, the polar axis of the majority of grains must be oriented in the same direction for an average piezoelectric response to be generated. For example, in AlN thin films, the polar axis is the c-axis of the hexagonal crystal structure, labeled as (0001) in Figure 1.1 B. In literature, the c-axis direction of AlN can also be labeled as (0002) or (00*2) with no change in meaning. Growing AlN with the c-axis oriented normal to the substrate surface allows the generation of a piezoelectric response through the thickness of the thin film, which is exploited in both longitudinal and transverse mode resonators [26].

Ferroelectrics are a subset of piezoelectric materials with a spontaneous polarization that can be reoriented under an external electric field. They possess piezoelectric coefficients up to two orders of magnitude larger than for pyroelectric materials such as AlN and ZnO [27],

Table 1.1 – Piezoelectric and dielectric properties of three common piezoelectric materials in MEMS: AlN, ZnO and PZT. $\text{Pb}(\text{Zr}_x\text{Ti}_{1-x}\text{O}_3$ (PZT) composition ranges from $x=0.3$ to $x=0.6$. CSD is chemical solution deposition.

Thin Film	AlN (sputtered) [33, 34, 26]	ZnO (sputtered) [35, 36]	PZT (CSD) [37]	LiNiO ₃ (single crystal) [38, 39]
$d_{33,f}$ (pm/V)	3.9	5.9	60 to 130	
$e_{31,f}$ (C/m ²)	-1.07	-1.0	-8 to -12	0.3
ϵ_r	10.3	10.9	300 to 1300	30-40
$\tan \delta$	0.003	0.01 to 0.1	0.01 to 0.03	10^{-3}

though at the cost of higher dielectric losses in the material. Examples of ferroelectrics and relaxor ferroelectrics include lead zirconate titanate (PZT) [28], barium titanate (BaTiO_3), lead magnesium niobate (PMN) and lead magnesium niobate-lead titanate (PMN-PT) [29]. In particular, PZT has been integrated into ultrasonics [19], micromotors [30], non-volatile memories [31] and energy harvesting devices [32].

Table 1.1 compares the piezoelectric and dielectric properties of AlN, ZnO and PZT, which are three common materials in MEMS. On the one hand, AlN and ZnO have lower piezoelectric coefficients than PZT, but on the other hand, the two pyroelectric materials have a lower relative permittivity and dielectric losses. Of the three materials, AlN is the most promising for NEMS, because PZT contains non-CMOS materials and requires specific substrates for a correct crystal growth [40], while ZnO is not as chemically stable as AlN and has been found to react with integrated circuit materials [10].

AlN thin films in both single crystal and polycrystalline forms can be deposited by pulsed laser deposition (PLD) [41, 42], atomic layer deposition (ALD) [43, 44], molecular beam epitaxy (MBE) [45], metalorganic chemical vapor deposition (MOCVD) [34] and reactive sputtering [26]. Reactive sputtering is typically preferred for depositing polycrystalline AlN thin films due to the low thermal budget, which further increases its CMOS-compatibility [46], and residual stress control. In the next section, the sputtering deposition technique is described, as well as the influence of sputtering parameters on the structure of sputtered thin films.

1.1.2 Sputtering Technique and Sputtered Thin Film Structure

Sputtering is a type of physical vapor deposition (PVD) where a target is physically bombarded to eject the atoms of interest onto a substrate within a vacuum chamber. A large direct current (DC), DC-pulsed or radio frequency (RF) potential generates a plasma, within which fast moving electrons collide and ionize the argon (Ar) atoms. The positively ionized Ar ions are then attracted to the negatively charged target and bombard its surface, physically removing target atoms. Most sputtering systems are equipped with a magnetron configuration to better confine generated electrons to near the target surface, which in turn generates a higher plasma density and higher deposition rates, while better protecting the substrate from resputtering.

DC sputtering is used for deposition of metal thin films, while DC-pulsed and RF sputtering are used for insulating thin films, which is necessary to avoid charge build-up on the target surface. The substrate can be RF-biased to generate some ion bombardment of the substrate and increase adatom mobility [47, 48].

Reactive sputtering is achieved by introducing oxygen (O) or nitrogen (N) gases during the sputtering process, which become ionized and react with the sputtered material before depositing on the substrate surface. A schematic of the reactive sputtering process for depositing AlN is shown in Figure 1.2 A. For doped thin films, either single targets comprised of the alloy of interest or co-sputtering of multiple targets can be used to deposit thin films with a specific composition [49]. A full description of the deposition modes in reactive sputtering is provided by Berg *et al.* [50].

The microstructure of sputtered thin films was originally described through a structure zone model (SZM) by Movchan and Demchishin to be dependent on the ratio of substrate temperature T_S to melting temperature of the metal T_M and comprised of three zones (I, II, III) [51]. Thornton expanded upon this work to include the Ar pressure, or in principal, the working pressure, since these parameters also greatly affect the final microstructure by influencing the adatom mobility. He also introduced a transition zone T [51, 52]. A visual representation of the Thornton's SZM can be seen in Figure 1.2 B. Messier *et al.* later found that the substrate bias influenced the boundary between zone I and zone T, such that with higher substrate bias, the zone T would be possible at lower T_S/T_M ratios [53].

Altogether, the four zones define four grain structures for sputtered thin films:

- Zone I: $0.1 > T_S/T_M$
 - Shadowing effects
 - Small, tapered grains and porous morphology
 - Low adatom mobility, inter-grain shading creates void structure.
 - Increasing Ar pressure enlarges T_S/T_M range where Zone I is possible
- Zone II: $0.1 < T_S/T_M < 0.3$
 - Surface diffusion
 - Dense fibrous grains, smooth surface
 - Higher adatom mobility than Zone I
 - Increasing substrate bias moves down the T_S/T_M range where Zone T is possible
- Zone II: $0.3 < T_S/T_M < 0.5$
 - Surface diffusion
 - Columnar grains, dense structure and high degree of binding at grain boundaries
 - Higher adatom mobility than Zone T, grain boundary migration possible
- Zone III: $0.5 < T_S/T_M$
 - Bulk diffusion
 - Columnar grains and high crystallinity
 - Very high adatom mobility, grain boundary migration and recrystallization possible

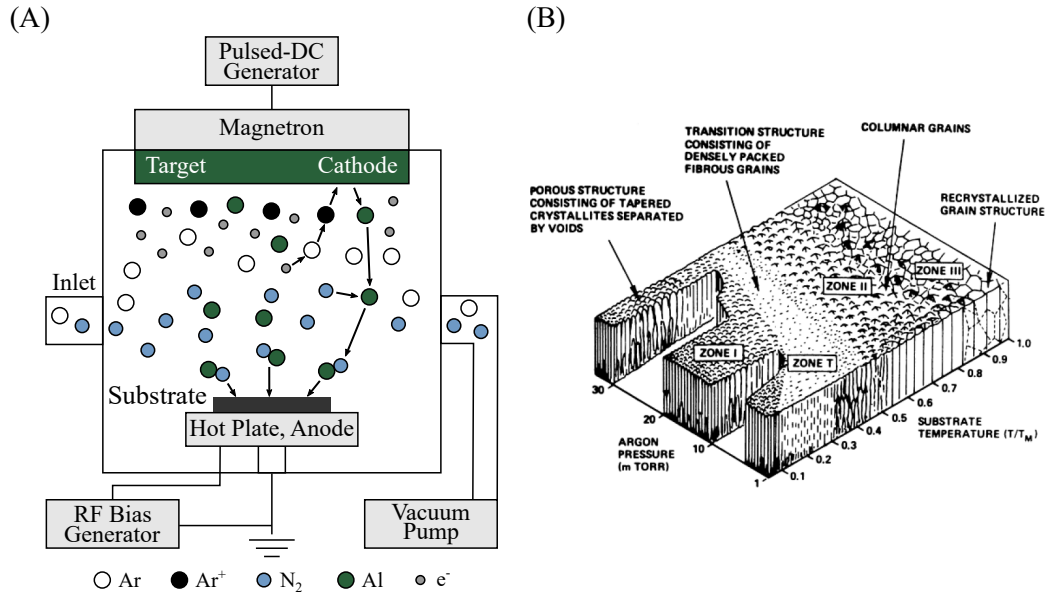


Figure 1.2 – (A) Schematic of DC-pulsed magnetron sputtering system for reactive sputtering of AlN. In the case of AlScN sputtering with a single target, Sc atoms will also be ejected from the target. Cooling of target and substrate holder is not included in schematic as well as grounding of the sputtering chamber. (B) SZM as a function of substrate temperature and Ar pressure. One can see the generation of Zone T at lower substrate temperatures as Ar pressure decreases [52, 48].

For reactive sputtering of insulating materials, the SZM serves as a guide but cannot completely determine the final microstructure, since the sputtering power and reactant gas flow also influence the grain growth. For sputtered ZnO, Mirica *et al.* found a significant shift in the temperature ranges for each zone and claimed that the shift was due to the energetic species generated in the sputtering process. They measured less than 100°C between each zone and subzone, which is much less than what was seen for metal thin films [54]. Zones I and T are usually predominant when deposition temperatures are below 400°C.

1.1.3 Characterization of Piezoelectric Thin Films

The quality of AlN and AlScN thin films can be characterized by a variety of methods, including:

- X-ray diffraction (XRD) [55]
- Atomic force microscopy (AFM)
- Piezoresponse force microscopy (PFM) [56]
- Residual stress through wafer curvature measurements
- Scanning electron microscopy (SEM)
- Transmission electron microscopy (TEM) [57, 58]

XRD is a non-invasive characterization technique that can be used to determine the crystalline properties of single and polycrystalline thin films. Wafer curvature measurements are also non-invasive and help to determine the macro residual stress present within the thin films and help indicate the success of the thin film deposition. The other techniques involve direct contact with the thin films to determine surface roughness or piezoelectric response (AFM/PFM) or bombardment of high energy electrons to image the thin films with up to atomic resolution (SEM/TEM).

XRD rocking curves are a noninvasive method for characterizing AlN and AlScN thin films; they are used to determine the distribution of tilt angles the grains within the thin films have with respect to the substrate surface normal. Grains tilted in respect to the normal of the substrate surface will decrease in the piezoelectric response in both the longitudinal and transverse directions [59, 60]. An inverse relationship has been demonstrated between increasing piezoelectric response and decreasing rocking curve full width at half maximum (FWHM) values in AlN thin films, which can be seen in Figure 1.3 A [61].

However, XRD rocking curve analysis alone is not enough to determine if devices comprised of AlN thin films will necessarily have good piezoelectric characteristics, since it has been shown that it is not necessary to have low rocking curve FWHM values for a high piezoelectric response. For example, the influence of two substrates (platinum (Pt) and silicon (Si)) and two sputtering methods (RF or pulsed DC) on the electromechanical coupling k^2 can be seen in Figure 1.3 B. If non-(0002) AlN diffraction peaks appear in XRD θ - 2θ measurements (hollow symbols in Figure 1.3 B), then even with low rocking curve FWHM values, the electromechanical coupling is heavily reduced [62]. To be able to systematically use rocking curves to characterize AlN and AlScN, two conditions must be met: no other AlN diffraction peaks than (0002) can be present and the relationship between rocking curve FWHM and piezoelectric response must be determined for each sputtering system and substrate.

To extract the piezoelectric coefficients of thin films, laser Doppler vibrometers (LDVs) as well as single or double beam interferometers can be used to measure the displacement of piezoelectric thin films sandwiched between electrodes [63, 64, 65, 66]. Electrical characterization of acoustic structures such as bulk acoustic waves (BAW), surface acoustic waves (SAW) resonators or contour mode resonators (CMRs) [46, 67, 68] or PFM can also be used to determine the piezoelectric coefficients of a material.

1.1.4 AlN Thin Films and Piezoelectric Applications

Although having lower piezoelectric coefficients compared to PZT [75], AlN thin films are thermally stable, can be deposited at low processing temperatures with a high c-axis texture and are CMOS compatible thanks to the absence of contaminating elements [69]. AlN thin films have also been found to be chemically stable when annealing up to 700°C in oxygen or nitrogen environments, which means they can be used in applications for harsh environments [76]. Several reviews have been published on the fabrication, characterization and implementation

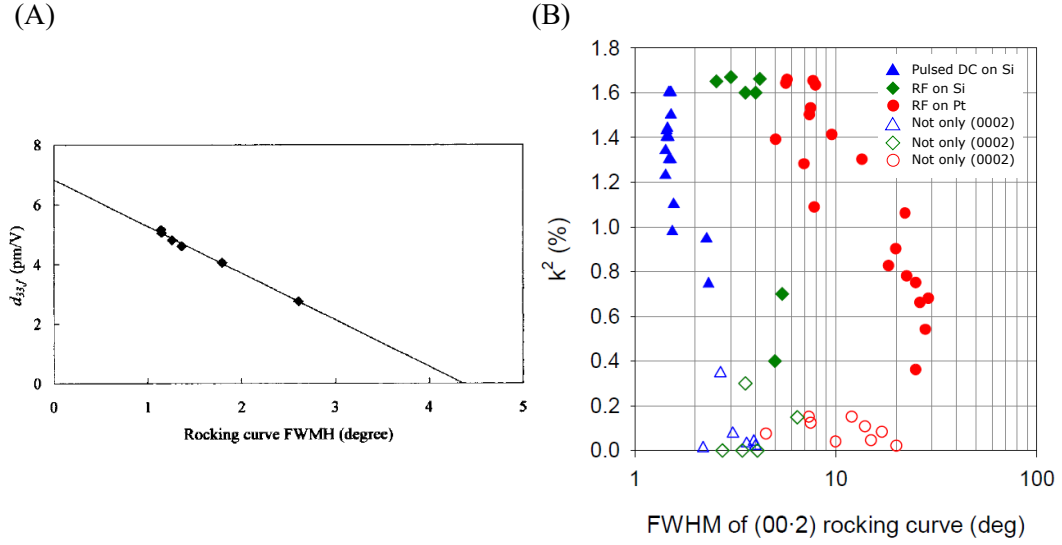


Figure 1.3 – Comparison of c-axis texture versus piezoelectric response. (A) An inverse relationship has been measured between the piezoelectric coefficient $d_{33,f}$ and AlN rocking curve FWHM [61]. Lower FWHM means better alignment of the AlN grains relative to the substrate normal, which will increase the overall piezoelectric response if the polarization axis of the grains are oriented in the same direction. (B) Electromechanical coupling k^2 versus rocking curve FWHM of AlN thin films deposited through DC-pulsed magnetron sputtering on heated Si substrates (circle symbols), through RF sputtering on oxidized Si substrates (diamond symbols) or RF sputtering on Pt-coated Si substrates (triangle symbols). Solid symbols mean only the (0002) diffraction peak was measured, hollow symbols mean other AlN diffraction peaks were also measured. Depending on the sputtering conditions and substrates (solid symbols), different AlN rocking curve FWHM values will generate similar electromechanical coupling. If crystal orientations other than (0002) are present (hollow symbols), then the piezoelectric response is significantly decreased, even if a low rocking curve FWHMs are achieved [62]. © [2005] IEEE.

of piezoelectric AlN thin films in MEMS and NEMS applications [10, 75, 77, 78, 79, 80]. Books are available with chapters that focus on solidly mounted resonators, thin film bulk acoustic resonators (FBARs) and CMRs [81] as well as on AlN thin film processing and fabrication, flexural resonators and lateral mode resonators [23].

AlN thin films have been implemented in several applications, a few of which can be seen in Figure 1.4. For example, AlN-based FBARs¹ have enjoyed commercial success as filters in telecommunications and are now a multi-billion dollar industry [17, 18, 46, 82, 83]. Lateral mode resonators (CMRs² and Lamb wave resonators) have been heavily researched for RF applications in the last decade due to their high acoustic velocity and the ability to tune the frequency of the resonators lithographically, instead of through changes in the thickness with FBAR [68, 73, 74, 84, 85, 86]. To increase the electromechanical coupling in lateral mode

¹TFBARs is also a common acronym for thin film bulk acoustic resonators

²CMRs are also described as Lamb wave resonators

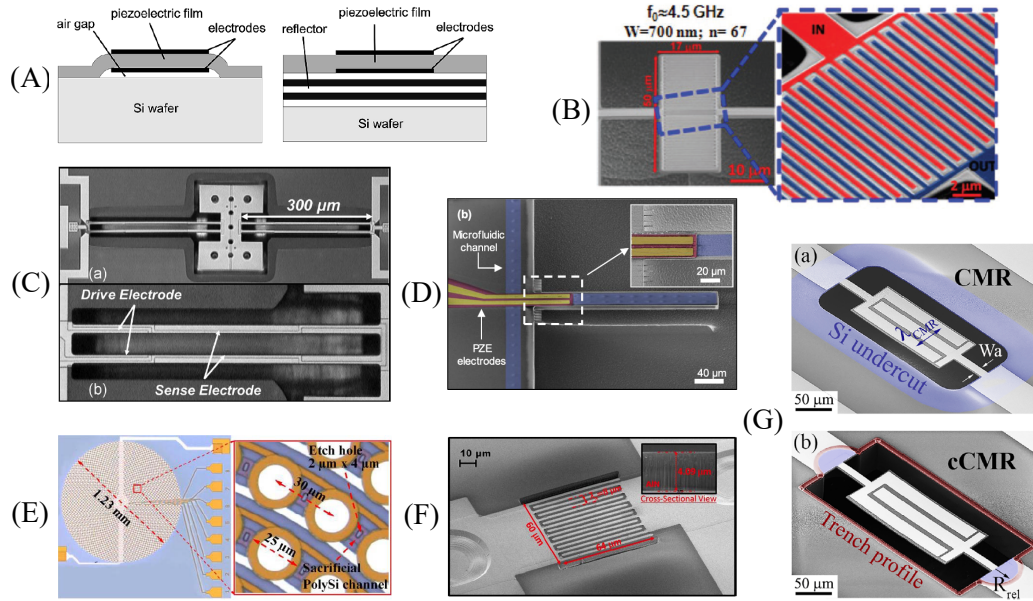


Figure 1.4 – Applications of AlN thin films in literature. (A) Cross section schematic of a FBAR and a solidly mounted resonator. Both types of resonators have been demonstrated for RF applications and feature high quality factors and low frequency drift due to temperature, as well as the ability to be directly integrated into circuits [69]. © [2006] IEEE. (B) GHz CMRs for narrow-band MEMS filters [68]. © [2010] IEEE. (C) Resonant MEMS accelerometers [70]. © [2009] IEEE. (D) SMRs for biological sensing [71]. (E) PMUTs for high resolution medical imaging [72]. © [2015] IEEE. (F) GHz CLMRs for radio-frequency front ends [73]. © [2016] IEEE. (G) 100s MHz CMRs and confined CMRs [74].

resonators, which is lower compared to FBARs, work has been published on cross-sectional Lamé resonators (CLMRs) which couple the thickness and lateral modes [73]. Piezoelectric micromachined ultrasonic transducers (PMUTs) based on AlN have been heavily researched for several applications, including medical imaging, nondestructive testing, range finding and fingerprint sensing [19, 87, 88, 89, 90].

NEMS relays or switches based on AlN cantilevers or buckled doubly clamped beams have also been demonstrated for logic and memory applications due to the low power consumption and little to no leakage current [91, 92, 93, 94]. Flexural resonators based on 50 nm thick AlN films for gravimetric detection were found to have the lowest surface mass limit of detection compared to the state of the art at that time [13]. Others have published work on MEMS accelerometers and microphones integrated with AlN thin films [70, 95]. Finally, suspended microchannel resonators (SMRs)³ actuated and sensed by piezoelectric AlN thin films were demonstrated recently [71].

³The SMR acronym has also been used to previously describe solidly mounted resonators in literature [96].

1.1.5 AlN Reactive Sputtering Optimization

To deposit highly c-axis textured polycrystalline AlN thin films, optimization of both the sputtering parameters and the substrate conditions is necessary. While each sputtering system will require a unique set of specific sputtering parameters to achieve a highly c-axis textured AlN thin film, the trends measured for various sputtering parameters can be generalized. The following paragraphs will break down the state of the art concerning several sputtering parameters and substrate characteristics.

Substrate Three substrate conditions have been shown to improve the c-axis texture of AlN: low surface roughness, similarity of crystal texture to AlN and high overall crystal texture. Crystalline substrates such as Si, quartz and diamond have been shown to generate low AlN rocking curve FWHM values, which mean better c-axis texture and potentially better piezoelectric response. Okano *et al.* demonstrated one of the first examples of highly textured AlN on Si substrates, generating AlN rocking curve FWHMs between 1-2° [97].

In an expanded study of crystalline, nonmetallic substrates, and Si were found to generate the lowest AlN rocking curve FWHM values by way of low surface roughness and similar orientation of the terminating face for epitaxial growth of AlN. Diamond as a substrate was also found to generate low AlN rocking curve FWHM values, despite its increased surface roughness, due to its (111) orientation, which presents a hexagonal-like face for local AlN epitaxial growth [98, 99].

On the other hand, Engelmark *et al.* found that adding a thermal silicon dioxide (SiO₂) layer, which is amorphous, to a Si substrate slightly improved the percentage of AlN c-axis texture versus bare Si substrates [100], although the differences in the results between the two substrates is small. Without measurements of the surface roughness, it is difficult to understand the impact of the thermal SiO₂ layer.

Pt has been demonstrated by several groups as the metal of choice for growing AlN thin films on metal-coated Si substrates, compared to tungsten (W), titanium (Ti) and aluminum (Al) [101, 102]. Pt is a face-centered cubic metal which grows with low surface roughness in a (111) orientation, therefore generating a hexagonal-like terminating face. The lattice mismatch between Pt and AlN is approximately 13%, but the low surface roughness and similar face orientation lead to high quality AlN thin film growth [103]. Löbl *et al.* measured an AlN rocking curve FWHM of 1.4° on Pt-coated substrates compared to 1.6° on SiO₂-coated substrates, but an even lower FWHM of 1-1.4° on bare Si substrates [104].

A study on the influence of Al, Pt, Ti and hafnium (Hf)-coated substrates on AlN deposited between room temperature to 500°C found that Al and Pt-coated substrates generated showed good crystalline stability and high $d_{33,f}$ values, while the Hf and Ti-coated substrates were less chemically stable and generated lower $d_{33,f}$ values [102]. Further investigation of the influence of electrode material and sputtering parameters

ters demonstrated that Pt-coated substrates consistently generated higher $d_{33,f}$ values compared to Ti and Al [33].

Molybdenum (Mo) thin films are easier to fabricate and have more compatible material properties to AlN than Pt, which are important parameters for devices such as FBARs. However, it is a body-centered cubic metal which grows with higher surface roughness compared to Pt and in a (110) orientation, which presents a non-hexagonal terminating face. Therefore, AlN grows with a significantly worse c-axis texture on Mo than Pt. However, in comparison to Al, copper (Cu) and Ti-coated substrates, AlN grown on Mo-coated substrates had the highest percentage of (0002) texture [105].

A few groups have optimized the sputtering of Mo thin films to increase its texture and lower the surface roughness. Decreasing the deposition pressure during sputtering of Mo was demonstrated to lower the surface roughness and increase the c-axis texture of AlN [106]. Increasing the (110) texture of Mo thin films also improved the crystal texture of AlN thin films grown on top [107]. Martin *et al.* optimized both the Mo thin film texture and smoothness such that AlN thin films grown on top achieved a rocking curve FWHM of 1.8° and $d_{33,f}$ of 4 pm/V [103]. A few groups investigated the positive impact of seed layers on the roughness and crystallinity of Mo thin films, which will be discussed in a later section.

In general, the surface roughness of the substrate has been shown to play a strong role in generating highly c-axis textured AlN thin films. In the work of Artieda *et al.*, the surface roughness of amorphous Si deposited on thermally oxidized Si substrates directly correlated with the AlN rocking curve FWHM. They also found that the surface roughness of thermally oxidized silicon substrates correlated in the same trend line, but Pt-coated substrates instead did not, which they suggested to be due to AlN nucleating with local epitaxy on Pt-coated substrates in contrast to amorphous substrates [108]. Despite the local epitaxial growth of AlN on Pt, the surface roughness of Pt thin films was still found to be correlated with the AlN rocking curve FWHM [109].

Seed Layers Seed layers can serve three functions: they can improve the nucleation of thin films that are deposited on top of them (seed), they can improve the adhesion of later deposited metal thin films which otherwise would not strongly adhere to most substrates (adhesion), and they can act as an elastic layer in a piezoelectric actuator by shifting the neutral axis from the center of the piezoelectric layer (elastic). In sputtering, the first and second functions of seed layers are applied.

Through the addition of a seed layer below metal electrodes such as Mo and Pt, the texture of both the metal electrodes and AlN is improved. Lee *et al.* measured a decrease in the Mo rocking curve FWHM from 12.85° to 4.6° by introducing Ti seed layers, which decreased the AlN rocking curve FWHM from 3.6° to 1.7° [110]. Piezoelectric coefficients of up to 4.0 pm/V ($d_{33,f}$) were achieved in AlN thin films deposited on Mo electrodes with a Ti seed layer [103]. Others found that gold (Au)/Ti seed layers, decreased the AlN rocking curve FWHM from 9. to 3.0° [111].

Increasing the thickness of AlN seed layers 200 nm was found to continually decrease the rocking curve FWHM of Mo thin films, but after a 100 nm AlN seed layer thickness, the AlN texture saturated at a rocking curve FWHM of 2.5° [112]. However, contradictory results were measured by another research group; they found that increasing the AlN seed layer thickness beyond 30 nm increased the Mo rocking curve FWHM, which was found to be directly related to the AlN rocking curve FWHM [107].

For 10-25 nm thick AlN piezoelectric layers grown on Pt electrode films, the addition of a 20 nm AlN seed layer slightly improved the AlN rocking curve FWHM and d_{31} coefficient [113, 114]. Recently, our group demonstrated that AlN seed layers produced better c-axis texture than Ti seed layers in 50 nm thick AlN thin films and that the thickness of the seed layer has a significant effect on the AlN rocking curve FWHM but not on the piezoelectric response [115].

Substrate Pre-Treatment A cleaning treatment of the substrate was shown to improve the properties of later deposited AlN thin films by removing organic residues and native oxide on silicon substrates. Both the AlN and Ti (0002) theta2theta peak intensities improved when the Si substrate was presputtered by inductively coupled plasma (ICP) sputtering [116]. Yazar *et al.* found that one minute of Ar plasma etching on Pt substrates before depositing AlN decreased the AlN rocking curve FWHM from 3.3 to 1.7° [117].

Substrate Temperature Higher substrate temperatures during the AlN deposition were found to improve the (0002) texture of AlN thin films. Some groups found a consistent improvement the AlN c-axis texture as the substrate temperature increased up to 400 - 500°C [102, 104, 118]. Iriarte *et al.* measured an improvement in the AlN rocking curve FWHM with increasing temperature, but the substrate temperature had less of an effect on the texture as the sputtering power increased [98, 119].

Some groups found an improvement in the c-axis texture of AlN up until a critical substrate temperature and then a decrease. For example, substrate temperatures with the best c-axis texture were found to be 250°C [120], 350°C [100], 400°C [109], and 430°C [121]. It is not clear why some groups did not measure a consistent improvement in c-axis texture with increasing substrate temperature. As discussed in Section 1.1.2, increasing substrate temperature should increase the density of the columnar grains and increase adatom mobility.

Sputtering Power Most groups found that higher sputtering powers improve the c-axis texture of AlN thin films. A design of experiments analysis found that the RF sputtering power had the strongest effect of the c-axis texture of AlN grown on glass substrates [118]. Another group measured a continual improvement in the AlN rocking curve FWHM as sputtering power increased independent of Ar flow, sputtering pressure, substrate temperature and surface roughness [98, 119]. Some groups measured the highest c-axis texture at intermediate sputtering power values, which can indicate that beyond these values, the adatom mobility is reduced due to the higher deposition rate [100, 109, 122].

Target-Substrate Distance One research group found that at lower sputtering powers (less than 500 W), a smaller target-substrate distance of 30 mm generated a lower AlN rocking curve FWHM, while with higher sputtering powers, a larger target-substrate distance of 70 mm gave lower AlN rocking curve FWHM values [98]. Chiu *et al.* confirmed that at higher sputtering powers (1600 W), increasing the target-substrate distance up of 75 mm decreases the AlN rocking curve FWHM [109].

Decreasing the target-substrate distance will increase the deposition rate and adatom mobility, similar to increasing sputtering power, but beyond a certain deposition rate, the adatom mobility decreases due to the shortened diffusion time. Therefore, the optimal target-substrate distance greatly depends on the other sputtering parameters and the distance range available in the sputtering system.

Substrate Bias Some research groups demonstrated an improvement in the crystalline and/or piezoelectric properties of AlN thin films as the substrate bias increased [33, 116]. Increasing the substrate bias increases the energy of ions bombarding the substrate [53]. Dubois *et al.* measured increasing $d_{33,f}$ values, up to 3.5 pm/V, for increasing substrate bias with Ti, Al and Pt substrates. However, this comes at the cost of higher compressive stresses in the AlN thin films due to the higher ion bombardment [33, 102]. A positive influence of higher substrate bias on AlN rocking curve FWHM was demonstrated by Doll *et al.*, but with few measurements to fully confirm the trend [116].

Artieda *et al.* found that increasing substrate bias lessened the effect of substrate roughness on rocking curve FWHM and produced increasingly compressive AlN thin films. They suggested that smoother substrates and higher bias promoted higher adatom mobility during the AlN deposition and contributed to a more c-axis textured AlN film with better percentage of one polarization orientation over another (Al or N polarity) [123].

Other research groups found an optimal range of bias values. The highest c-axis texture was found at -30 V by Lee *et al.* [124]. Higher k^2 values and (0002) texture were measured between 15-50 V substrate bias by Iborra *et al.* [125], while minimum AlN rocking curve FWHM was found between 10-50 V by Iriarte *et al.* [98]. Recently, Knisely *et al.* demonstrated that the RF substrate bias could be varied during the AlN deposition to greatly reduce the residual stress, without significantly affecting the c-axis texture [126].

Sputtering Pressure Most work has demonstrated that decreasing the sputtering pressure gives a better (0002) texture and higher piezoelectric response, as well as higher compressive film stress [33, 97, 98, 100, 119, 127, 128], due to higher energy ion bombardment [53]. Similar to increasing the substrate bias or the N₂ gas concentration, decreasing the sputtering pressure increases the energy of bombarding ions or neutrals by increasing the mean free path in the plasma [53, 127].

Optimal sputtering pressures were from 1 to 7 mTorr, depending on other deposition parameters. For example, optimal pressure values of 7 mTorr [125], 3.75 mTorr (0.5 Pa) [120] and 6 mTorr (0.8 Pa) [109] generated the highest k^2 , (0002) θ_2/θ_1 texture and rocking curve FWHM, respectively.

Contrary to the work above, Ababneh *et al.* found that lowering the sputtering pressure increased the tensile stress of their AlN thin films, though they still measured an improvement in the percentage of (0002) $\theta_2\theta$ texture with decreasing sputtering pressure [122].

Gas Flow Ratio Several groups found an improvement in c-axis texture and piezoelectric response with N₂ gas concentrations (percentage of total gas flow during sputtering that is due to N₂ gas flow) between 75%-100% [33, 109, 117, 127, 120, 122]. However, the improvements come at the cost of generating higher compressive stresses due to the ions or neutrals gaining more energy in the plasma sheath before bombarding the substrate [53].

Huffman *et al.* stated that most of the ion bombardment is by nitrogen atoms, which would increase with increasing N₂ gas concentration [127]. Navarro *et al.* found that growing (0002) texture AlN depended on both the N₂ gas concentration and sputtering pressure [128].

While they did not measure the rocking curve FWHM or piezoelectric response of their AlN thin films, Ababneh *et al.* determined from $\theta_2\theta$ curves that 100% N₂ concentrations provided the highest (0002) texture [122]. Yazar *et al.* found a similar results in their work and further demonstrated a decrease in the AlN rocking curve FWHM from 4.7 to 3.3° with N₂ gas concentration increasing from 50-100% [117].

Two groups found that N₂ gas concentrations of 85% and 80% provided the best (0002) $\theta_2\theta$ texture and lowest rocking curve FWHM of 4°, respectively [109, 120]. However, the works of Iriarte *et al.* did not find a strong influence of Ar/N₂ gas ratio on the AlN rocking curve FWHM [98, 119].

Multistep Deposition Felmetsger *et al.* found that breaking the AlN deposition into two steps, the first in deep poison mode (high N₂ gas concentration) and higher temperature and the second closer to the poison mode/metallic mode (lower N₂ gas concentration) transition and lower temperature, generated AlN thin films with lower rocking curve FWHM values as well as with lower residual stress. In particular, they could fabricate 200 nm and 25 nm thick AlN films on Mo thin films with rocking curve FWHMs of 1.8° and 3.1°, respectively, which are close to the state of the art on Pt electrodes [61]. The deep poison mode with its high N₂ concentration promotes the nucleation of nitrogen basal-oriented small grains [129].

Promising results were found for a three step deposition process for 10-25 nm thick AlN films on extremely thin Ti/Pt electrodes. Similar to Felmetsger *et al.*, the deposition began in deep poison mode, then the N₂ concentration was decreased in two later deposition steps to mitigate the residual stress within the AlN thin film. They achieved rocking curve FWHMs from 1.44° to 4.72° for AlN layer thicknesses between 1000 and 10 nm [113, 114].

1.1.6 Conclusion on AlN Reactive Sputtering Optimization

Based on the state of the art discussed above, one can obtain highly c-axis textured AlN thin films with:

- Highly texture and low surface roughness substrates
- Pt or Mo (if sputtering is optimized) electrodes
- AlN seed layers between 15-30 nm thick
- High substrate temperatures (above 250°C)
- High sputtering powers
 - RF power source: >300 W
 - DC-pulsed power source: >500 W
- Intermediate or high substrate bias (-20 to -60 V, depending on the sputtering system)
- 80-100% N₂ gas concentration
- Sputtering pressure lower than 7 mTorr (actual value depends on sputtering system)
- Larger target substrate distance
- Multistep deposition where the first deposition step is with high N₂ gas concentration

1.1.7 AlScN Thin Films and Piezoelectric Applications

While the chemical stability and CMOS-compatibility of AlN thin films have led to their implementation in a variety of micro- and nanoscale applications, the piezoelectric coefficients of AlN are significantly lower than ferroelectric materials. To enhance the piezoelectric response in AlN thin films, some groups have tried doping with metals such as tantalum (Ta) [130] and chromium (Cr) [131], demonstrating nearly double the piezoelectric coefficient at a few atomic percent of dopant. More recently, Uehara *et al.* demonstrated a four-fold increase in the d_{33} of magnesium niobate-doped AlN (MgNbAlN) films in comparison to undoped AlN [132]. Doping AlN with scandium (Sc), a rare-earth metal, which has been measured to improve the piezoelectric response five-fold relative to undoped AlN [133]. The origin of the strong piezoelectric enhancement in AlScN alloys was found to be an intrinsic alloying effect where an elastic softening increases the lattice's sensitivity to axial strain [134].

Figure 1.5 gives a visual insight to the demonstrated applications for AlScN thin films. AlScN thin films were first integrated in FBARs for RF applications, with Sc concentration up to 12% [135] and 15% [136]. Both confirmed the earlier measurements of Akiyama *et al.* of larger piezoelectric response and lower elastic stiffness for higher Sc concentration [133]. Hashimoto *et al.* then demonstrated SAW resonators with a k^2 of 3.82% based on AlScN thin films (unreported Sc concentration) deposited on 6H-SiC (silicon carbide) substrates, a three-fold increase in the electromechanical coupling factor compared to AlN [86, 137]. Acoustic

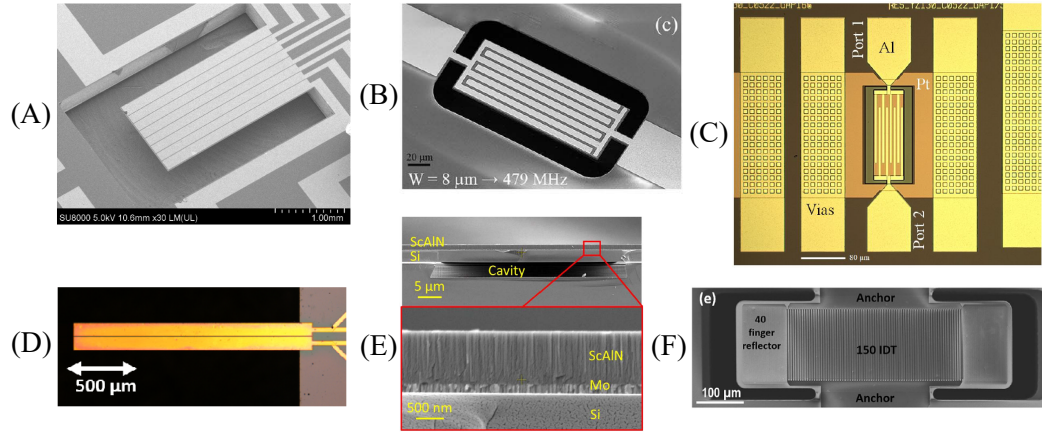


Figure 1.5 – Applications of AlScN thin films in literature. (A) MEMS vibrational energy harvesters [147]. © [2017] IEEE. (B) CMRs with $\text{Al}_{0.82}\text{Sc}_{0.17}\text{N}$ for timing and filtering applications [142]. © [2019] IEEE. (C) laterally vibrating resonators (LVRs) with $\text{Al}_{0.8}\text{Sc}_{0.2}\text{N}$ thin films for RF filters [140]. © [2017] IEEE. (D) Microcantilevers based on $\text{Al}_{0.73}\text{Sc}_{0.27}\text{N}$ for biosensing or liquid sensing [146]. © [2015] IEEE. (E) AlScN PMUTs for medical imaging [144]. © [2017] IEEE. (F) Free standing lamb wave resonators for RF applications [139].

resonators based on contour modes (also known as Lamb wave or lateral modes) [138, 139, 140, 141, 142] or hybrid BAW/SAW modes [143] were also demonstrated with AlScN. AlScN integrated into PMUTs generated a more than two-fold improvement in the electromechanical coupling coefficient [144] and a factor of nine improvement in transmission amplitude compared to AlN-based PMUTs [145]. Cantilevers actuated by AlScN were investigated for applications in sensing and energy harvesting, in both cases demonstrating improved piezoelectric response relative to AlN devices [146, 147].

In order to sputter AlScN thin films with the desired composition, several options are possible. Single targets comprised of an Al-Sc alloy can be used in RF or DC-pulsed sputtering. However, only one composition is possible, and the targets can be extremely expensive, due to the difficulties in fabricating the alloy target [148]. RF or DC-pulsed co-sputtering of Al and Sc targets allow make it possible to deposit a variety of AlScN compositions. In both the single target sputtering and co-sputtering cases, the deposition rate is normally low, since highly c-axis textured AlN and AlScN films grow best in low rate conditions [128, 149]. S-gun magnetron sputtering with two conical ring-shaped targets has been developed with mass production in mind with deposition rates of up to 100 nm/min [148, 150, 151].

While doping AlN with Sc significantly increases its piezoelectric response, the hexagonal crystal becomes more unstable with increasing Sc concentration, which may make deposition of highly c-axis textured thin films more challenging [152, 153]. Therefore, several groups have investigated the effect of Sc concentration, as well as sputtering parameters which would normally affect AlN growth. An outline of their results is completed in the following section.

1.1.8 AlScN Reactive Sputtering Optimization

Sc Concentration Several groups measured an improvement in the piezoelectric response as the Sc concentration in AlScN thin films was increased [133, 136, 152, 154, 155, 156, 157, 158, 159, 160]. The addition of Sc, which would otherwise form ScN with a rock-salt structure, into AlN destabilizes the normal wurtzite (hexagonal) structure and increases the sensitivity to axial strain on the crystal lattice [134]. Maximum piezoelectric coefficients and elastic softening were measured between 41-43% Sc concentration, after which the hexagonal phase is lost, and the nonpolar cubic phase is dominant [133, 154, 156, 157, 158]. Mertin *et al.* and Matloub *et al.* compared their experimental work with ab-initio calculations [134, 161] as well as previously cited experiments and found an excellent agreement [159, 160, 162].

Substrate Compared to AlN, little work has been done on how the substrate, seed layers or substrate pre-treatment affects the crystallinity or piezoelectric coefficients of AlScN thin films. Parsapourkolour *et al.* stated that using an AlN seed layer and insuring there is no surface oxide layer by plasma treatment before the Pt electrode deposition helped generate fully c-axis textured $\text{Al}_{0.85}\text{Sc}_{0.15}\text{N}$ with a $d_{33,f}$ of 6.6 pm/V [163]. Fichtner *et al.* also measured an improvement in the crystallinity of their AlScN thin films grown on Mo electrodes by prior plasma etching and deionized H_2O rinsing to dissolve native or plasma-induced SiO_2 [164].

Substrate Temperature The lowest AlScN rocking curve FWHMs and highest piezoelectric responses were found at substrate temperatures during the AlScN deposition between 200-400°C [133, 154, 155]. Beyond 400°C, the crystalline structure degrades until the hexagonal phase is lost at 800°C [165].

Sputtering Power Yang *et al.* first described the effect of sputtering power on $\text{Al}_{0.94}\text{Sc}_{0.06}\text{N}$ thin films, showing a maximum c-axis texture, piezoelectric response and good electrical properties at an applied DC pulsed power of 130 W [166]. On the other hand, Lozano *et al.* found a much higher DC pulsed power of 700 W gave the smallest rocking curve FWHM of 2.2° and highest $d_{33,f}$ of -12 pC/N for their $\text{Al}_{0.74}\text{Sc}_{0.26}\text{N}$ thin films [149]. Mertin *et al.* similarly measured in $\text{Al}_{0.725}\text{Sc}_{0.275}\text{N}$ thin films that a sputtering power of 1000 W generated a maximum piezoelectric coefficient $e_{31,f}$ of -1.86 C/m² as well as zero to slightly tensile residual stress values [159, 160]. Larger sputtering powers may therefore be necessary for good c-axis texture at higher Sc concentrations.

Substrate Bias On the one hand, one group found little influence of the substrate bias on piezoelectric response through their design of experiments, but on the other hand, Mayrhofer *et al.* demonstrated the highest piezoelectric coefficient d_{33} of 13.2 pm/V at zero bias power [155, 167]. Any conclusions on this sputtering parameter are difficult based off the little work in the state of the art.

Gas Flow Ratio Some groups found that 1:2-1:1 Ar:N₂ gas flow ratios gave higher c-axis texture and piezoelectric coefficients [152, 155, 167, 168, 169]. However, some contradictory results were found in the literature. On the one hand, Lu *et al.* measured better AlScN rocking curve FWHMs and lower density of abnormal grains with 60-100% N₂ gas concentration [170]. On the other hand, Mayrhofer *et al.* found that with increasing the Sc concentration from 0-15%, the lowest FWHM of the (0002) theta2theta diffraction peak was with N₂ gas concentrations from 100% to 65%, respectively [168]. The optimal gas flow ratio was also dependent on the substrate bias [167].

Sputtering Pressure In comparison to Akiyama *et al.*, who found that there was little influence of sputtering pressure on piezoelectric response [155], other research groups found that increasing pressure to the point of having zero stress or slightly tensile stress minimized the abnormal grain density and enhanced the piezoelectric response [152, 159, 160]. Zhang *et al.* and Lozano *et al.* found a similar intermediate pressure value of 3.75-4 mTorr gave the lowest rocking curve FWHMs (below 3°) and highest piezoelectric response (above 8 pC/N for d₃₃) [149, 169].

Target-Substrate Distance Two groups studied the influence of target-substrate distance and found seemingly contradictory results. Fichtner *et al.* found that increasing the target-substrate distance, while maintaining a 75% N₂ gas concentration, decreased the density of abnormal grains [164]. On the other hand, another research group found that increasing the target-substrate distance with 50% N₂ gas concentration increased the density of abnormal grains. However, with a 100% N₂ gas concentration, no influence of target-substrate distance on density of abnormal grains was found [170]. While it has been shown that the AlScN rocking curve FWHM is inversely related to the piezoelectric response [149], like in AlN thin films, the appearance of abnormal grains is similar to the appearance of non-(0002) peaks in theta2theta curves of AlN, which lead to a lower piezoelectric response [62].

Abnormal Grain Growth The growth of abnormal grains in AlScN thin films, an example of which can be seen in Figure 1.6 A, has been correlated with lower piezoelectric response (Figure 1.6 B) [159, 170]. Mertin *et al.* also correlated the density of abnormal grains with higher tensile residual stress, which was due to higher Ar sputtering pressures and lower sputtering power in their work [159]. Another research group found that increasing the N₂ gas concentration from 50% to 100% significantly decreased the density of abnormal grains [170]. Mayrhofer *et al.* used infrared (IR) spectroscopy to more accurately measure the crystallinity of their AlScN thin films, demonstrating that the IR peaks develop shoulders if there is not a high c-axis texture [171].

One group hypothesized that the abnormal grains originated near the substrate interface and measured the grains to have a (0001) texture but grow at a large angle relative to the substrate normal. The same group had earlier measured an increase in density of abnormal grains with increasing Sc concentration [152, 164].

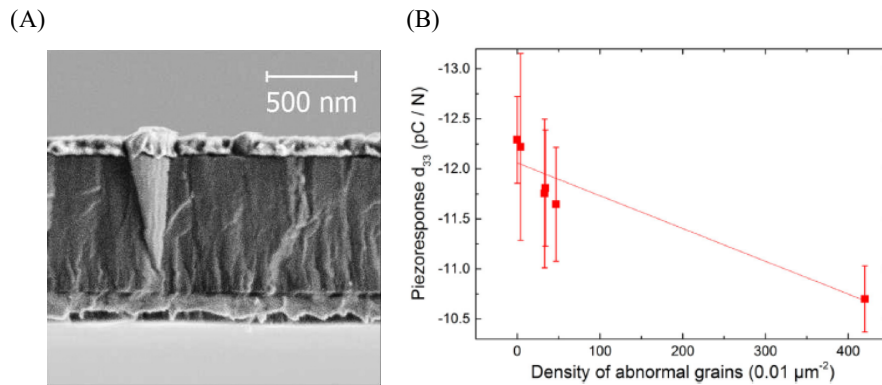


Figure 1.6 – Influence of abnormal grains on AlScN piezoelectric response (A) SEM cross section image of an abnormal grain which formed during non-optimal sputtering of AlScN [164]. (B) An inverse relationship was found between the density of abnormal grains and piezoelectric coefficient d_{33} [170].

Sandu *et al.* were able to demonstrate that the abnormal grains were generated on high-energy, less compact grain boundaries with a high concentration of Sc. Initially, the abnormal grains grow with a Sc-rich rocksalt structure but quickly switching to a wurzite crystal structure growing at a significant angle relative to the substrate normal [153]. Abnormal grains have also been found in AlN thin films where the surface roughness of the substrate was large enough to reduce adatom mobility and cause stacking faults [109].

1.1.9 Conclusion on AlScN Reactive Sputtering Optimization

Based on the state of the art on AlScN sputtering optimization, a few conclusions can be made about how to deposit highly c-axis textured AlScN:

- AlN seed layers and non-oxidized substrates help crystallization
- Substrate temperatures between 200-400°C
- Higher sputtering powers
- Little to no substrate bias
- Pressure values such that slightly tensile films are fabricated
- Higher N_2 gas concentration and sputtering power for lower density of abnormal grains

Abnormal grains in the AlScN thin films have been found to be an issue in the sputtering deposition of AlScN thin films and, like the appearance of non-(0002) peaks in θ - 2θ curves of AlN, have been shown to decrease the AlScN piezoelectric response. The sputtering optimization of AlScN thin films should therefore always include a study on the density of abnormal grains, particularly if XRD is used to evaluate the c-axis texture.

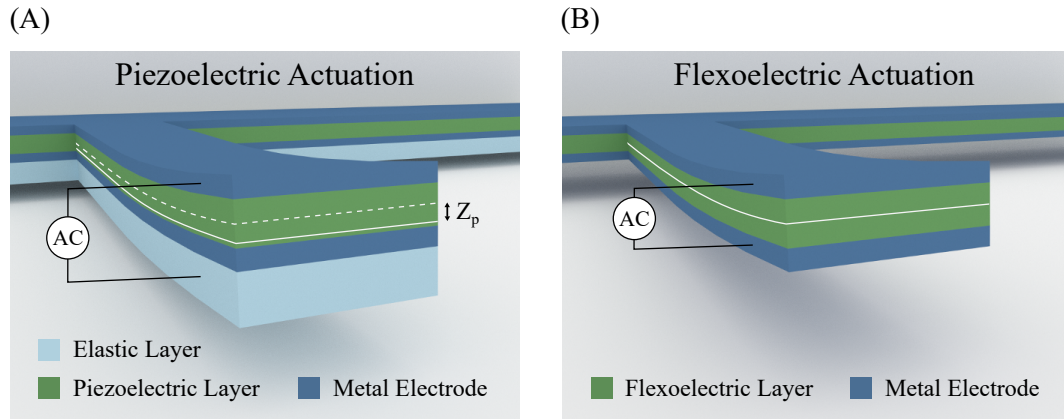


Figure 1.7 – Cross section schematics of (A) piezoelectric and (B) flexoelectric-based flexural actuators. In both cases, the bottom and top electrodes cover the whole cantilever surface. Z_p represents the neutral axis offset from the center of the piezoelectric layer. In piezoelectric beams, this offset is necessary for curvature generation, while in the case of flexoelectric beams, it makes no difference.

1.1.10 Sub-100 nm AlN and AlScN Thin Films for Nanoscale Transduction

Fabrication and integration of highly textured, micron thick AlN films into MEMS has become a robust process. Recently, AlScN thin films with various Sc concentrations have been investigated and demonstrated in a few applications.

For applications where high speed and low power consumption is needed, such as relays or switches for CMOS or zeptogram mass sensing, decreasing the thickness of the system provides a significant improvement. A few systems with integrated AlN layers at or below 100 nm thicknesses have been recently demonstrated [13, 113, 172].

On the one hand, decreasing the thickness of the piezoelectric layer in flexural cantilevers has been shown to increase their potential displacement [14], which increases the interest in nano-actuation and sensing by piezoelectricity. The necessary power to generate deformation also decreases. On the other hand, decreasing the thickness of the actuation layer leads to a decrease in the piezoelectric response, since the c-axis texture and piezoelectric response of AlN has been shown to worsen with decreasing layer thickness [61, 98, 116, 129, 173].

At the moment, the influence of only a few sputtering parameters, such as multistep deposition, substrate pretreatment and seed layers on AlN thin films with thicknesses below 100 nm have been completed [114, 115, 129]. No studies have been completed on AlScN less than 1 μm thick and only two applications have been shown for 500 nm thick layers [146, 147]. Therefore, fabrication of AlN and AlScN thin films at the nanoscale requires more investment in terms of optimizing the sputtering parameters and the substrates conditions.

Two interesting sputtering parameters that can be further studied for AlScN thin films are

substrate bias and gas flow ratio. The substrate bias was found to be an important sputtering parameter for AlN depositions but has been little researched for AlScN thin films. Different groups have found opposing influence of the Ar gas concentration on the crystalline and piezoelectric properties of AlScN thin films; further investigation should be made to provide insight into the influence of the gas flow ratio.

Ultimately, piezoelectric actuators are handicapped by the necessity of maintaining a displacement of the neutral axis relative to the center of the piezoelectric layer to generate a curvature (Z_P in Equation 1.4). For example, generating a non-zero Z_P in the thickness cross section of a piezoelectric actuator is demonstrated by using an elastic layer underneath the bottom electrode in Figure 1.7 A.

In comparison, actuators based on the flexoelectric effect have no limitations on the type of thickness cross sections (Figure 1.7 B) and the flexoelectric coefficients are predicted to remain unchanged in dielectric films with decreasing film thickness. In the next section, flexoelectric actuation is discussed as an alternative to piezoelectric actuation at the nanoscale.

1.2 Flexoelectric Thin Films for NEMS

1.2.1 Theory of the Flexoelectric Effect

The flexoelectric effect in solids describes the electromechanical relationship between polarization and mechanical strain gradients. The generalized constitutive equations including the piezoelectric and flexoelectric effect are defined as:

$$P_i = \chi_{ij} E_j + e_{ijk} \sigma_{jk} + \mu_{klj} \frac{\partial \varepsilon_{kl}}{\partial x_j} \quad (1.5)$$

$$\sigma_{ij} = c_{ijkl} \varepsilon_{kl} + d_{ijk} E_k + \mu_{ijkl} \frac{\partial E_k}{\partial x_l} \quad (1.6)$$

Where the left side and first two terms on the right side of the two equations are the same as in Equations 1.1 and 1.2 and the last term describes the direct and converse flexoelectric effects, respectively. The flexoelectric coefficient μ_{ijkl} is a four-rank tensor that defines the relationship between polarization and strain gradient and vice versa [174].

While the constitutive equations for flexoelectricity give the impression that the effect is asymmetric, since that a strain gradient will generate a homogeneous polarization but not vice versa, Yurkov and Tagantsev were able to demonstrate in a careful analysis of a finite sample that with appropriate boundary conditions, the flexoelectric effect would be symmetric [175].

Potential applications for flexoelectric-based devices include energy harvesting [176, 177], *in-situ* crack monitoring [178], enhanced piezoelectric microcantilevers [179], flexoelectric microcantilevers [180], strain diodes [181] and nanoactuators [16].

First theorized in the late 1950's and early 1960's by Mashkevich and Tolpygo, Kogan provided the phenomenological framework describing the flexoelectric effect [182, 183, 184]. The first use of the term 'flexoelectric effect' in studies of solid dielectrics was by Indenbom *et al.*, taken from earlier work on liquid crystals [185]. Flexoelectricity also exists in polymers and biosystems [186, 187].

Tagantsev expanded the theoretical knowledge of flexoelectricity by nuancing the effect into static, dynamic, bulk and surface contributions [188, 189]. There has been some dispute over whether the surface contributions exist in centrosymmetric insulating materials [190], but recent theoretical and experimental work has provided more evidence that these contributions exist [191, 192, 193].

In this work, only the bulk static flexoelectric and surface piezoelectric effects will be discussed in detail. The dynamic flexoelectric effect is mostly predominant when working with acoustic waves or the smallest feature of the device is on order of the external perturbation. As the smallest feature of the resonators in this work is approximately 100 nm and the working frequencies around 1 MHz, the dynamic flexoelectric effect should be negligible. Surface flexoelectricity is expected to be comparable to the bulk flexoelectric effect in low-permittivity materials, but is difficult to experimentally separate the bulk and surface flexoelectric effects [194].

Kogan was the first to estimate the flexoelectric coefficient as proportional to the ratio of electron charge to crystal lattice parameter [184]. This proportionality was expanded into an order of magnitude estimate of the bulk static flexoelectric coefficient $\mu_{b,s}$ [174, 188]:

$$\mu_{b,s} = \chi_e f_{b,s} \propto \frac{\epsilon_{r,bulk} e}{4\pi a} \quad (1.7)$$

Where $f_{b,s}$ is the bulk flexocoupling coefficient, e is the electron charge and a is the crystal lattice parameter. The bulk flexocoupling coefficient is estimated to be between 1-10 V for a simple atomic lattice, but Yudin and Tagantsev noted that the accuracy in this calculation was one to two orders of magnitude, which makes estimation of the flexoelectric coefficient from Equation 1.7 fairly inaccurate [174].

Surface piezoelectricity should occur in any non-piezoelectric material due to the symmetry-breaking of the crystal lattice in the surface adjacent layers. While the thickness of the layers creating this effect is much smaller than the thickness of the bulk dielectric, it was derived that it can contribute as much as the bulk static flexoelectricity to the total flexoelectric response in low permittivity materials [174, 175].

Similar to the bulk static flexoelectric coefficient, the flexoelectric coefficient due to surface piezoelectricity is proportional to the bulk relative permittivity:

$$\mu_{SP} \propto e\lambda \frac{\epsilon_{r,bulk}}{\epsilon_{r,surface}} \quad (1.8)$$

Where λ is the thickness of the surface layer (~ 0.4 nm if atomically thin) and $\epsilon_{r,bulk}$ and $\epsilon_{r,surface}$ are the relative dielectric permittivities of the bulk and surface layers, respectively. Separating the surface piezoelectric and bulk flexoelectric contributions experimentally is very difficult since both contributions are directly related to the bulk relative permittivity.

The two main contributions to the bulk flexoelectric effect in dielectrics are from ionic and electronic polarizations. Based on the work of Tagantsev [189], Maranganti and Sharma calculated the ionic contribution to flexoelectricity by both ab-initio and shell-model lattice dynamics of several materials, including semiconductors, alkali halides and perovskite dielectrics in the paraelectric phase [195]. Their calculations are of the same order of magnitude as theoretical results found by Askar *et al.* for sodium and potassium chloride [196].

While calculations of the flexoelectric coefficients for SrTiO_3 compare well to calculated and experimental results [197, 198, 199], the BaTiO_3 experimental values are significantly larger than the calculated results. Further discussion on the disparity between experimental and theoretical flexoelectric coefficients is continued in the next section.

For the electronic contribution to flexoelectricity, Hong and Vanderbilt made ab-initio calculations of several materials, including carbon, Si, sodium chloride and some perovskites [200], based off the work of Resta [190].

Several reviews and a book have been published on flexoelectricity in solids, focusing on theory [174] or on materials, experiments and applications [187, 186, 201] or a broad overview on the topic [202, 203, 204]. In the next section, the experimental work on flexoelectricity will be discussed. The theory behind the flexoelectric effect will be further developed in Chapter 2.

1.2.2 Experimental Characterization of the Flexoelectric Effect

The flexoelectric effect in ferroelectrics was originally measured in the 1960s. Ferroelectric BaTiO_3 cantilevers were used to measure the flexoelectric curvature generation from an applied electric potential, the thickness dependence of the curvature generation and the maximization of the flexoelectric effect near the Curie temperature [205, 206]. Interest in experiments on the flexoelectric effect picked up again when Ma and Cross measured the flexoelectric coefficient in BaTiO_3 [207], PMN [208], barium strontium titanate (BST) [209] and PZT [210].

1.2. Flexoelectric Thin Films for NEMS

Table 1.2 – Non-exhaustive list of measured flexoelectric coefficients μ_{12} or μ_{13} , relative permittivity ϵ_r and flexocoupling coefficient f for various ferroelectric, paraelectric and dielectric materials. BST/ZNO is $\text{Ba}_{0.6}\text{Sr}_{0.4}\text{TiO}_3/\text{Ni}_{0.8}\text{Zn}_{0.2}\text{Fe}_2\text{O}_4$. BTO is $\text{Ba}(\text{Ti}_{0.87}\text{Sn}_{0.13})\text{O}_3$. SPT is $\text{Pb}_{0.3}\text{Sr}_{0.7}\text{TiO}_3$. Stars next to the flexoelectric coefficients mean that the data was digitally extracted from graphs within the literature. The methods of measurement are: 3PB (three point bending), CB (acoustic or applied force cantilever bending), 4PB (four point bending), Curv (converse curvature generation).

Material	Crystallinity	μ_{12} or μ_{13} (nC/m)	ϵ_r	f (V)	Method	Reference
PMN-34PT	Single crystal	36,000*	33,000	120	3PB	[212]
PMN-28PT	Single crystal	37,000*	35,000	120	3PB	[212]
PMN	Ceramic	4,000-4,400	13,000	40	CB	[213, 208]
BST/NZO	Ceramic composite	128,000	41400*	350	CB	[214]
BST	Ceramic	96,000*	16,400	650	CB	[209]
BST	Ceramic	8,500	4,100	250	CB	[179]
BTO	Ceramic	53,000	15,000	400	CB	[215]
BaTiO ₃	Ceramic	43,200*	10,200	500	CB	[207]
BaTiO ₃	Single crystal	25,000-100,000*	1,500	1,000-8,000	CB	[179]
BaTiO ₃	Single crystal	200	1,500	22	3PB	[192]
SPT	Ceramic	20,000	14,000	160	CB	[15]
PZT-5H	Ceramic	500	2,200	26	4PB	[216]
PZT-5H	Ceramic	2,000	2,200	100	4PB	[216]
PZT-5H	Ceramic	9,500	11,000	100	CB	[210]
TiO ₂	Single crystal	1.5*	110	1	3PB	[193]
SrTiO ₃	Single crystal	7,5.8	300	3,2	3PB	[198, 199]
SrTiO ₃	Single crystal	4.1	75	6	Curv	[16]

In Table 1.2, a non-exhaustive list of measured flexoelectric coefficients for several materials can be seen. A large enhancement of the flexoelectric coefficients was found in the tested ferroelectrics and relaxors near the temperature of maximum relative permittivity or the Curie temperature. Among the tested materials, those with very high dielectric permittivities generated the highest flexoelectric coefficient values and the largest deviation from the theorized 1-10 V flexocoupling coefficient expected from the theoretical flexoelectric coefficient/dielectric permittivity linear relationship [207, 209, 211]. Flexocoupling coefficients, which can be found in Table 1.2 for several materials, from 100 up to 8000 have been found in very high permittivity materials.

A few sources for the abnormally large flexoelectric coefficients have been suggested and researched. An important note is that relaxors, like PMN, present different polarization properties than ferroelectrics, like perovskites (PZT and BaTiO₃) or relaxor ferroelectrics like PMN-PT (a solid solution comprising ferroelectric and relaxor phases). Therefore, the sources of the high flexoelectric coefficients can be different in each type of material. For example, it has been discussed that some ferroelectric macro-domains and polar nanoregions can persist in ferroelectrics and relaxor ferroelectrics, respectively, beyond the Curie temperature, thus contributing an extrinsic contribution to the measured flexoelectric coefficient [15, 212].

Large applied strain gradients in ferroelectrics and relaxor ferroelectrics can also lead to ferroelastic domain wall motion in unpoled ferroelectrics below the Curie temperature [216, 217]. Recent work in BaTiO₃ and BST ferroelectrics suggest that strain gradients developed in the high-temperature processing of perovskites could break the macroscopic symmetry in those materials and influence the alignment of polar regions or charged defects [218, 219]. Strain gradients were also found to influence the relative permittivity, effective polarization and critical temperature in BaTiO₃ thin films clamped to a substrate [220, 221].

In a study of single crystal BaTiO₃ measured at temperatures beyond the Curie temperature, where any flexoelectric coefficient enhancement from ferroelectric domains should be eliminated, macro polar regions and surface piezoelectricity were suggested to be the major sources of the enhanced BaTiO₃ flexoelectric coefficient. Further measurements at temperatures beyond the hysteresis temperature found a large anisotropy between the flexoelectric coefficients for three different crystal orientations, which was considered an indirect measurement of surface piezoelectricity [192].

In a later work, Narvaez *et al.* attributed the large flexoelectric response in semiconducting BaTiO₃ to surface piezoelectricity based on their barrier layer model, where the bulk of the semiconducting material is conducting and only the interface layers are insulating. They also measured the effective flexoelectric coefficient in titanium dioxide (TiO₂) and niobium-doped TiO₂, showing a 1000-fold enhancement in the coefficient with doping [193].

Flexoelectricity has been shown to have an effect on other research topics in ferroelectrics, such as domain wall stability [222], rotation of polarization at domain walls [223, 224], crystallization [225], critical thickness (dead layer) [226, 227] and spontaneous polarization at interfaces in nonferroelectric perovskites [228]. It also plays a role in size-dependent phenomena such as giant piezoelectric response [90, 229, 230, 231] and nanoindentation [232, 233, 234]. Flexoelectric coefficients have been measured or estimated using a variety of different methods, including:

- Direct Flexoelectric Effect
 - Cantilever bending due to low frequency acoustic drive or applied force [179, 207, 208, 209, 210, 214, 215, 235, 236, 237, 238]
 - Four-point bending [216]
 - Three-point bending [192, 193, 198, 212, 239]
 - Observation of zero polarization state in released membrane [231]
- Converse Flexoelectric Effect
 - Electrical actuation of truncated pyramids [211, 240, 241]
 - Curvature generation in flexural beams due to applied electric field [16, 181, 205]
 - Curvature induced by TEM [242]

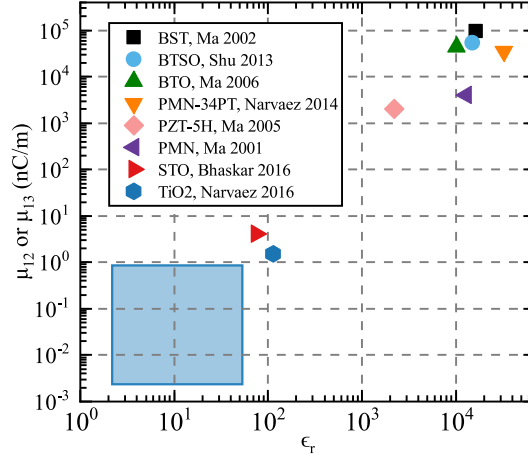


Figure 1.8 – Summary of state of the art in measured flexoelectric coefficients for several materials versus their relative permittivity. References are: BST [209], BTSO [215], BaTiO₃ [207], PMN-34PT [212], PZT-5H [210], PMN [213], SrTiO₃ [16], TiO₂ [193]. Note the absence of measurements in the low relative permittivity range, highlighted by the blue box.

A recent breakthrough in using the flexoelectric effect for nano-actuation and sensing came from the fabrication and characterization of cantilevers actuated by a flexoelectric SrTiO₃ layer [16]. The curvature generated in a flexoelectric-based flexural cantilever is defined as [202]:

$$\kappa = \frac{\mu_{eff} V_{AC}}{D_f} \quad (1.9)$$

Where μ_{eff} includes the bulk flexoelectric and surface piezoelectric contributions, V_{AC} is the AC drive and D_f is the flexural rigidity.

The flexoelectric coefficients of SrTiO₃ have been extensively studied, showing a good correlation between experimental values and ab-initio calculations, making SrTiO₃ an ideal material to test first for nanoactuation [195, 198, 197, 199, 200]. A good correlation was found between the inverse and direct measurements of the flexoelectric coefficient [198, 199].

1.2.3 Flexoelectric Transduction as an Alternative to Piezoelectric Transduction

In comparison to piezoelectric actuation, flexoelectric actuation offers three advantages: the flexoelectric effect is theorized to exist in all dielectrics, flexoelectric coefficients have been predicted not to decrease with decreasing film thickness [174] and no displacement of the neutral axis in flexural NEMS is necessary to generate a curvature. While flexoelectric coefficients of most dielectrics tend to be lower than piezoelectric coefficients, at the nanoscale,

the advantages discussed above can play an important role in choosing between flexoelectric-based curvature generation and piezoelectric-based curvature generation.

SrTiO₃ flexoelectric curvature generation was demonstrated to be comparable to values from state of the art piezoelectric films with similar thicknesses [16]. Other groups have similarly found that when decreasing the actuation layer thickness, flexoelectric thin films can generate larger amount of electrical charge than piezoelectric thin films [180] as well as larger effective piezoelectric coefficients at micron to sub-micron scales [179].

Given the results for flexoelectric actuation based on a paraelectric material, it is worthwhile to investigate other non-ferroelectric materials. By expanding the list of potential active materials from ferroelectrics and piezoelectrics to simple dielectrics, the fabrication and application of NEMS would be greatly simplified. Applications for flexoelectric NEMS could include nanoelectromechanical relays, resonators for super high frequency filters and high-sensitivity mass sensors. Integrating flexoelectric NEMS with non-ferroelectric materials in particular for CMOS applications would be more straightforward, since many high-k dielectric materials like HfO₂ are CMOS compatible. Very few groups have fabricated and characterized nanoscale actuators with piezoelectric or flexoelectric actuation [13, 16, 114]. Further demonstrating the ability to fabricate piezoelectric and flexoelectric NEMS will increase their potential to be integrated into applications in sensing or electronics.

The flexoelectric coefficients of a variety of ferroelectric and paraelectric materials have been measured, but there is on-going research to explain the differences between experimental results and theoretical calculations. To be able to better understand how the experimental flexoelectric coefficient and relative permittivity of dielectrics are related, materials with lower relative permittivities should be measured to fill in the gap highlighted by the blue rectangle in Figure 1.8. Also, little work has been completed to experimentally distinguish between the electronic and ionic contributions to the bulk flexoelectric effect. Measurements of dielectrics with very low relative permittivities and/or amorphous properties would help in the understanding of both of the above topics.

1.3 Outline of Thesis

In this thesis, an investigation of piezoelectric and flexoelectric thin films for NEMS was performed, including the sputtering optimization of sub-100 nm thick AlN and 1 μ m Al_{0.6}Sc_{0.4}N films as well as the fabrication and characterization of flexoelectric sub-100 nm thick resonators based on amorphous HfO₂. The thesis is divided into three chapters:

Chapter 2 discusses the work behind the sputtering optimization of AlN films based on manipulation of several sputtering parameters and substrate properties. The influence of two sputtering parameters on the c-axis texture and density of abnormal grains in Al_{0.6}Sc_{0.4}N films will also be reviewed.

Chapter 3 details the fabrication and characterization of HfO_2 -based flexoelectric actuators, including the process flow and mask design, microfabrication and issues during processing, electrical and optical measurements and analysis of the effective flexoelectric coefficient.

The last chapter will summarize the results in Chapters 2 and 3 and compare the AlN and HfO_2 thin films fabricated in this work to the state of the art. It will also provide some analysis of the relationship between experimental flexoelectric coefficients and relative permittivity and a discussion on piezoelectric versus flexoelectric curvature generation at the nanoscale.

2 Sputtering Optimization of AlN and $\text{Al}_{0.6}\text{Sc}_{0.4}\text{N}$ Thin Films

In this chapter, the crystalline and piezoelectric properties of polycrystalline AlN and AlScN thin films deposited by reactive sputtering are optimized for implementation into NEMS. First, the main characterization techniques are described, including XRD, residual stress and SEM imaging. Then, the influence of several sputtering parameters and substrate conditions on 50 and 100 nm thick AlN films is analyzed. The impact of Ar gas concentration and RF substrate bias voltage is then measured on 1 μm thick $\text{Al}_{0.6}\text{Sc}_{0.4}\text{N}$ films. Finally, a summary is provided of the main outcomes in AlN and AlScN sputtering deposition experiments.

2.1 Material Characterization Techniques

2.1.1 X-Ray Diffraction

One way to measure the crystalline properties of thin films is through XRD, a noninvasive characterization technique. In this technique, X-rays, which have wavelengths the same order of magnitude as the inter-atomic spacing, will be diffracted in the crystalline lattice when the Bragg condition is met [55]. A normal incidence XRD system was used (Bruker D8 Discover) to complete the scans on AlN/AlScN thin films.

Two types of scans were performed to characterize the deposited thin films: theta2theta curves and rocking curves. Theta2theta curves provide a wealth of details about the thin films under study: what crystalline materials are present, their composition and texture, etc. To generate theta2theta curves, both the X-ray source and detector are set at the same angle θ above the substrate. During the scan, θ is increased equally on both sides, moving both the source and detector steadily closer together until the desired final angle. A schematic visualizing the scanning process and an example scan from AlN and Pt thin films deposited on a Si substrate can be seen in Figure 2.1 A.

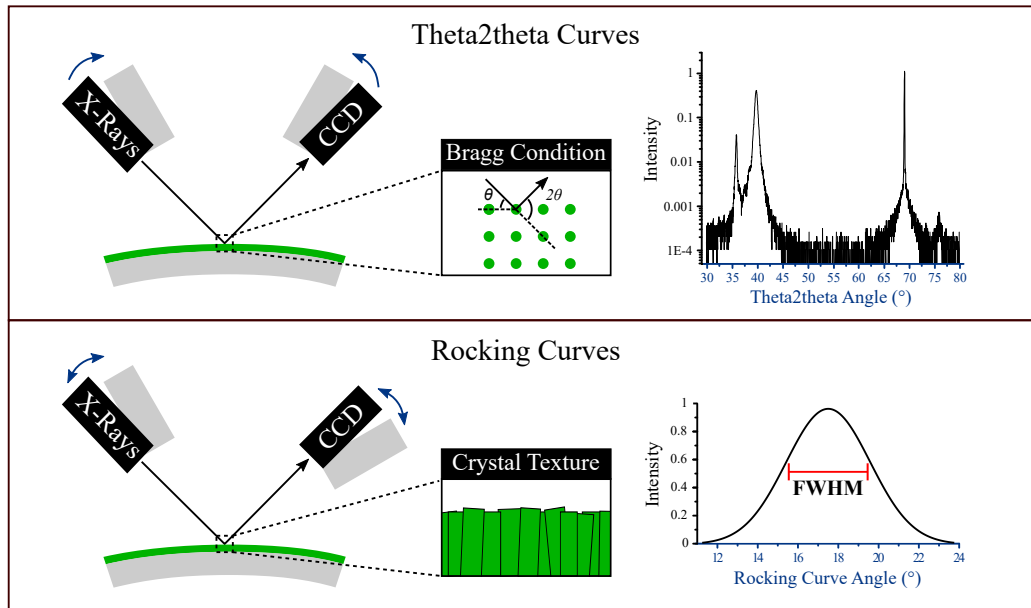


Figure 2.1 – Schematics describing methods to measure theta2theta and rocking curves. (A) theta2theta curve measurements are created by scanning X-ray source and detector with the same angle θ and speed above the substrate. The diffraction peaks from polycrystalline thin films and the substrate are measured when the Bragg condition is met. A theta2theta curve measurements with peaks from AlN, Pt and the Si substrate, respectively, is shown. (B) Rocking curves are measured by setting the X-ray source and detector to meet the Bragg condition of a diffraction peak of interest, then tilting or 'rocking' the source and detector about that value. The FWHM indicates the distribution of grain tilt relative to the substrate surface normal. A rocking curve for AlN is shown.

In contrast to theta2theta curves, rocking curves focus on certain diffraction peaks to understand the alignment of the crystals relative to the substrate. A parameter that is usually taken from rocking curves is the FWHM, which is calculated by fitting the rocking curves with a Gaussian function. The FWHM indicates the distribution of the tilt of the grains relative to the substrate surface normal; the lower the FWHM, the less misaligned the grains and the higher the texture of the thin film in that crystal grain orientation. Rocking curves are useful measurements for polycrystalline piezoelectric thin films for determining the alignment of the crystallites, which is directly related to the piezoelectric response of the material.

Rocking curves are completed by fixing the angle between the source and detector such that the Bragg condition is met for a material and crystal orientation of interest. Then, keeping the fixed angle, the source and detector are tilted or 'rocked' about the normal to the substrate to measure the intensity of the diffracted X-rays as a function of the tilting angle. The method of conducting rocking curves and an example peak from an AlN thin film can be seen in Figure 2.1 B.

The value of interest from XRD measurements of AlN and AlScN thin films is the rocking curve FWHM of the AlN/AlScN (0002) diffraction peak, which, as discussed in the introduction, has been found to be correlated with piezoelectric response [61]. While a low rocking curve FWHM value does not necessarily mean the piezoelectric response will be high, it does act as a marker to determine whether processing was optimal or not.

In order to confirm the measurement error for the θ 2 θ and rocking curves, we completed seven measurements on a single wafer to measure the change in rocking curve FWHM and found a standard deviation of 0.1°. This value is used for all rocking curve FWHM measurements discussed in this chapter.

2.1.2 Thin Film Residual Stress

Stresses in thin films can develop from several sources, including: a crystal lattice mismatch and/or thermal expansion mismatch between the thin film and substrate (which may also be under stress), from defects within the thin film and from ion bombardment of the growing thin films (peening effect) [33, 53]. All of the above stress sources influence the growth and texture of the deposited thin film, and in the case of piezoelectric thin films, the piezoelectric response. A way to quantify the influence of these stress sources is through measurement of the residual stress, for example through XRD or wafer curvature measurements.

The sign and magnitude of residual stress can indicate whether the AlN and AlScN thin films will have a piezoelectric response and c-axis texture. Compressive residual stress has been correlated with higher piezoelectric response in AlN thin films [33], while none to slightly tensile stress minimized the density of abnormal grains and improved the piezoelectric response in AlScN thin films [152, 159].

In addition, residual stress in thin films also affect the mechanical properties and successful operation of later developed resonators. For example, for doubly clamped resonators, compressive thin films can lead to buckling of the beams, which completely alters their resonant behavior. Therefore, one must consider both the best sputtering deposition conditions and final device specifications when fabricating thin films.

The residual stress of the thin films was calculated by measuring the change in wafer curvature due to the thin film deposition (Toho Technology FLX 2320-S) and applying Stoney's formula, the definition of which can be found in Appendix A.1. In the sections below, negative stress values are compressive, while positive ones are tensile.

2.1.3 Film Thickness and Crystal Texture

The AlN and AlScN film thickness and grain texture were characterized by cleaving the Si substrates where the films were deposited, then imaging the cross section with SEM in either the secondary electron or InLens modes. Two SEMs were used during the characterization

(Zeiss Leo 1550 or Zeiss Merlin), which have resolutions of 5 nm and <1nm, respectively.

The crystal growth of the AlScN thin films were characterized by both normal and cross section SEM. In normal SEM imaging, the density of abnormal grains, which are grains that do not follow the wurtzite (0002) crystal growth, could be quantified. The columnar grain density and quality could be measured in cross section SEM. The thickness of AlScN was measured by analyzing the cross section images in an imaging processing program (ImageJ).

2.2 AlN Deposition Experiments

As discussed in Chapter 1, sputtering parameters such as sputtering power and substrate temperature as well as the substrate conditions can have a significant influence on the c-axis texture of AlN thin films. To confirm that the optimal sputtering parameters and substrate conditions for micron thick AlN thin films will generate highly textured nanometer thick AlN thin films, several parameters and conditions were tested:

- Sputtering Parameters
 - Ar gas concentration
 - Multistep deposition
 - Sputtering power
 - Substrate temperature
- Substrate Conditions
 - Bottom electrode thin film material
 - Seed layer material and thickness
 - Bottom electrode sputtering system

A few sputtering parameters were already optimized by other users of the sputtering system before these deposition tests, including the substrate pre-treatment, target-substrate distance, substrate bias and sputtering pressure. Substrates used during all the deposition tests were initially treated by a one minute Ar plasma cleaning within the sputtering system to remove any organic residues from the substrate surfaces.

The target-substrate distance was set at 50 mm and could not be altered in the sputtering system. To generate substrate bias voltages between 50-100 V, which was previously found to give the highest c-axis texture for AlN thin films in our sputtering system, a substrate bias voltage of 6 W was used. Finally, the base pressure in the sputtering system was 2 μ bar and the total gas flow was set to 50 sccm (Ar plus N₂ gas flows), which generating sputtering pressures between 3-4 mTorr.

To deposit most of the seed layers, bottom electrode layers and all the AlN actuation layers, a magnetron sputtering system capable of DC and DC pulsed sputtering (Pfeiffer Spider 600) was used. Four chambers are available in this sputtering system for insulator and metal thin film depositions, with one chamber dedicated to AlN and AlScN depositions.

All targets in the Spider have a minimum purity of 99.95% and in the case of the Al target for AlN depositions, the purity is 99.9995%. Before any deposition experiments, the sputtering targets were cleaned using standard recipes provided by the sputtering system to remove any surface contamination and prime the chamber for the depositions. An abbreviated catalog of the substrates created during the deposition experiments can be found in Appendix A.3.

2.2.1 Influence of Sputtering Machine Parameters on AlN C-Axis Texture

As discussed in Chapter 1, sputtering parameters such as sputtering power and substrate temperature can have a significant influence on the crystalline properties of AlN thin films. To confirm that the optimal sputtering parameters for microscale AlN thin films will generate highly textured AlN thin films at the nanoscale, four sputtering parameters were tested, which can be seen in Table 2.1.

An additional reason for testing the influence of the substrate temperature, beside confirming whether an improvement in c-axis texture occurs with increasing temperature, was to determine whether lower temperatures could be used without significantly deteriorating the crystallinity. Lowering the substrate temperature will decrease the thermal stress within the thin film and simplify the thin film fabrication, which can be necessary in the fabrication of NEMS.

To test the influence of each sputtering parameter, a series of 200 nm wet oxidized, (100) Si substrates were coated with four layers (full stack): 15 nm AlN seed layer, 25 nm Pt bottom electrode layer, 50 nm AlN actuation layer and 15 nm Pt top electrode layer. The Si substrates had no specific resistivity value, 100 mm in diameter and 525 μm thick.

We chose to use Pt electrodes and AlN seed layers during this deposition experiment to ensure that the substrate condition was ideal as possible and any changes to the AlN texture was therefore due to the sputtering parameters. All four layers were deposited sequentially within the same sputtering system and kept under vacuum between the layer deposition steps.

Table 2.1 – Sputtering parameters tested to measure their influence on AlN rocking curve FWHM. The deposition time is given in seconds. Multiple depositions mean that the deposition time was broken into two parts, denoted as part 1/part 2 in the table. The Ar gas concentration is defined as the percentage of the Ar gas flow comprising the total Ar plus N₂ gas flow. RT means room temperature.

Multistep Deposition Times (s)	Ar Gas Concentration (%)	Sputtering Power (W)	Substrate Temperature (°C)
50/10	0	1000	RT
40/20	20%	1250	200
60		1500	300
			350

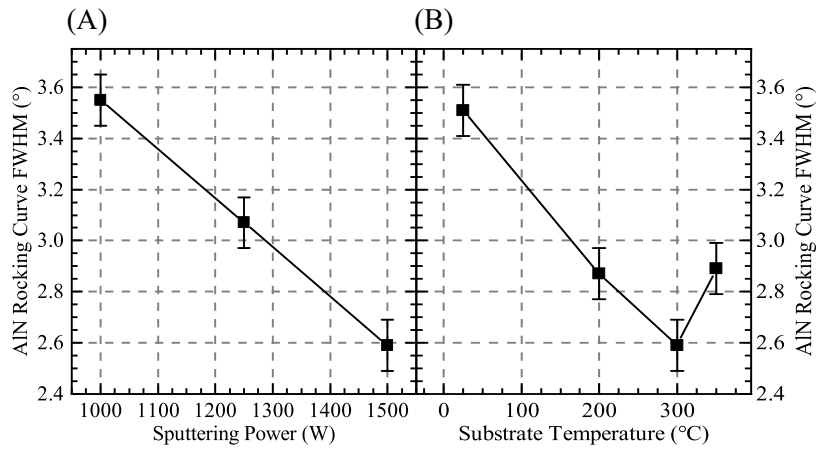


Figure 2.2 – Influence of sputtering power and substrate temperature on the AlN rocking curve FWHM. (A) Sputtering power versus AlN rocking curve, showing a clear decrease in the AlN rocking curve FWHM for increasing sputtering power. (C) Substrate temperature versus rocking curve FWHM, where the lowest measured AlN rocking curve FWHM was at 300°C.

The AlN seed layer was deposited under the following conditions: 20% Ar gas concentration, sputtering power of 1500 W and substrate temperature the same as the actuation layer substrate temperature, since the full stack of layers was deposited at once during the deposition experiment. The Pt bottom and top electrode layers were deposited at 350°C. The conditions for the AlN actuation layer depositions are discussed in the following paragraphs.

The influence of the four sputtering parameters was characterized by the measuring the AlN rocking curve FWHM. Theta2theta curve measurements taken of each substrate before the rocking curve measurements exhibited only the (0002) diffraction peak from AlN layers, the (111) diffraction peak from the Pt electrode layers and the (400) diffraction peak from the Si substrate. Residual stress measurements were also taken of the substrates, but since the full stack of layers was deposited at once, it was difficult to deconvolute the results to find the residual stress in the AlN actuation layer alone and the measured results did not demonstrate any trends versus the tested parameters.

When looking at the influence of sputtering power on deposited AlN thin films, a clear improvement is measured in the AlN rocking curve FWHM with increasing sputtering power (Figure 2.2 A). When measuring the influence of the sputtering power, the AlN actuation layer deposition conditions were: substrate temperature of 300°C, 20% Ar gas concentration, and a 50 seconds/10 seconds multistep deposition. The lowest rocking curve FWHM can be found at a sputtering power of 1500 W, the highest applicable value in the sputtering system. An important note on the results in Figure 2.2 A is that the effect of decreasing sputtering power on the deposition rate was not taken into account by altering the deposition time during the experiment. Therefore, there can be differences in the deposited film thickness which can

also influence the measured AlN rocking curve FWHM. However, we found that increasing the thickness of the AlN actuation layer to 100 nm compared to 50 nm in this deposition experiment only decreased the rocking curve FWHM by 0.2°, which means that the impact of sputtering on the crystalline properties is still significant.

Four different substrate temperatures were tested which spanned the temperature range of the sputtering system. During the substrate temperature test, the sputtering power was 1500 W, the Ar gas concentration was 20% and a 50 seconds/10 seconds multistep deposition. The deposition tests results can be seen in Figure 2.2 B; the AlN rocking curve FWHM improves with increasing substrate temperature until 300°C, after which the AlN rocking curve FWHM slightly increases with a substrate temperature of 350°C. It is not clear why the c-axis texture worsens after a substrate temperature of 300°C; we found no significant difference in the values of other sputtering parameters that could explain the results. Further deposition experiments should be completed to confirm the decrease in c-axis texture beyond 300°C.

Decreasing the substrate temperature to 200°C does not significantly deteriorate the AlN c-axis texture, but further decrease of the substrate temperature degrades the crystalline quality.

No significant trends are measured on the AlN c-axis texture when two Ar gas concentrations and three multistep depositions were tested; we therefore conclude that these two parameters have negligible impact on the AlN crystalline properties. On the other hand, increasing the sputtering power and substrate temperature are found to significantly improve the c-axis texture of the 50 nm thick AlN films.

2.2.2 Influence of Seed Layers on AlN C-Axis Texture and Piezoelectric Response

The next set of deposition experiments studied the influence of the seed layer material (Ti and AlN) deposited at room temperature and 350°C, as well as the seed layer thickness (AlN) on the rocking curve FWHM and piezoelectric response of the AlN actuation layer. To study these substrate conditions, a series of substrates were coated with a full stack comprised of: 15-100 nm AlN or Ti seed layer, 25 nm Pt bottom electrode layer, 50 nm AlN actuation layer and 25 nm Pt top electrode layer.

The AlN actuation layer deposition conditions were: 50 seconds/10 seconds multistep deposition, 20% Ar gas concentration, 350°C substrate temperature and 1500 W sputtering power. The Ti and AlN seed layers were deposited at 350°C; the sputtering power and Ar gas concentration for the AlN seed layers was the same as for the AlN actuation layer. The Pt electrodes were deposited at a substrate temperature of 350° C.

When comparing seed layers with a thickness of 15 nm deposited at 350°C, the AlN actuation layer rocking curve FWHM on Ti seed layers was 2.6°, compared to a lower value of 2.0° for AlN grown on AlN seed layers [115].

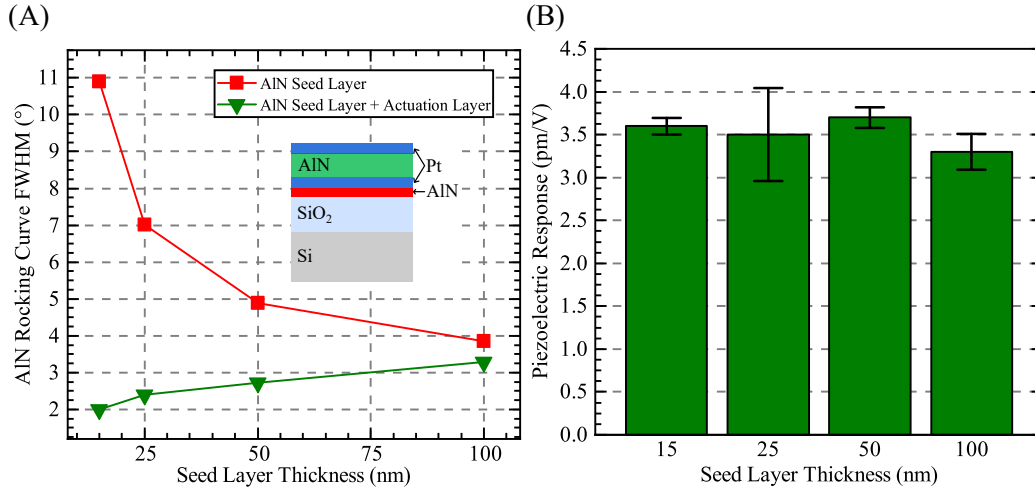


Figure 2.3 – Influence of AlN seed layer thickness on AlN actuation layer rocking curve FWHM and piezoelectric response. Inset schematic shows the thin films deposited as part of the full stack. The error bars were within the symbol size. (A) While the rocking curve FWHM of the AlN seed layer decreases with increasing seed layer thickness, the rocking curve FWHM of the actuation layer deposited on top of the AlN seed layer increases. (B) The piezoelectric response of the AlN actuation layer does not significantly change with different AlN seed layer thicknesses, in contradiction of the rocking curve results.

We then focused on the influence of the AlN seed layer thickness on the AlN actuation layer rocking curve FWHM. Four AlN seed layer thicknesses between 15-100 nm were tested with 50 nm thick AlN actuation layers deposited above the seed layers. Rocking curves were measured on substrates with the AlN seed layers of various thicknesses alone, as well as on separate substrates where a full stack was deposited. Therefore, on substrates where the full stack was deposited, diffraction data is collected from both the AlN seed and actuation layers.

The results of the rocking curve characterization on AlN seed and actuation layers can be found in Figure 2.3 A. On the one hand, as the AlN seed layer thickness increases, the rocking curve FWHM of the layer decreases due to increasing c-axis texture with increasing film thickness [61]. On the other hand, the rocking curve FWHM of the AlN actuation layers deposited on AlN seed layers slightly increases with increasing AlN seed layer thickness. These results appear at first to be counter-intuitive, since a more crystalline seed layer should improve the c-axis texture of the Pt bottom electrode and AlN actuation layers.

To determine whether the piezoelectric properties of the AlN thin films had been affected by the AlN seed layer thickness, the piezoelectric response was measured by fabricating electrodes through the full stack with standard photolithography and dry etching, then measuring the top electrode displacement when actuated in a double beam interferometer system in another laboratory. The details on the setup can be found in the work of Kholkin *et al.* [63]. Electrode diameters between 200-750 μm were fabricated to take into account the electrode

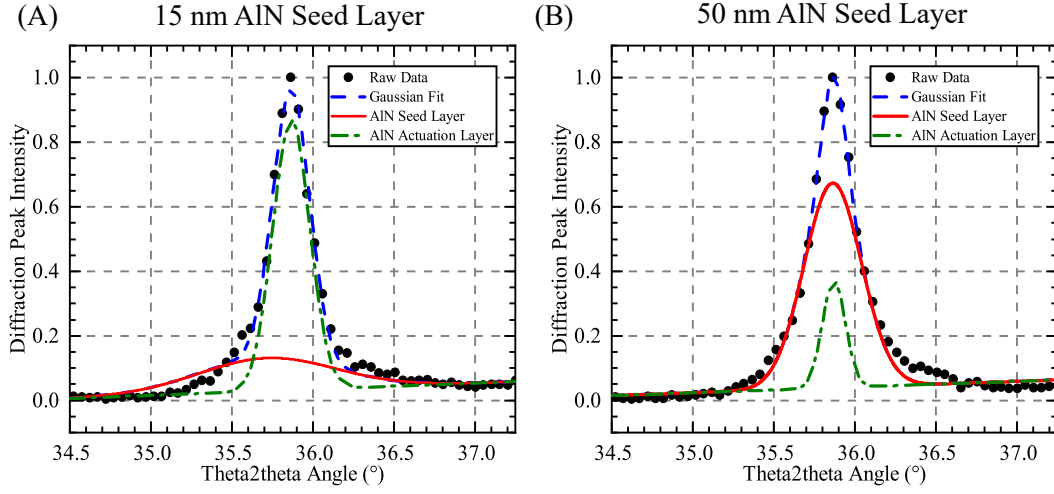


Figure 2.4 – Two term Gaussian analysis to deconvolute the (0002) theta2theta diffraction peak contributions from each AlN layer. The measured (0002) theta2theta diffraction peak (black circles) was deconvoluted by a two term Gaussian (blue dashed line) to determine the contributions from the AlN seed layer (red solid line) and AlN actuation layer (green dashed line). (A) A 15 nm thick AlN seed layer only slightly impacts the theta2theta diffraction peak analysis. (B) The diffraction from a 50 nm thick AlN seed layer significantly impacts the Gaussian analysis of the (0002) diffraction peak.

size effect [63] and COMSOL simulations were used to calculate the piezoelectric response based on fitting the measured displacement of the electrodes during actuation [167].

We find that increasing the thickness of AlN seed layer does not significantly influence the piezoelectric response of the AlN actuation layers [115], as can be seen in Figure 2.3 B . An average $d_{33,f}$ of 3.5 ± 0.17 pm/V was measured for the AlN actuation layers, which is close to values found in the state of the art [75].

Since the piezoelectric response does not significantly change with increasing AlN seed layer thickness, we believe that the AlN seed layers are deviating the rocking curve characterization by shadowing the diffraction data from the actuation layer during theta2theta measurements. By analyzing the (0002) theta2theta diffraction peak from the AlN seed layers alone, a two-term Gaussian, the equation of which can be found in Appendix A.4, was applied to the (0002) theta2theta diffraction peak from the actuation layers deposited on the seed layers to deconvolute the contributions from each layer.

For example, the two-term Gaussian fitting of the (0002) theta2theta diffraction peak of a full stack with a 15 nm AlN seed layer and 50 nm AlN actuation layer can be seen in Figure 2.4 A. The individual contributions from the AlN seed layer (solid blue line) and actuation layer (dashed green line) based on the two-term Gaussian fit (dashed red line) are plotted separately.

When the AlN seed layer thickness is much smaller than the actuation layer thickness, the diffraction from the seed layer only slightly contributes to the total (0002) diffraction peak. As the AlN seed layer thickness increases, for example with a 50 nm thickness as seen in Figure 2.4 B, its contribution to the total (0002) θ diffraction peak significantly. As the rocking curve FWHM of the seed layers is larger than for the actuation layers, increasing the seed layer's contribution to the (0002) θ diffraction peak increasingly affects the rocking curve characterization. While increasing the seed layer thickness may overall improve the crystallinity of the proceeding layers, for accurate rocking curve characterization of the AlN actuation layer, the AlN seed layer thickness should be significantly thinner than the AlN actuation layer to minimize its influence.

2.2.3 Influence of Substrate and Sputtering System on AlN Rocking Curve FWHM

Based on the literature review on AlN sputtering optimization seen in Chapter 1, it is clear that the substrate and seed layer play a strong role in the quality of AlN thin films. Therefore, the deposition experiment discussed in the previous section was expanded to fully confirm the influence of the substrate conditions on the c-axis texture of AlN, by testing two seed layers, three bottom electrode thin films and two seed layer/bottom electrode sputtering systems. The tested substrate conditions can be found in Table 2.2. All the possible combinations of these three substrate conditions were tested, except two: Ti seed layers under Al bottom electrode thin films deposited in the Spider sputtering system, which could not be configured into the system; and AlN seed layers could only be deposited in the Spider sputtering system.

The different seed layers and bottom electrode thin films were chosen based on the frequency of their use in literature. In particular, we wanted to see if a high AlN c-axis texture could be achieved on Mo and Al bottom electrode thin films as well in our sputtering system.

Two different bottom electrode sputtering machines (Spider and DP650) were tested to compare the effect of each sputtering system on the bottom electrode thin film properties and thereby AlN deposited on top. The DP650 contains only one sputtering chamber, with smaller targets, smaller target substrate distance and a shutter between the target and substrate, compared to the Spider sputtering system. The differences in the setup of each sputtering should influence the crystallinity and roughness of the deposited bottom electrode thin films.

The deposition experiments themselves were separated into two parts: deposition of the seed layer/bottom electrode thin films; and deposition of AlN/top electrode thin films. The thicknesses of the four layers in the full stack were: 15 nm seed layer, 25 nm bottom electrode thin film, 100 nm AlN actuation layer and 100 nm top electrode thin film. The substrates were 200 nm wet oxidized Si. All AlN seed layers were deposited in the Spider at room temperature with 20% Ar gas concentration and 1500 W sputtering power. Ti seed layers were deposited at room temperature in either the Spider or DP 650, depending on which system was used to deposit the bottom electrode thin films.

The bottom and electrode thin films were also deposited at room temperature, in comparison to 350°C in the previously discussed deposition experiments. This was done to better simulate the deposition conditions that are used during fabrication of many NEMS and MEMS, which involves liftoff of the bottom electrode to minimize the top and bottom electrode overlap area. A small deposition test prior to this one found no significant difference in the AlN rocking curve FWHM between Pt electrode thin films deposited on an AlN seed layer at room temperature and 300°C. The top electrode thin film was Al except when the bottom electrode thin film was Al, in which case Mo was used to avoid overlap of θ 2 θ diffraction peaks.

The AlN actuation layers were deposited with the following sputtering parameters: 1500 W sputtering power, 20% Ar gas concentration, 300°C substrate temperature and a continuous deposition time.

The influence of the bottom electrode rocking curve FWHM on the rocking curve FWHM of AlN can be found in Figure 2.5 A. In all θ 2 θ curve measurements, only the AlN (0002) diffraction peak was measured. We find that Pt bottom electrode layers generated the lowest AlN rocking curve FWHM, independent of the type of seed layer and electrode sputtering system. A low AlN rocking curve FWHM also occurs for Pt bottom electrodes with worse texture, which indicates the surface roughness of the Pt layer could play a part in the results.

A fairly low AlN rocking curve FWHM is achieved on Mo bottom electrode thin films with a Ti seed layer deposited in the Spider sputtering system. However, the Mo bottom electrode thin films are more strongly influenced by the sputtering system and seed layer and generally perform less well compared to Pt bottom electrodes. As a body-centered cubic metal, Mo is expected to grow roughness and less crystalline than face-centered cubic Pt, but it has been shown in literature that highly c-axis textured AlN films can still be achieved [103].

In the case of Al bottom electrodes, the crystallinity of the electrode was so low that rocking curves could not be measured. It is not clear why the crystallinity of the Al bottom electrodes was not higher. It has been shown previously in literature that Al bottom electrodes perform slightly less well than Pt bottom electrodes [33], but our results show a much more significant difference. One conclusion from these results is that further sputtering optimization of the Mo and Al layers must be achieved to increase their texture and therefore the c-axis texture of AlN grown above.

Table 2.2 – Tested seed layers, bottom electrode thin films and seed layer/bottom electrode sputtering systems versus AlN rocking curve FWHM. All possible combinations of the three conditions were fabricated except for Ti seed layers with Al bottom electrodes in the Spider sputtering system, since this was not a possible configuration in the system.

Seed Layer	Bottom Electrode Material	Sputtering System
AlN	Pt	Spider
Ti	Mo	DP650
	Al	

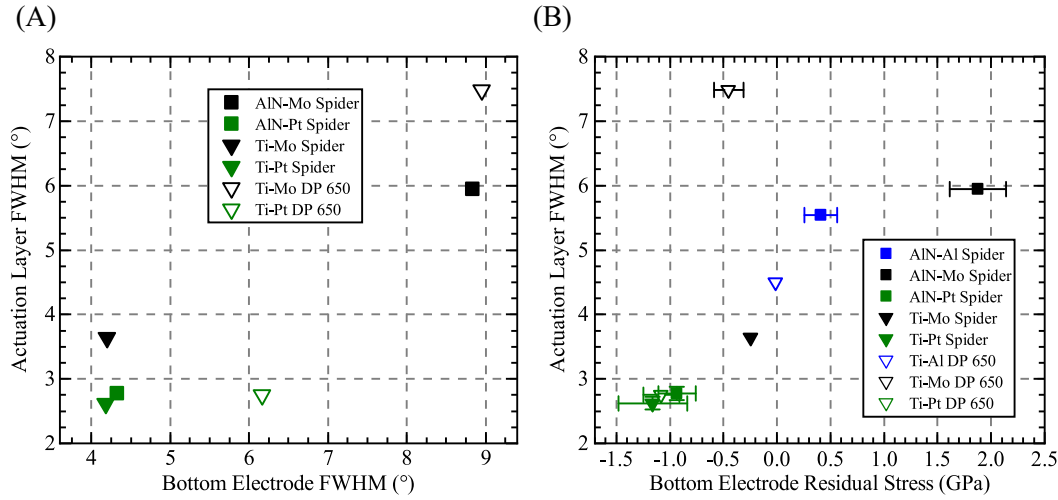


Figure 2.5 – Influence of seed layers, bottom electrode thin films and bottom electrode sputtering systems on texture of 100 nm AlN. The symbol colors designate the bottom electrode metal, the shape the seed layer and solid/hollow symbols for each sputtering system. In the legend label, the substrate conditions are listed as: seed layer-bottom electrode sputtering system. The error bars are within most of the symbols, except in the case of some residual stress measurements. (A) AlN rocking curve FWHM is correlated with low bottom electrode rocking curve FWHM. Lowest AlN rocking curve FWHM values were found with Pt electrodes, independent of the seed layer or sputtering system. Mo bottom electrode thin films generated larger AlN FWHM, except in the case when a Ti seed layer and the Spider sputtering system are used. The crystallinity of the Al bottom electrodes was too low for rocking curves to be measured. (B) AlN rocking curve FWHM versus bottom electrode thin film residual stress. While there appears to be a correlation between more compressive bottom electrodes and lower AlN rocking curve FWHM, more experiments with varying residual stress in one electrode material should be completed before drawing further conclusions.

The c-axis texture of AlN appears to be correlated with the bottom electrode stress, as seen in Figure 2.5 B. However, more experiments with varying residual stress on one bottom electrode material are required in order to better understand why this correlation occurs.

2.2.4 Conclusions on AlN Sputtering Optimization

Based on the deposition experiments discussed above, a few conclusions can be made. Increasing the sputtering power and using a substrate temperature of 300°C generates the lowest AlN rocking curve FWHM and Pt electrodes consistently provided the lowest rocking curve FWHM values compared to Mo and Al electrodes. Ti or AlN seed layers generate similar AlN rocking curve FWHM values when they are deposited at room temperature, but AlN seed layers are better when depositing at 300°C. While AlN seed layers deposited at 300°C offer promising results for the c-axis texture of AlN actuation layers, to minimize deviation of the rocking curve characterization, they should be significantly thinner than the AlN actuation

layers. The influence of sputtering power, substrate and substrate conditions on the c-axis texture of micron thick AlN films has been confirmed for 50-100 nm thick AlN films.

To summarize, the best AlN rocking curve FWHM values were measured with:

- High sputtering power of 1500 W
- Substrate temperature of 300°C
- AlN seed layers when deposited at 350°C
- AlN and Ti seed layers when deposited at room temperature
- Pt electrodes compared to Al or Mo electrodes
- Increased deposition temperature for Pt electrodes compared to room temperature

One issue seen when comparing depositions from separate experiments was the sputtering system variability in depositing thin films with consistent characteristics when identical sputtering parameters are used. One example is that with increasing sputtering power, the deviation between the programmed sputtering power and achieved sputtering power increased. Another is that the achieved substrate bias power was usually 1 W lower than the programmed value and the substrate bias voltage fluctuated between 50-100 V during the different deposition experiments. The substrate bias has a strong influence on the residual stress of the AlN thin films, which may be why no clear trends could be measured in the residual stress. The substrate bias fluctuations may have impacted the influence of more subtle sputtering parameters such as multistep deposition and the gas flow ratio. More tests on different gas flow ratios and multistep depositions should be completed to better understand their influence on the AlN thin film characteristics, but with a more stable sputtering system.

2.3 Al_{0.6}Sc_{0.4}N Deposition Experiments

2.3.1 Impact of Ar Gas Concentration and Substrate Bias on Al_{0.6}Sc_{0.4}N Film Properties

One aim of this doctoral work is to fabricate piezoelectric layers on the nanoscale for NEMS. However, since AlScN is a relatively new material and has been seen in literature to be more challenging than AlN to deposit with a good (0002) texture, initial deposition experiments were completed with 1 μm thickness. By optimizing the growth of AlScN thin films on the microscale, the thickness can then be decreased to try to implement into NEMS devices.

AlScN is more challenging than AlN to grow due to the Sc addition destabilizing the wurtzite crystal growth. As discussed in Chapter 1, beyond a Sc concentration of approximately 43%, the crystal growth changes from hexagonal to cubic phase. Below a Sc concentration of 43%, abnormal grains may be generated if the deposition parameters or substrate are not optimal, which are detrimental to the total piezoelectric response of the AlScN thin film [170]. Abnormal grain growth occurred during most of the deposition experiments and are always referred to as abnormal, compared to the regular wurtzite (0002) AlScN grain growth.

Chapter 2. Sputtering Optimization of AlN and Al_{0.6}Sc_{0.4}N Thin Films

All depositions were completed using the Spider sputtering system with a single AlSc target and Sc concentration of 40 at% (52.6 wt%). Before the deposition experiments, the AlSc target composition was confirmed by depositing AlSc onto a substrate without a nitrogen gas flow and then measuring the thin film composition through energy-dispersive X-ray spectroscopy (EDX). A slightly higher Sc concentration of approximately 41% was measured compared to the supplier information of 40%, but the values overlap given the large standard deviation of the measurement (3%). Unless otherwise specified, the discussion of AlScN thin films will be with 40% Sc concentration.

The full stack of thin films deposited during the AlScN deposition experiments was: 10 nm Ti seed layer, 100 nm Pt bottom electrode thin film, approximately 1 μ m AlScN and 100 nm Ti top electrode. All deposition experiments were completed by depositing the full stack at once. AlScN sputtering parameters were 1500 W for the sputtering power and 300°C for the substrate temperature. A short Ar plasma cleaning was completed before the seed layer deposition to remove any organic residues from the substrate surfaces.

The characteristics of 1 μ m thick AlScN thin films deposited by reactive sputtering were measured versus different Ar:N₂ gas flow ratios (also discussed as Ar gas flow concentration) and RF substrate bias powers, based on knowledge from the AlN deposition experiments and the literature review. The total gas flow during sputtering was kept constant at 50 sccm and Ar gas concentration was varied between 0-60%.

The tested substrate bias powers were between 2-6 W, which translated to a potential between -50 to -100 V during the AlScN depositions. Depending on the calibration of the RF power source in the sputtering system, applied substrate bias powers would be translated into larger or smaller bias voltages. Therefore, the substrate bias is discussed below in terms of the absolute magnitude of the average substrate bias voltage. A catalog of all the substrates used in deposition experiments and the deposition parameters can be found in Table 2.3.

The AlScN thin films were characterized by rocking curves and residual stress. Compared to the 50-100 nm AlN thin films studied in the previous section, the AlScN layers comprise more than 80% of the deposited film stacks in the deposition experiments. Therefore, the curvature-based residual stress measurements should give a fairly accurate estimate of the magnitude and trends in the AlScN layers. Additionally, the films were analyzed by normal and cross section SEM to understand the columnar grain texture and density of abnormal grains.

Table 2.3 – Sputtering parameters during AlScN deposition experiments.

Substrate Temperature (°C)	Ar Gas Concentration (%)	Sputtering Power (W)	Substrate Bias Power (W)
300	0-60%	1500	2-6

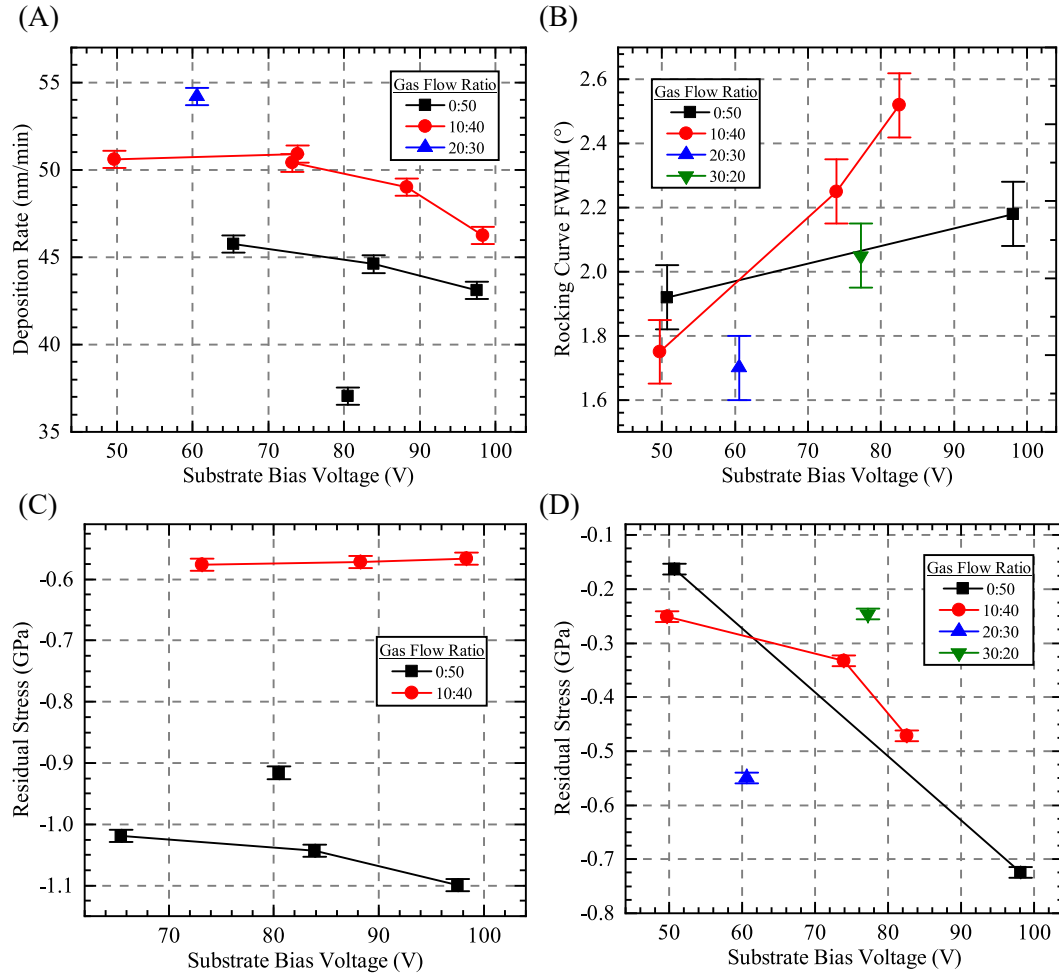


Figure 2.6 – Measured deposition rate, rocking curve FWHM and residual stress in AlScN deposition experiments. The legend denotes the tested gas flow ratios (Ar gas concentration): 0:50 (0%), 10:40 (20%), 20:30 (40%) and 30:20 (60%). (A) AlScN deposition rate versus substrate bias voltage for different Ar:N₂ gas flow ratios. Deposition rate increased with increasing Ar concentration. Extremely low deposition rate data point in 0:50 Ar:N₂ gas flow ratio is an outlier caused by the shift in bias voltage during deposition experiments as discussed before. (B) Rocking curve FWHM is found to have a linear relationship with substrate bias voltage, for a given Ar:N₂ gas flow ratio. The lowest FWHM of 1.70° was found with 40% Ar concentration, but its error bars overlap with a result from 20% Ar concentration. (C) Deposition experiment with two different Ar gas concentrations (0 and 20%). Increasing the Ar gas concentration decreases the compressive stress and alters the trend between residual stress and substrate bias voltage. (D) Second deposition experiment with an expanded range of Ar gas concentrations (0-60%). Significantly different trends and residual stress magnitudes are found compared to the first deposition experiment. The substrate bias voltage most strongly influenced the residual stress values compared to the Ar gas concentration in the first experiment.

The measured deposition rate for three different Ar:N₂ gas flow ratios versus substrate bias voltage can be seen in Figure 2.6 A. The AlScN deposition rate increases with increasing Ar gas flow, due to the higher sputtering efficiency of the AlSc target. For a Ar:N₂ gas flow ratio of 10:40, a trend of slightly decreasing deposition with increasing substrate bias can be seen. A similar trend is also seen for a gas flow ratio of 0:50 Ar:N₂, although there is an outlier which cannot be explained by the sputtering system conditions.

The influence of four different Ar:N₂ gas flow ratios was measured versus the AlScN rocking curve FWHM (Figure 2.6 B). The lowest FWHM measured was 1.70° for a gas flow ratio of 20:30 Ar:N₂, though the values from Ar concentrations of 0% and 20% generate similar results. For 0:50 and 10:40 Ar:N₂ gas flow ratios, a decrease in AlScN rocking curve FWHM can be seen when the substrate bias voltage decreases. The decrease in FWHM with lower substrate bias voltage correlates with the results from Mayrhofer et al, who found the highest piezoelectric coefficient at zero substrate bias [167]. However, they measured a maximum piezoelectric coefficient at 25% Ar concentration, while we found 40% Ar concentration to offer the lowest FWHM. More studies with lower bias voltage are necessary to confirm the trend, particularly for 40% and 60% Ar concentrations.

Two deposition experiments, completed on different days, were studied separately to measure the change in AlScN residual stress versus gas flow ratio and substrate bias voltage. The standard deviation of the residual stress in these deposition experiments was roughly 5%. In the first deposition experiment (Figure 2.6 C), two gas flow ratios were tested with three different substrate bias powers. While the residual stress does not significantly change across different substrate bias voltages when a Ar:N₂ gas flow ratio of 10:40 is used, it slightly decreases with increasing substrate bias voltage for a gas flow ratio of 0:50. The same outlier data point as discussed in Figure 2.6 A can be seen to behave differently than the other data points.

In the second deposition experiment (Figure 2.6 D), the range of gas flow ratios was increased from two to four, including the two measured in the first deposition experiment. In the case of 10:40 and 0:50 Ar:N₂ gas flow ratios, the residual stress increases with increasing substrate bias voltage, while no clear trend can be seen for the 20:30 and 30:20 gas flow ratios since only single data points were collected. Comparing the results in Figure 2.6 C and D, similar trends can be found for the 0:50 Ar:N₂ gas flow ratio but not for the 10:40 gas flow ratio. As discussed for the AlN depositions, variability in the sputtering system is the most likely cause for the changes in residual stress and the outlier in the deposition rate. Therefore, it is difficult to draw further conclusions on the residual stress measurements without further deposition experiments.

When comparing the rocking curve FWHM and residual stress measurements in Figure 2.6 B and D, one can see that decreasing the compressive stress leads to smaller rocking FWHM values, which correlates with results seen in literature, where AlScN with higher tensile stress has a higher piezoelectric response [152, 159].

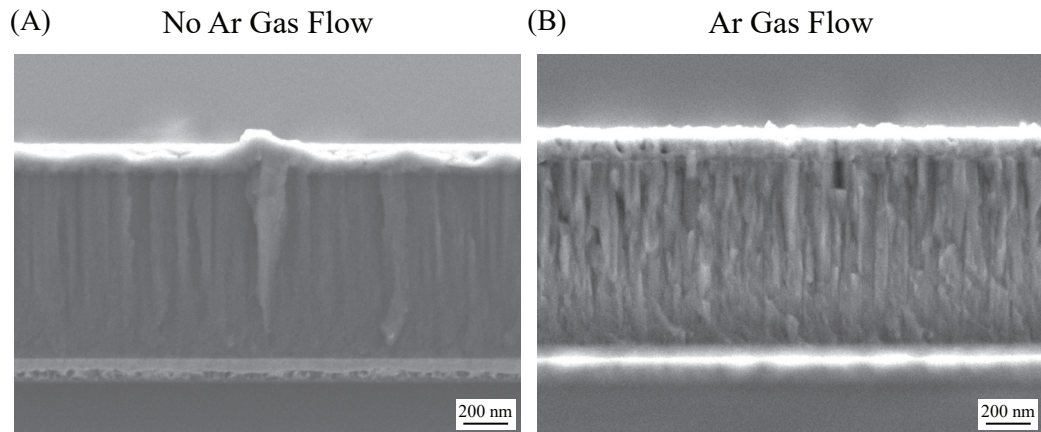


Figure 2.7 – Influence of Ar gas concentration on $\text{Al}_{0.6}\text{Sc}_{0.4}\text{N}$ grain density and c-axis texture. Bright layers in SEM images are bottom and top electrodes. Substrate bias power was 6 W in both images. (A) Highly dense grain texture for AlScN films for depositions without an Ar gas flow, but abnormal grains appear in the film after approximately 200 nm of columnar grain growth. The abnormal grains grow faster than columnar grains and protrude from the AlScN film thickness. (B) Sputtering with 20% Ar concentration greatly decreases the grain density, particularly as the thickness increases. Voids are visible near or at the top of the AlScN layer. However, no abnormal grains are present.

2.3.2 Study on Columnar Grain Texture and Density of Abnormal Grains

High columnar grain density in AlN and AlScN thin films is important for generating a strong piezoelectric response. To study the influence of Ar gas concentration and substrate bias on grain density and growth, normal and cross section SEM analysis is used.

The Ar gas concentration during sputtering of the AlScN thin films had a significant effect on the columnar grain texture and the appearance of abnormal grains, which can be seen in Figure 2.7. With zero Ar gas concentration, the wurtzite (0002) grains were columnar and dense. However, abnormal grains started to grow after approximately 200 nm of AlScN had been deposited. For example, one abnormal grain can be seen in Figure 2.7 A protruding beyond the AlScN layer.

When Ar is introduced during the AlScN sputtering, the AlScN grain growth significantly changes. One improvement with introducing an Ar gas flow is that little to no abnormal grains appeared. However, the columnar grain density is lower, to the point of generating voids near the top of the AlScN layer. Having voids within the thin film means that parts of the AlScN layer are not generating a piezoelectric response and therefore generating a less effective piezoelectric layer. In addition, voids increase the risk of electrical shorts between the bottom and top electrodes due to filling of the voids during the top electrode deposition.

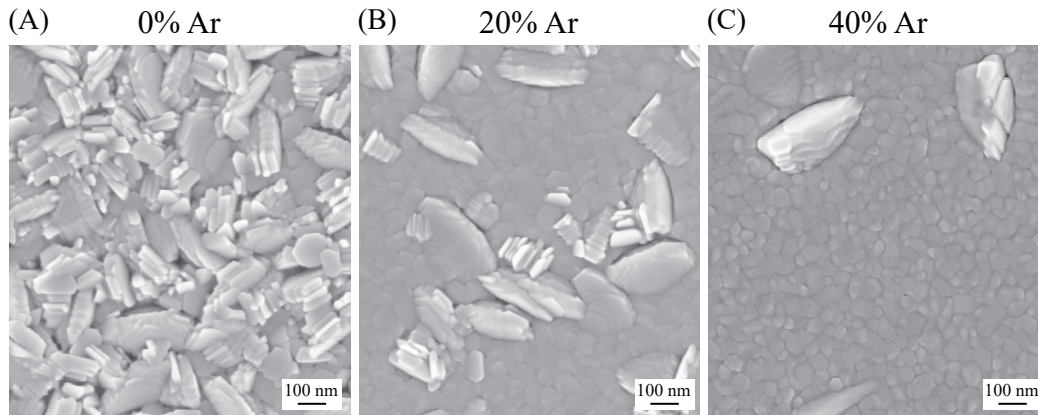


Figure 2.8 – Density of abnormal grains imaged by normal SEM versus no Ar gas concentration during sputtering (A), 20% Ar gas concentration (B) and 40% Ar gas concentration (C). The density of abnormal grains decreases with increasing Ar gas concentration. The abnormal grain size is approximately the same in the different Ar gas concentrations.

The abnormal grains were also visible in normal SEM imaging due to the protrusion of the abnormal grains into the top electrode, which can be seen in Figure 2.8. A clear decrease in the density of abnormal grains occurs with increasing Ar gas flow concentration from 0% (A) to 20% (B) to 40% (C).

The influence the substrate bias voltage and Ar gas concentration on the density of abnormal grains can be found in Figure 2.9. The density was calculated as number of abnormal grains per square micrometer. A negative linear relationship was found between substrate bias voltage and density of abnormal grains under pure nitrogen sputtering conditions (Figure 2.9 A). When increasing the Ar gas concentration, a strong decrease in the density of abnormal grains was measured, similar to the decrease in rocking curve FWHM seen in Figure 2.6 B.

The impact of the Ar gas concentration on the abnormal grain density is still an open question in the literature. In the case of AlN thin films, the lower the Ar gas concentration, the higher the energy of the ions bombarding the substrate, which generates a denser, better c-axis textured film [33]. However, for AlScN thin films, the target-substrate distance and substrate bias have been shown to influence the optimal Ar gas concentration from 0-50% [167, 170]. For the sputtering parameters that we have set in our sputtering system, such as the target-substrate distance, sputtering power and sputtering pressure, having a non-zero Ar gas concentration appears to be necessary to minimize the growth of abnormal grains.

It is important to note that SEM analysis is not a foolproof method of characterizing the grain growth of AlScN, since imaging is done in small areas compared to the diameter of the substrate. It is always possible that the areas imaged have locally different conditions than other parts of the substrates. Top view SEM images were taken at every substrate center, middle and edge with two to three magnifications, while the cross section SEM images were taken near

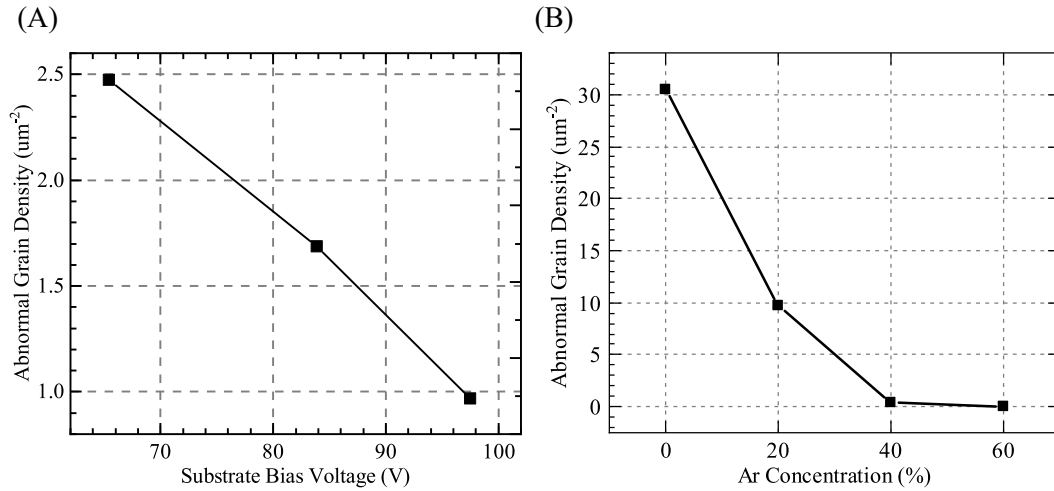


Figure 2.9 – Influence of substrate bias voltage and Ar gas concentration on density of abnormal grains. (A) A linear relationship is found between the density of abnormal grains versus substrate bias voltage for 0% Ar gas concentration. (B) The density of abnormal grains significantly decreases with increasing Ar concentration.

the center of the substrate, depending on the substrate cleavage. Before images were taken, the substrates and substrate cross sections were inspected in several areas to get a full sense of the AlScN characteristics both in normal and cross section SEM. For example, one noted behavior was that on substrates where abnormal grains occurred, the density of abnormal grains increased from the center to the edge of the substrate. This behavior is most likely due to the asymmetry of the sputtering plasma and the dimensions of the sputtering chamber and target, which induce the growth of increasingly tilted regular grains when moving from the substrate center to edge. The increased grain tilt may then further impact the hexagonal grain growth and more easily induce the growth of abnormal grains.

2.3.3 Conclusions on $\text{Al}_{0.6}\text{Sc}_{0.4}\text{N}$ Sputtering Optimization

A few conclusions can be drawn from the AlScN deposition experiments. Increasing the Ar gas concentration during the depositions increases the AlScN deposition rate, but its influence on the AlScN rocking curve FWHM and residual stress is less clear. Decreasing the substrate bias voltage slightly decreases the deposition rate, AlScN rocking curve FWHM and residual stress.

The columnar grain texture was denser when little or no Ar gas flow was included in the depositions, but more abnormal grains appeared at lower Ar gas flow levels. The rocking curve FWHM also increased at lower Ar gas flow levels, which means that a dense columnar grain growth does not necessarily lead to improved (0002) texture. When taking into account the substrate bias voltage, an inverse relationship is found between the rocking curve FWHM and the density of abnormal grains. Having a high Ar gas concentration and middle to low

substrate bias voltage would generate a fairly low density of abnormal grains while offering a low AlScN rocking curve FWHM.

The effect of abnormal grains in AlScN thin films can be compared to the presence of non-(0002) orientations in AlN thin films: if abnormal grains are present, then the method of using rocking curve FWHM to gauge the magnitude of the potential piezoelectric response in the AlScN thin film is no longer accurate. Even if most of the AlScN thin films is highly c-axis textured and a low rocking curve FWHM is measured, having some density of abnormal grains means that some part of the material is not contributing to the total piezoelectric response. Rocking curves only indicate the distribution of tilt angles the (0002) grains have compared to the substrate surface normal; they cannot take into account other crystal orientations or abnormal grains within the thin film.

An interesting difference between the AlN and AlScN thin film growth is that less compressive stress in the AlScN thin films seems necessary to have a high c-axis texture, compared to AlN thin films. These results correlate to work completed by Mertin et al., who showed that lower compressive stress generates a higher piezoelectric response for AlScN thin films with lower Sc concentrations [159]. There is significant difference in the optimal residual stress values for AlN versus AlScN thin films, which indicates that optimal deposition conditions for AlScN thin films may be substantially different than for AlN thin films.

During all the AlN and AlScN deposition experiments, the achieved substrate bias power was approximately 1 W lower than the programmed substrate bias power and would fluctuate between different experiments and within the experiments themselves. The fluctuations in substrate bias are an issue because then the depositions conditions themselves are not fully stable and it is more difficult to draw conclusions from different deposition experiments. A similar issue was seen in the disparity between the programmed and achieved sputtering power seen during the AlN deposition experiments. The discrepancies and fluctuations are mostly due to the sputtering system itself, which was modified from an industrial application and does not have the best control on the sputtering parameters.

2.3.4 Etch Tests on Al_{0.6}Sc_{0.4}N Thin Films

To electrically characterize some of the AlN and AlScN thin films, top electrodes with various diameters were fabricated by dry etching. Some work was previously completed for fabricating electrodes on AlN thin films for piezoelectric response measurements [115]. A photolithography was first completed with 8 μm of photoresist AZ9260. Then, the top Ti electrode and AlN/AlScN layer were dry etched with an ICP etcher (STS Multiplex ICP). The etch rate of AlScN with 40% Sc concentration was measured using three different etch chemistries and RF power. The etch test results can be found in Table 2.4. Using the recipe with the highest etch rate, chips with AlN or AlScN thin films were etched and the photoresist was removed by a combination of O₂ plasma etching and wet etching with 70°C Remover 1165.

Table 2.4 – Dry etch tests to find the highest etch rate for AlScN with 40% Sc concentration.

Cl₂ (sccm)	BCl₃ (sccm)	Ar (sccm)	RF Power (W)	Etching Rate (nm/min)
10	10	0	200	42.0
20	20	0	200	49.6
25	15	70	150	10.0

Some fencing was visible during microscope analysis of the electrode on all chips, but proved not to be an issue later during the electrical characterization. On each chip, several electrodes were tested through current-voltage (IV) sweeps to measure their resistance. The DC characterization setup is described in more detail in Chapter 3. All measured resistances were on the order of a few GΩ and no electrical breakdown could be measured up to an applied voltage of 75 V on AlScN thin films with 40% Sc concentration.

2.4 Conclusion

In this chapter, the impact of substrate and sputtering parameters on AlN and AlScN thin films was studied, particularly by using rocking curves, residual stress and SEM analysis. For 50 and 100 nm thick AlN thin films, a sputtering power of 1500 W, substrate temperatures of 300°C and Pt bottom electrode thin films with either AlN or Ti seed layers were found to provide the lowest rocking curve FWHM values. The influence of Ar:N₂ gas flow ratio and multistep deposition on rocking curve FWHM was inconsistent across the different deposition experiments.

For 1 μm AlScN thin films, decreasing substrate bias voltage and increasing the Ar gas concentration decreased the rocking curve FWHM, as well as the residual stress in the full stack. Increasing both the substrate bias voltage and Ar gas concentration decreased the density of abnormal grains. Therefore, a compromise in the sputtering parameters would need to be made to have both a low rocking curve FWHM and low density of abnormal grains in sputtered AlScN thin films.

One overall conclusion that can be made about the above work is the importance of the stability of the sputtering system to deposit thin films with consistent characteristics. While trends in sputtering parameters could be measured in one deposition experiment, when repeating similar conditions during different processing iterations, different results could occur. In particular, this was the case when altering the gas flow ratio or the substrate bias power. In the future, it is important to try to stabilize the sputtering system or switch to a more stable system for deposition experiments. Despite the fluctuations in sputtering parameters, it was possible to extract some trends and deposit AlN and AlScN thin films with characteristics similar to the state of the art.

3 Flexoelectric Actuators Based on Amorphous HfO_2

This chapter focuses on the fabrication and measurements of flexoelectric actuators based on 40 nm thick amorphous HfO_2 films. First, the fabrication is described in detail, including the wafer and chip designs, developed process flow, as well as issues and successes during the fabrication itself. Then, the electrical and crystallographic characterization of the deposited thin films is reviewed. Afterwards, the experimental setup for characterizing the deformation of the flexoelectric actuators is described, as well as the method for calculating the effective flexoelectric coefficient. Finally, a surface fit is used to calculate the effective flexoelectric coefficient of amorphous HfO_2 based on the measurement of seventy-four cantilevers.

3.1 Motivation for Flexoelectric Actuation with High-K Dielectrics

The flexoelectric effect has been measured in several ferroelectric and paraelectric materials and was recently demonstrated as a method of actuation for NEMS with single crystal SrTiO_3 [16]. However, compared to AlN thin films, ferroelectrics like PZT and paraelectrics like SrTiO_3 are more challenging to fabricate in thin film form due to needing high deposition temperatures and specific substrate conditions [40]. For flexoelectric transduction to become a viable, potentially commercialized alternative to piezoelectric transduction in NEMS, there is a need to develop flexoelectric thin films that can be deposited with mature, CMOS-compatible processes. High-k dielectrics, which are dielectrics with a relative permittivity larger than SiO_2 , are a natural choice based on their mature processing techniques and their current investigation for replacing various materials in CMOS applications. Deposition of high-k dielectrics is achievable by sputtering, MOCVD or ALD, among several other methods.

Several high-k dielectrics were available in our cleanroom, including aluminum oxide (Al_2O_3), ZnO , HfO_2 , tantalum oxide (Ta_2O_5) and TiO_2 . To choose the high-k dielectric to test in the flexoelectric actuators, two properties were important: good compromise between relative permittivity and electrical breakdown field and good thickness uniformity. Increasing the relative permittivity should increase the flexoelectric coefficient, but at the cost of a lower electrical breakdown field [243].

Depositing less than 50 nm thick dielectric films requires a good thickness uniformity, conformity and low surface roughness. Therefore, ALD was chosen over sputtering for the deposition technique. Three dielectrics were available for deposition by ALD: Al₂O₃, HfO₂ and TiO₂. Initial work was first completed with TiO₂ and HfO₂, since the flexoelectric coefficient of Al₂O₃ is most likely quite small due to its low relative permittivity.

On the one hand, while the breakdown field of TiO₂ is relatively low, its flexoelectric coefficient has already been measured in thick single crystal films [193] and it would be interesting to compare the flexoelectric coefficient of nanoscale, polycrystalline TiO₂ films to its thicker counterpart. On the other hand, HfO₂ has a good compromise between relative permittivity and electrical breakdown field and is under active development for CMOS applications [243].

In the end, TiO₂ could not be deposited with sufficient quality due to a large surface roughness and large particulates within the films. No such issues existed for the HfO₂ films, so the fabrication for the flexoelectric actuators continued with HfO₂.

3.2 Fabrication

3.2.1 Process Flow

Long-term, we envision trying several different high-k dielectrics and different layer thicknesses; we therefore developed a simple and flexible process flow with four steps, which is schematically shown in Figure 3.1. The process flow requires substrates with wet oxidized SiO₂ to act as an electrical insulating layer as well as sacrificial layer for release of the actuators. The processing at the wafer level includes three steps: Liftoff of the sputtered bottom electrode thin film (Figure 3.1 A), deposition and patterning of the dielectric and top electrode thin films (Figure 3.1 B) and liftoff of electrode pads to use in later electrical characterization (Figure 3.1 C).

As will be discussed later in this chapter, secondary phenomena such as electrostriction and electrostatic force may also generate deformation in the flexoelectric actuators by making the dielectric layer effectively piezoelectric. Therefore, two thickness cross sections were fabricated, one with zero shift of the neutral axis and one with a set displacement of the neutral axis due to the increase in thickness in one of the electrodes. By creating two thickness cross sections, the effective piezoelectric effect could be modulated, and it would be possible to remove the effect from the flexoelectric coefficient measurements.

The thicknesses of the electrode and HfO₂ films was set as low as possible to maximize the flexoelectric curvature. The thickness of the electrode thin film was chosen to vary in thickness from 25-35 nm, as these were thicknesses that could be reliably deposited with the available sputtering systems. The HfO₂ film thickness was chosen to be 50 nm to be confident that the dielectric films would not electrically breakdown during the later characterization. Recently, undoped HfO₂ thin films have been shown to have thickness-dependent ferroelectric

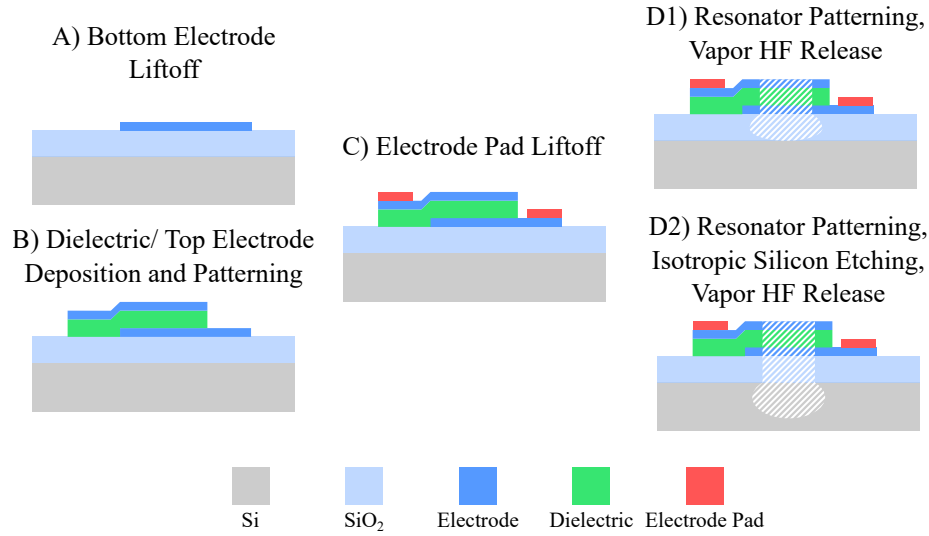


Figure 3.1 – Developed process flow for fabricating flexoelectric actuators based on four steps: (A) Liftoff of a sputtered bottom electrode thin film; (B) Deposition of a dielectric thin film by ALD and top electrode thin film by sputtering, then patterning of the two layers by dry and wet etching, respectively; (C) Liftoff of an additional metal thin film on the electrode pads for wire bonding; (D) Chip level fabrication to pattern and release the actuators by etching the sacrificial SiO₂ through vapor HF etching (D1) or through isotropic Si etching and vapor HF etching (D2). The checkered pattern denotes areas where the sacrificial SiO₂ and/or Si layers were etched to release the actuators.

properties [244]; we also chose a thicker HfO₂ film thickness to avoid ferroelectricity.

The fabrication then continues at the chip level to maximize the variety of actuators that can be designed and fabricated. The flexoelectric actuators are patterned by a standard photolithography and dry etching. Then, two release methods are possible for the flexoelectric actuators: etching of the sacrificial SiO₂ layer under the actuators via vapor hydrofluoric acid (HF) etching (Figure 3.1 D1), or dry etching of the sacrificial SiO₂ layer to access the Si substrate, then isotropic Si etching and vapor HF etching to fully release the actuators (Figure 3.1 D2). Both methods were tried during processing of the HfO₂ flexoelectric actuators; more discussion of why two different methods were used will be seen in Section 3.2.7.

Several different metals can be used for the electrode thin films, including Pt, Al, Ti and Mo. Of the four metals, Pt and Mo are the most chemically stable and resistant to most wet etchants and solvents. Since dry etching will be used, fencing is a potential issue, which occurs when nonvolatile elements cannot be fully removed during the etching process and redeposit on the sidewalls of the photoresist mask [245]. Fencing from dry etching is often difficult to remove and can alter the neutral axis position in the thickness cross section. Both Pt and Mo were tested as electrode layers during processing of the HfO₂ flexoelectric actuators; we will show later that etching of the Pt thin films generated significantly more fencing than the Mo thin

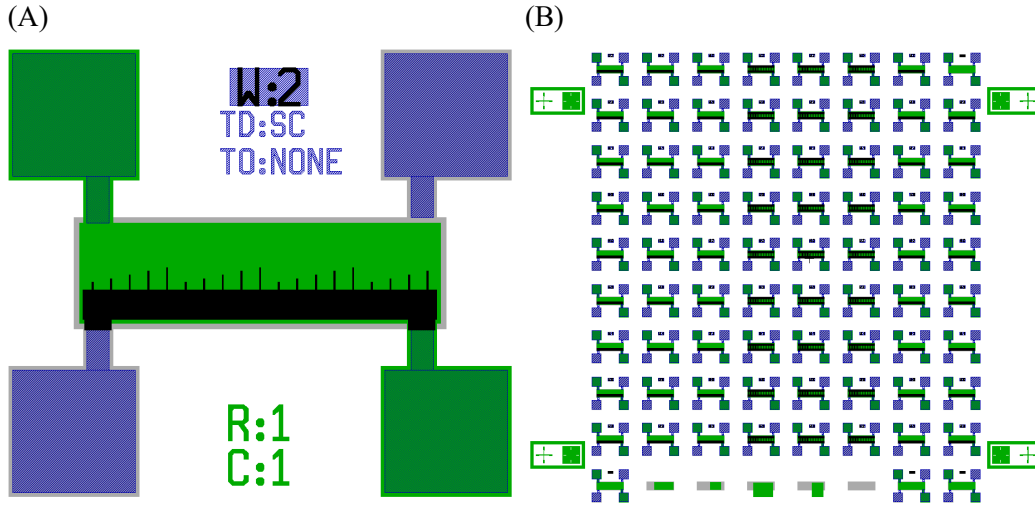


Figure 3.2 – Mask designs for cantilever electrodes and chips. (A) Example of an electrode with 19 cantilevers comprised of 5 lengths and 1 width. Each electrode is individually labeled. The grey areas denotes the bottom electrode, green the top electrode, checkered purple for the Al pads and black for the actuators and beam support to clamp the cantilevers and connect them to the electrode pads. (B) Chip design with 78 electrodes. The bottom row includes electrical test structures and a resolution array to determine the quality of the photolithography.

films, which precluded the use of Pt layers.

Some wet and dry etch tests were completed on Mo, TiO₂ and HfO₂ thin films to optimize their processing. We found that Cl₂ and SF₆-based dry etching was able to etch both the metal and dielectric thin films with a sufficient difference in their respective etch rates and that HF-based wet etching was able to selectively etch the HfO₂ and TiO₂ thin films without attacking the Mo electrodes. A table with the results of all the etch tests can be found in Appendix A.5.

3.2.2 Mask Design

The mask design was composed of two elements: the base design for the electrode that was replicated across the wafers; and the actuator design that was overlaid on top of the electrode design and could be modified for fabricating different actuator types, beam lengths and widths. The two elements are shown in Figure 3.2 A. The top electrodes (solid green color) overlapped the bottom electrodes (solid grey color) in the rectangular area to create the electrode/dielectric/electrode thin film stack. Two electrode pads (purple checkered squares) were designed for each electrode layer to be able to wire bond or contact with DC probes. The actuator design (solid black color) was located in the rectangular area and contained both the cantilevers as well as the beam support, which provided a fixed support for the cantilevers as well as electrically connecting them to the electrode pads.

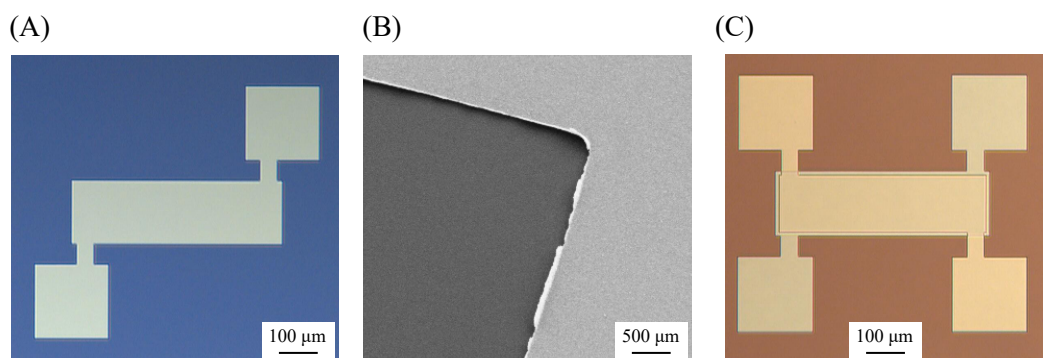


Figure 3.3 – Results of bottom electrode liftoff. (A) Optical microscope image of bottom electrodes after liftoff. (B) Tilted SEM image which shows small fences left over from the liftoff. (C) Optical microscope image of top electrode after wet etching of HfO_2 and photoresist stripping. Top electrodes are slightly redder in appearance and overlap the bottom electrodes at two points.

The cantilevers were designed to have five lengths (10, 15, 20, 25 and 30 μm) and 4-5 widths (2-6 μm). Each cantilever was separated from his neighbors by a distance of 25 μm to minimize mechanical crosstalk.

On each chip, 78 electrodes were available for fabricating either cantilevers or test structures (Figure 3.2 B). One row of electrodes was set aside for electrical test structures and two resolution arrays to measure the overexposure and overdevelop from the photolithography. The wafer level mask design can be seen in Appendix A.7.

3.2.3 Bottom Mo Electrode Liftoff

The wafers used in this work were 100 mm, 525 μm Si substrates and approximately 290 nm of thermally oxidized SiO_2 . The thermal oxide layer served both as electrical insulation between the electrodes and Si substrate and as a sacrificial layer for releasing the actuators at the end of the processing. Before the start of the fabrication, the radius of curvature of the wafers was measured for later residual stress calculations. More details on the fabrication can be found in Appendix A.6.

The bottom electrodes were patterned by double layer liftoff using a sacrificial resist layer plus a photosensitive resist (photoresist) layer. In comparison to pattern transfer by dry etching, liftoff minimizes the contact between the photoresist and the desired thin film and the potential creation of fences. While liftoff is traditionally completed with evaporation, in this project, sputtering was chosen for the Mo thin films. As will be discussed later (Section 3.2.6), evaporated Mo poorly adheres on thermally oxidized substrates and the electrical resistance of the thin films is higher. Sputtered Mo thin films adhere better on SiO_2 but some fencing will occur because sputtering is a more conformal deposition process than evaporation.

The photolithography for the bottom electrode was completed using an automatic photoresist coater and developer system (Süss ACS200 Gen3) and a direct laser writing system (Heidelberg Instruments MLA150). The sacrificial resist layer was etched by the developer solution when the photoresist layer was being developed, creating an undercut beneath the photoresist layer. This undercut later creates a separation during the metal deposition between the metal that is required to stay on the substrate after the liftoff and the metal adhering to the photoresist, which will be removed at the end of the liftoff. In our photolithography, the undercut was approximately 1 μm . The photosensitive resist layer was overexposed by approximately 0.75 μm , which was not an issue for the later fabrication steps.

After the photolithography, a bottom electrode of 25 nm Mo was sputtered onto the wafers at room temperature. To finish the liftoff, the photoresist and sacrificial resist were stripped by a solvent overnight, which also lifted away the Mo that had been deposited on the photoresist layer. The wafers were rinsed and dried before checking the liftoff results in the microscope.

An example of a fabricated bottom electrode structure can be seen in Figure 3.3 A. Small fences on the edges of the bottom electrodes were found through SEM analysis and are due to the sputtering process depositing a small amount of material in the undercut (Figure 3.3 B). However, these fences were small or infrequent enough not to be measured by mechanical profiling. Therefore, the chance of electrical shorting due to the fences was minimal, considering that a 50 nm HfO₂ film will be conformally deposited by ALD on top of the bottom electrode layer.

3.2.4 HfO₂ and Top Mo Electrode Deposition and Patterning

After the bottom electrode were fabricated, a HfO₂ thin film was deposited by ALD with a recipe for 50 nm thickness. The precursors for the ALD deposition were TEMA¹ and water (H₂O) and the deposition rate was set as 1 Å/cycle on Si substrates. Although dummy HfO₂ depositions on Si chips were tested with the same recipe and confirmed to have the correct 50 nm thickness, SEM and ellipsometer of the HfO₂ thin films on the Mo bottom electrodes revealed that the HfO₂ thickness was 40.5 ± 5.2 nm.

The top Mo electrode was deposited directly after the HfO₂ deposition to minimize post-deposition contamination or oxidation. Two different Mo film thicknesses, 25 and 35 nm, were deposited to create the symmetric and asymmetric thickness cross sections, respectively.

The radius of curvature was measured after the deposition of the HfO₂ and top Mo electrode thin films, respectively, to calculate the residual stress in each layer based on the technique described in Section 2.1.2. The residual stress for the HfO₂ thin film was 580 ± 51 MPa, while the residual stress for the 25 and 35 nm thick top Mo electrode films was 420 ± 57 MPa and 455 ± 16 MPa, respectively. The residual stress in the Mo bottom electrode thin film could not be measured because it was already patterned after the liftoff.

¹tetrakis(ethylmethylamido)hafnium(IV)

Patterning of the top electrode and HfO₂ layers in both wafers was achieved by a photolithography of the second mask design and dry/wet etching of the layers. The photolithography was completed in the same equipment as for the Mo bottom electrode liftoff, but with a single positive photoresist layer. More details on the photolithography can be found in Appendix A.6.

After the photolithography, the top Mo electrode layer was etched by SF₆-based plasma etching in an ICP plasma etcher. An overetch of a few nanometers into the HfO₂ was completed to ensure that the Mo layer had been fully etched across the wafer surface. The completed top Mo electrode layer etch was confirmed by manually checking with a multimeter that the electrical resistance was high in the etched areas as well as through ellipsometer measurements of the HfO₂ layer thickness.

The HfO₂ layer was then wet etched with a 10% HF chemistry. Although the HfO₂ layer could also have been dry etched, wet etching this layer avoided etching the Mo bottom electrode layer as well as to avoid fencing that could short the electrodes. The HfO₂ layer etch was checked by measuring the sacrificial SiO₂ layer thickness with a spectroscopic reflectometer. The sacrificial SiO₂ layer was also etched approximately 40 nm.

After confirming the HfO₂ and Mo layers have been fully etched in the optical microscope, the photoresist mask was removed by wet and drying etching (see the runcard in A.6 for more details). A microscope image of a fabricated bottom and top Mo electrode can be seen in Figure 3.3 C.

3.2.5 Electrode Pad Liftoff and Dicing

To fabricate the electrode pads for later wire bonding, the same photolithography process was completed as for the bottom electrode liftoff, with the exception of using a thicker sacrificial layer and photoresist layer to be able to liftoff a thicker metal film. A 500 nm thick Al film was then evaporated onto wafers and the same liftoff process as for the bottom electrode was used.

Before the chip level fabrication, the wafers were coated with 5 μm of photoresist to protect the electrodes and then diced to fabricate 1 by 1 cm chips. Afterwards, the photoresist from chips that would continue onto the last processing step was manually removed with a photoresist stripper (SVC14).

3.2.6 Fabrication Issues during Wafer Level Fabrication

A few issues were encountered during the fabrication of the top and bottom electrodes. One issue was that after the electrode pad liftoff on some wafers, residues were left on the top electrodes after stripping away the photoresist and sacrificial resist layers. The residues were purple to red in color under the optical microscope, as can be seen in Figure 3.4 A. Despite repeated treatments with different solvents, wet etchants and O₂ plasma, these residues could not be fully removed, forcing the abandonment of these wafers.

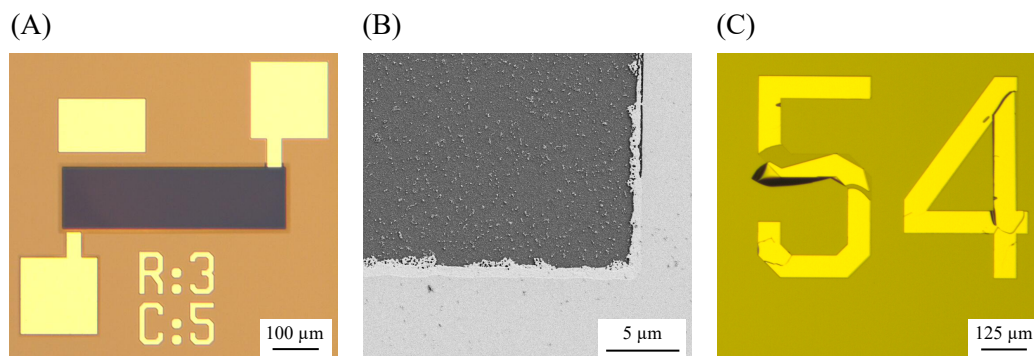


Figure 3.4 – Issues encountered during wafer level fabrication (A) Polymer residues left on top Mo electrodes after Al liftoff on some wafers. The LOR resist may have reacted with the top electrode during the evaporation of Al, producing residues that were impossible to remove, despite several attempts with various solvents, chemicals and O_2 plasma. (B) A fabrication trial with Cr/Pt electrodes instead of Mo electrodes proved not successful after significant fencing occurred along the edges of the Pt top electrodes from dry etching. Ultrasound, solvents and HF etchings proved unsuccessful at removing the fencing. (C) A fabrication trial with evaporated Mo electrodes instead of Mo sputtered electrodes was not successful due to the poor adhesion of the bottom Mo electrodes to the thermally oxidized substrates.

Sputtered Cr/Pt electrodes were also tested as an alternative to Mo electrodes. However, large fences were created during dry etching of the top Pt electrode, which can be seen in Figure 3.4 B, and the electrical resistance of the Cr/Pt bottom electrodes significantly increased over time.

Multiple HF etchings were done to try to remove the fencing and reduce the electrical resistance. The Cr/Pt bottom electrode electrical resistance did reduce, but the fences were not removed. Also, the electrical resistance between the top and bottom electrodes through the HfO_2 layer significantly decreased after the HF etchings, which could be due to the fences shifting and shorting the electrodes.

One explanation for these results is that Cr diffusion and/or oxidation of Pt or Cr caused the bottom electrodes to have a high electrical resistance. The high probability of unremovable fencing during the later fabrication of the flexoelectric actuators put a stop to the use of Cr/Pt electrodes.

A fabrication trial was also completed with evaporated Mo instead of sputtered Mo, since evaporation would lead to a better thickness uniformity and less fencing during the bottom electrode liftoff. However, these electrodes proved unsuccessful, based on their poor adhesion to the oxidized substrate, as can be seen in Figure 3.4 C, and high electrical resistance in both the top and bottom Mo electrodes that increased with time. The increase in electrical resistance may have been due to oxidation of the Mo thin films.

3.2.7 Patterning and Release of Flexoelectric Actuators

Three different chip level process flows (Runs 1, 2 and 3) were created to fabricate several chips. In general, the chip level process flow followed the following procedure:

- Protective SiO₂ sputtering and attachment to carrier wafers
- Photolithography
- Etching of protective SiO₂ layer and removal of generated fences
- Etching of Mo and HfO₂ layers and removal of generated fences
- Dry etching of sacrificial SiO₂ layer and isotropic Si etching (not Run 1)
- Photoresist stripping and removal from carriers
- Vapor HF etching to finish release of actuators

An overview of the differences in fabrication for each run can be seen in Table 3.1. The most important difference in the three fabrication runs was in the actuator release (Run 1 versus Runs 2 and 3). In Run 1, the release was completed by etching the sacrificial SiO₂ layer with vapor HF. In Runs 2 and 3, the sacrificial SiO₂ layer was initially anisotropically etched by a fluorine-based ICP etcher down to the Si substrate. Then, the open areas of Si substrate were isotropically etched by SF₆ with another ICP plasma etcher until the flexoelectric actuators were released. Finally, vapor HF was used to remove the sacrificial SiO₂ beneath the actuators and any protective SiO₂ remaining on top of the electrodes. With the first method, the approximately 300 nm distance between the actuators and substrate made beam collapse much more likely, which was why Runs 2 and 3 included the silicon substrate etching. The collapse can be due to stiction or static deformation of the beams due to residual stress within the thin films. While every effort was made to avoid stiction, which occurs when the evaporation of water or solvents creates capillary forces between the beams and substrate, during the vapor HF processing step, some water may be generated if the recipe does not sufficiently flush the reactants created during the etching.

Another difference between Run 1 and Runs 2 and 3 is in the deposition of the photoresist. In Run 1, the photoresist deposition was completed manually to better control the edge beading on chips attached to carrier wafers. To decrease the fabrication time in Runs 2 and 3, automatic photoresist coating was used. Depending on the photoresist thickness, the photoresist deposition recipes were optimized to minimize photoresist beading on the edges of the chips and to generate as uniform a photoresist thickness as possible. In Run 2, 2 µm of photoresist could be deposited on the chips without significant beading and consistent thickness due to the high spin speeds required for that thickness and specific photoresist dilution. However, when the photoresist availability in machines was altered, a more diluted photoresist had to be used in Run 3 which did not require high spin speeds to achieve the desired 1.2 µm thickness. Therefore, a special recipe with an acceleration at the end of the spin cycle was created to help remove the edge beading. However, the photoresist was still not as uniform in thickness across the chips compared to Runs 1 and 2.

Chapter 3. Flexoelectric Actuators Based on Amorphous HfO₂

Table 3.1 – Breakdown of differences in fabrication between Runs 1,2 and 3. The Rite Track is another automatic photoresist coating and developing system available at CMi. The gases used during SPTS etching were C₄F₈/He/H₂.

Chip Level Fabrication Step	Run 1 (Chip 1s, 1a)	Run 2 (Chips 2s, 2a)	Run 3 (Chip 3a)
25 nm SiO ₂ Sputtering	Yes	Yes	Yes
HDMS Pretreatment	Yes	Yes	Yes
Photoresist Deposition	Manual	Rite Track	ACS200
Photoresist Thickness	2 µm	2 µm	1.2 µm
Exposure Tool	MLA	MLA	MLA
Photoresist Development	Manual	Automatic +Manual	Manual
Post-Development Bake	No	Yes	Yes
Photoresist Descum	Yes	No	Yes
SPTS Protective SiO ₂ Etch Time	7.5 s	15 s	12.5 s
BHF Fence Removal	Yes	Yes	Yes
Post-Etch Bake	No	No	Yes
Mo and HfO ₂ STS Etching (Cl ₂ /Ar)	All Layers	Top Mo/HfO ₂ , then BHF, then bottom Mo	All layers
BHF Fence Removal	Yes	No	No
SPTS Sacrificial SiO ₂ Etching	No	Yes	Yes
O ₂ Plasma Polymer Removal	No	No	Yes
AMS Isotropic Si Etching	No	Yes	Yes
Photoresist Stripping	O ₂ Plasma +Remover 1165 +O ₂ Plasma	O ₂ Plasma +Remover 1165 +O ₂ Plasma	Manual Edge Clean +O ₂ Plasma
BHF Fence Removal	Yes	No	No
uETCH vapor HF	Yes	Yes	Yes

The designed widths on Chips 1s, 2s and 2a for both the cantilevers and doubly clamped beams were 2, 3, 4, 5 and 6 µm, while on Chip 3a, only widths between 2-5 µm were fabricated. The designed and measured cantilever lengths for four of the chips used to characterize the HfO₂ effective flexoelectric coefficient can be found in Appendix A.11.

3.2.8 Fencing During Chip Level Fabrication

Fencing was an issue during the wafer and chip level fabrication. Fencing can shift the neutral axis position within the cantilevers, which made it essential to remove before the cantilever release. To determine the fencing sources, a series of chips were fabricated until after the SPTS protective SiO₂ etching (Figure 3.5 A), after the top Mo electrode etching (Figure 3.5 B) and after the HfO₂ etching (Figure 3.5 C) and then analyzed with the SEM. To ensure that any imaged fencing was only created from the dry etching of each new layer, previously made fences were removed by BHF, which was found to be successful at removing any fencing during the dry etching processing.

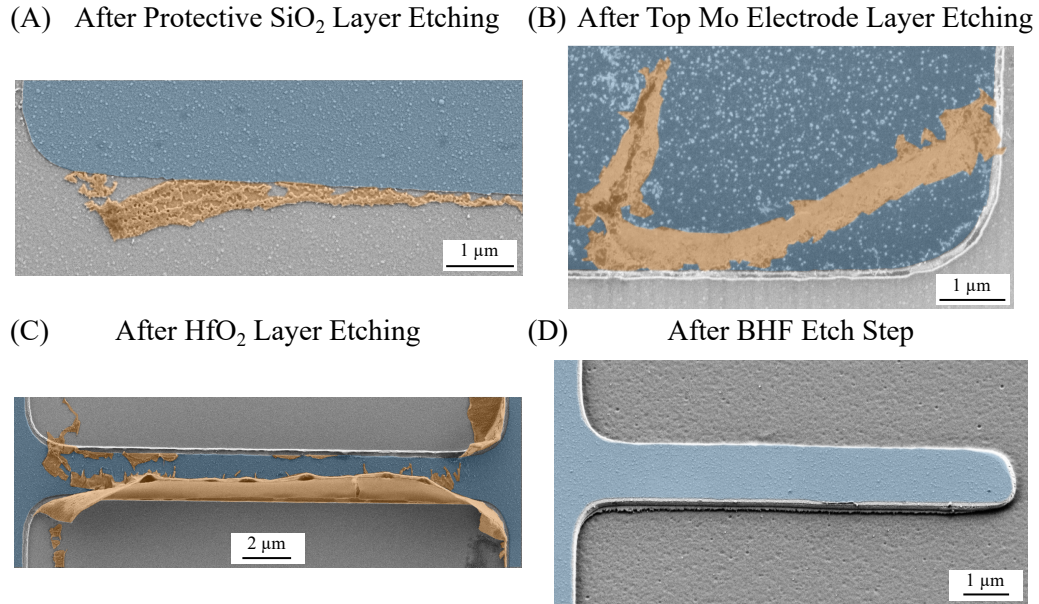


Figure 3.5 – Tests to determine the sources of fencing during dry etching (A) Top view SEM image of fencing due to the protective SiO₂ layer after SPTS etching (B) Top view SEM image of Mo fencing after STS etching of the top Mo layer. (C) Top view SEM image of HfO₂ fencing after etching through the HfO₂ layer in the STS. Note the large gap between the top and bottom electrode width due to the significant HfO₂ fencing. (D) Tilted SEM image of an unreleased cantilever on Chip 1s, after a buffered hydrofluoric acid (BHF) etch to remove the fencing. Very few fencing residues are left on the cantilever edges.

Through the SEM analysis, HfO₂ was found to create the largest fencing. Based on these results, a BHF etching was completed during Run 1 after etching the top and bottom Mo electrodes and HfO₂ layer, which successfully removed most of the fencing (Figure 3.5 D).

The impact of fencing on shadowing the etching of lower layers can be seen most visibly in Figure 3.5 C. Where the fencing has fallen away from the electrode edges, a gap can be seen between the top electrode and the bottom electrode. Without removal or minimization of fencing, this gap would be patterned into the bottom electrode. Minimizing this mismatch of top and bottom electrode thicknesses is important to maintaining the designed asymmetry or symmetry in the thickness cross section of the later released flexoelectric actuators.

3.3 Fabrication Results

3.3.1 Run 1

In Run 1, Chips 1s and 1a were fabricated, which have symmetric and asymmetric thickness cross sections, respectively. In Figure 3.6A, a cross section SEM image of a released cantilever

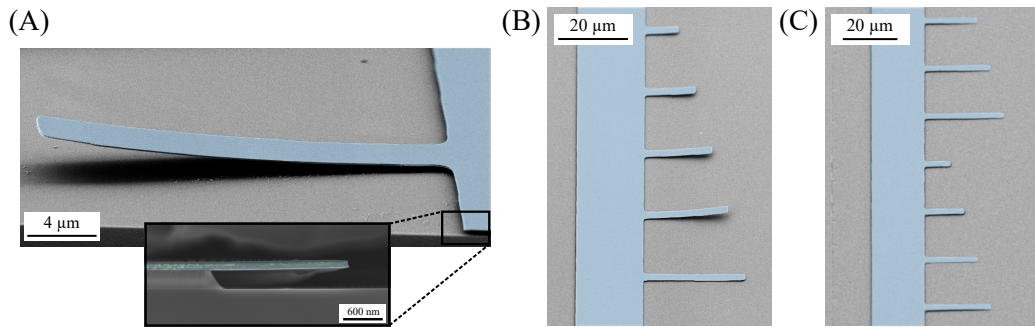


Figure 3.6 – Successful fabrication in Run 1 of Chip 1s (symmetric cross section) but poor results for Chip 1a (asymmetric cross section). (A) Cross section SEM image of a released cantilever on Chip 1s with static curvature due to residual stress from depositions and fabrication. Inset is cross section SEM image of SiO₂ underetch underneath the beam support. The Mo (blue color) and HfO₂ (green color) layers can be distinguished from each other in the thin film stack. (B) Example of released cantilever array from Chip 1s in tilted SEM image, with the longest cantilevers not surviving the release process. The properly released cantilevers can be visually separated from collapsed cantilevers by the dark shadow underneath them. (C) Unsuccessfully released cantilever array seen on Chip 1a; most cantilevers were found in this condition.

from Chip 1s can be seen. Most cantilever edges were free of residues and demonstrated a static deformation due to the residual stress from the fabrication and layer depositions. The underetch of the sacrificial SiO₂ layer during the vapor HF process can be seen in the inset of Figure 3.6 A, which reaches to approximately 2 μm. While most of the cantilevers survived the release process on Chip 1s (Figure 3.6 A and B), the vast majority of cantilevers on Chip 1a did not (Figure 3.6 C). Collapsed cantilevers can be distinguished from free-standing ones by the lack of dark shadowing beneath them. The small distance between the cantilevers and the substrate, as well as a slightly downward static curvature due to the residual stress within the HfO₂ and Mo layers, may be the reasons for the low survival rate in Chip 1a.

3.3.2 Run 2

Based on the results of Run 1, the process flow for Run 2 was modified to fabricate a larger distance between the cantilevers and substrate by silicon isotropic etching before the vapor HF etching. Chips 2s and 2a were fabricated with this modified process flow, of which the results can be seen in Figure 3.7. Much higher cantilever survival rates were found for Chip 2a in comparison to Chip 1a from Run 1 (same asymmetric cross section), while similar cantilever survival rates were found in both Chips 1s and 2s (both chips have a symmetric cross section). However, a polymer layer developed across all open areas during anisotropic etching of the sacrificial SiO₂ layer by etching gas C₄F₈, which is known to create a passivation layer on open silicon surfaces in Bosch processing. The polymer layer is transparent and therefore not discovered until after SF₆-based isotropic etching of the Si substrate. The leftovers of the polymer layer can be seen surrounding the cantilevers and beam support in Figure 3.7 A.

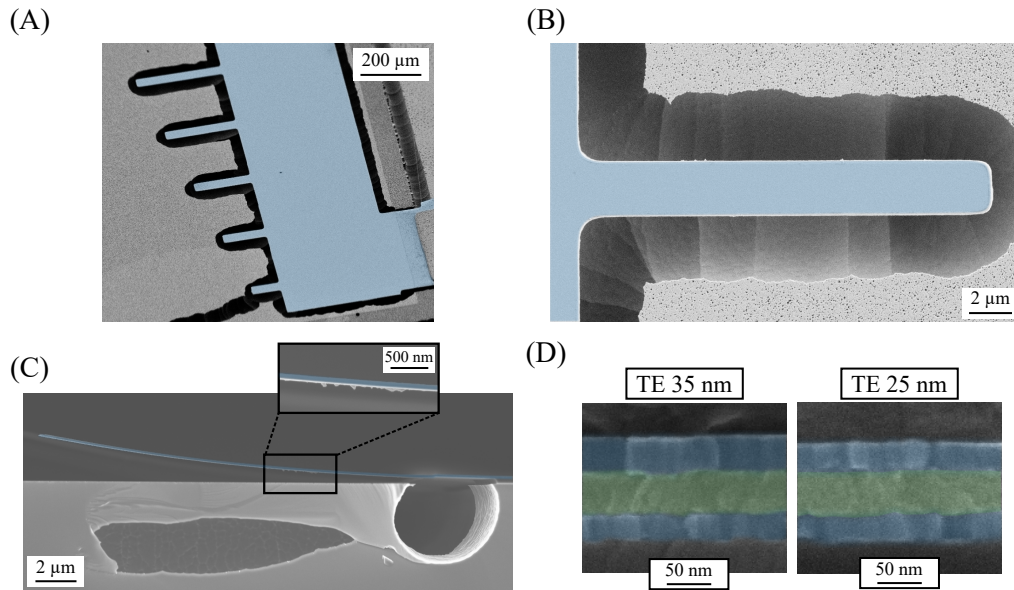


Figure 3.7 – SEM images of Chips 2a and 2s from Run 2 and of the thickness cross sections for the asymmetric (TE 25 nm) and symmetric (TE 35 nm) cross sections. (A) Tilted SEM image of released cantilevers from Chip 2a. While the release was good near the cantilevers and beam support, the polymer layer left during the sacrificial SiO_2 etching masked most of the open areas during the isotropic Si etching. (B) Top view SEM image of a released cantilever from Chip 2a, where near the cantilever, locally stronger plasma etching removed the polymer layer and allowed isotropic Si etching. (C) Cross section SEM image of a released cantilever from Chip 2s and partial release of beam support due to Si underetching. The polymer masking during the isotropic Si etching created pockets underneath the cantilevers and beam support. Insert shows some residues potentially due to an incomplete Si or SiO_2 etching. (D) Cross section SEM images to determine the thickness of Mo and HfO_2 layers in both thickness cross sections.

Table 3.2 – Thickness of each layer in the symmetric and asymmetric thickness cross sections based on cross section SEM images. An example of these images can be found in Figure 3.7 D. The Mo bottom electrode and HfO_2 layer measurements were averaged across both wafers.

Thin Film	Designed Thickness (nm)	Measured Thickness (nm)
Mo bottom (symmetric & asymmetric)	25	25±3
HfO_2	50	40±5
Top Mo electrode (symmetric)	25	27±3
Top Mo electrode (asymmetric)	35	36±3

During the Si etching, the polymer layer had served as an etch mask and was only removed near the cantilevers and beam support due to locally stronger plasma etching conditions, an example of which can be seen in Figure 3.7 B. Near and underneath the cantilevers, the local Si isotropic etching was successful, as seen in a cross section SEM image of a released cantilever in Figure 3.7 C.

While the fabrication was successful in creating more distance between the released cantilevers and substrate, small residues were left on the sides and underneath the cantilever (Figure 3.7 B and inset of Figure 3.7 C). Since few cantilevers could be imaged by cross section SEM, it is difficult to know the percentage of residues remaining on the cantilevers or if they significantly impact the later flexoelectric characterization of the cantilevers.

During Run 2, an additional BHF etching was completed after dry etching the top Mo and HfO₂ layers to remove any fencing from shadowing the bottom electrode dry etching, based on previous etch tests during Run 1 that demonstrated HfO₂ was the dominant fence source (Section 3.2.7). While the fences were successfully removed, no significant change in the top and bottom electrode gap was seen during the SEM analysis.

The thickness of each deposited layer was found by cleaving chips with asymmetric and symmetric cross sections and imaging with cross section SEM. The average thicknesses of each layer, seen in Table 3.2, were calculated based on analysis of the SEM images, such as in Figure 3.7 D, in ImageJ. The top and bottom electrodes thicknesses were close to the desired deposited values, while the HfO₂ layer was approximately 10 nm thinner than the desired 50 nm thickness as set during the ALD deposition.

3.3.3 Run 3

In Run 3, four chips were fabricated. To remove the polymer residues found during Run 2, an additional O₂ plasma etch step was introduced between the sacrificial SiO₂ etching and isotropic Si etching. This successfully removed the polymer layer and allowed a clean isotropic Si etching. However, the photoresist burned during the O₂ plasma etching, which made removing the photoresist extremely difficult after the cantilevers were released. By careful hand removal of most heavily burned areas and further O₂ plasma etchings, it was possible to remove the whole photoresist layer and complete the final vapor HF etching. One additional change from Run 2 was extending the isotropic Si and vapor HF etchings to ensure no residues would be left underneath the cantilevers.

Released cantilevers from Chip 3a can be seen in Figure 3.8. Additional SEM images from Chip 3a of a full cantilever electrode structure can be found in Appendix A.8, as well as a top view of released cantilevers. No large residues from the polymer masking are visible and the silicon etching seems uniform across the open areas (Figure 3.8 A and inset). However, in some parts of the chips, the cantilevers and electrodes had small residues attached to their edges, which came from the non-uniform photoresist coating (Figure 3.8 B).

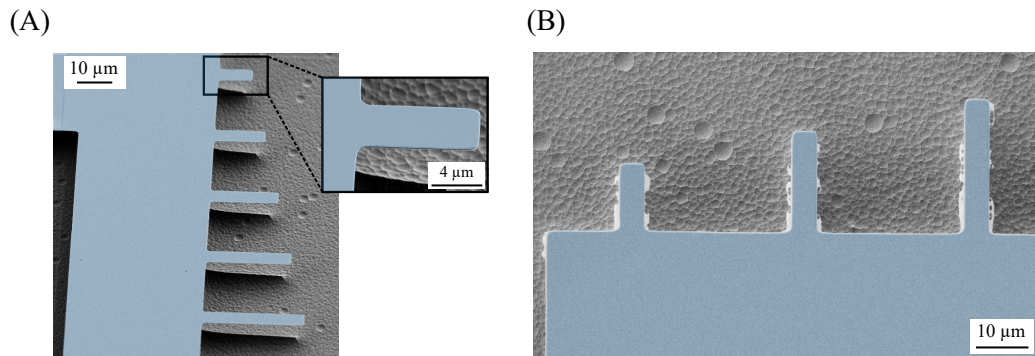


Figure 3.8 – SEM images of Chip 3a from Run 3. (A) Tilted SEM image of released cantilevers without large polymer residues around the cantilevers and support. Inset is close up tilted SEM image of a released cantilever with clean edges. The underetched silicon substrate can be seen underneath the cantilever. (B) Top view SEM image showing small residues found around some of the cantilevers after processing. These are most likely due to the sub-optimal photoresist deposition on parts of the chips, which made proper exposure and development difficult to achieve in a clean fashion.

During the photolithography, the machine for depositing photoresist and the photoresist had to be modified due to changes in equipment of the cleanroom. Despite modifications of the photoresist deposition recipe to reduce edge beading and generate a consistent thickness, the end results were not ideal. Some areas of the chips had a large deviations in photoresist thickness which limited the exposure and development success and generated residues on the cantilevers and beam supports. Efforts to remove the residues with low power O_2 plasma were not successful and so they carried on to partially mask later etching steps. Despite the residues, approximately half the actuators on the chips had clean edges.

3.4 Electrical Characterization

3.4.1 DC Measurements

The electrical resistance of the electrodes and through the HfO_2 layer were characterized by DC current-voltage (IV) sweeps through a semiconductor parameter analyzer (Hewlett-Packard 4155B) before and after the chip level fabrication process to check for any issues. Currents down to 1 fA can be accurately measured by the analyzer. All measurements were performed by a MATLAB program that interfaced with the semiconductor parameter analyzer to run and analyze the IV sweeps.

An example of an IV sweep from the top electrode to the bottom electrode through the HfO_2 layer on Chip 3s can be seen in Figure 3.9. The curves are nonlinear as well as asymmetric and occur in vacuum and air. Increasing the measurement speed does not change the IV curve behavior, but introduces more noise into the measurement, making it difficult to draw

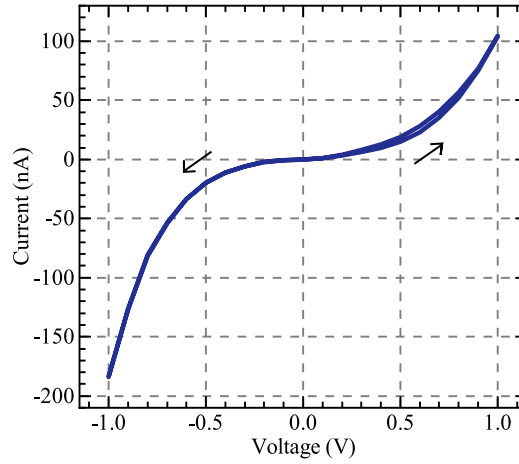


Figure 3.9 – Example of an IV sweep with a 1 V range to measure the electrical resistance from the top to bottom electrode through the HfO₂ layer, demonstrating an electrical resistance on the 10-100 MΩ. The electrical contact to the electrodes is through wire bonds to a PCB. The sample was in vacuum during measurements.

any conclusions on the speed of the measurement. Repeating the IV sweeps, increasing the voltage range or inverting the direction of the IV sweep produced no significant difference in the IV curve behavior or the magnitude of electrical resistance (see Appendix A.8).

One possible reason for this asymmetric nonlinear behavior is asymmetric diode interfaces between the HfO₂ and Mo layers. As the fabrication of each interface occurs at different points of the wafer level fabrication, it is possible that the interfaces are slightly different in roughness and/or oxidation conditions. However, the origin of the diode behavior is not entirely clear, since HfO₂ is a wide gap insulator and therefore Schottky contacts seem unlikely. The thickness of the HfO₂ layer is also too large for resistive switching or quantum tunneling to occur, such as in metal-insulator-metal (MIM) diodes. More measurements at different temperatures will be necessary to determine the diode behavior.

Although the IV curves are nonlinear, within a small voltage range similar to what will be applied in the deformation measurements, linear fits could be used to determine the electrical resistance with a sufficiently high accuracy (>0.95 adjusted R^2). The average electrical resistance from the top electrode to the bottom electrode through the HfO₂ layer measured before and after the chip level fabrication can be found in Table 3.3 for four of the chips later characterized for the HfO₂ effective flexoelectric coefficient.

Chips 1s, 2s and 2a maintained a higher resistance after the chip level fabrication, while the resistance in Chip 3a decreased by three orders of magnitude. The resistance on each chip was found to fluctuate by approximately one order in magnitude across the measured electrodes, which led to the high standard deviation. The fluctuations can be due to different conditions on the edges of each electrodes, such as residues or small fencing.

Table 3.3 – Electrical resistance and standard deviation from top to bottom electrode through the HfO₂ layer before and after vapor HF release (Chip 1s) or before and after chip level fabrication (Chips 2s, 2a and 2a). Measurements were taken with DC probes in air.

Chip	Before (E11 Ω)	STD (G Ω)	After (G Ω)	STD (G Ω)
1s	1,279	340	249	156
2s	214	68	1,034	643
2a	591	437	970	784
3a	3,712	3,036	1.1	0.7

The breakdown voltage of the HfO₂ layer varied between 6 V to above 40 V and depended on the cleanliness of the electrode edges. If the electrodes had clean edges after the chip level Mo and HfO₂ etching, the breakdown voltages were generally above 15 V.

The electrical resistance of only the top electrode and only the bottom electrode for Chips 1s, 2s, 2a and 3a can be found in Appendix A.9. The electrical resistances of both electrodes was below 100 Ω for all the measured chips and did not significantly change after the release of the cantilevers.

3.4.2 Capacitance and Polarization Measurements

To gauge the dielectric properties of the fabricated Mo/HfO₂ capacitors, the capacitance and polarization versus electric field were measured by an Aixacct TF2000 Analyzer.

For the capacitance and tangent loss measurements, a testing frequency of 1 kHz and voltage range between 2-5 V were chosen. The measured tangent losses and capacitance in two chips (0a and 3a2) can be seen in Figure 3.10 A and B, respectively. Chip 0a was fabricated before Run 1 in Section 3.3, while Chip 3a2 was fabricated during Run 3 (Section 3.3.3). While the capacitance does not significantly change between the two chips, Chip 3a2 provides a more stable capacitance over a larger voltage range. This may be due a better chip level fabrication in comparison to Chip 0a. However, the capacitance behavior is more asymmetric in Chip 3a2.

Low and similar tangent losses were measured in both chips and a more asymmetric behavior can again be seen in Chip 3a2, which may be due to differences in the contact interface between HfO₂ and top/bottom electrodes. The noise in the measurement of the capacitance and tangent losses is much lower in Chip 3a2 than Chip 0a, which could be due to either better fabrication or better contact of the probes with the electrodes during the measurement.

Based on the capacitance measurements, the thickness of HfO₂ and the area of the tested electrodes, a dielectric constant of 15 was found for the HfO₂ thin films. This value is slightly lower than the state of the art (20-25 [243]), but may be due to the non-ideal deposition on Mo or that the HfO₂ layer is amorphous, as will be discussed in the next section.

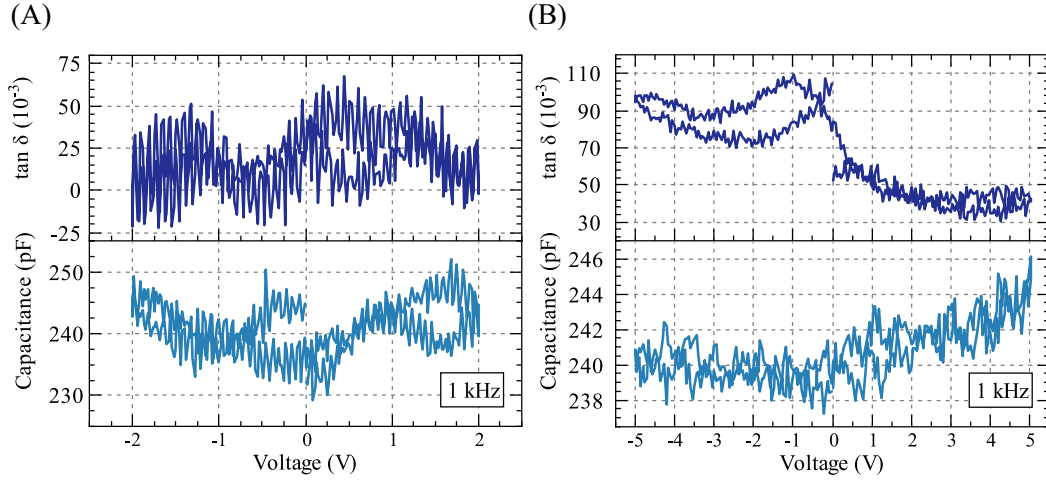


Figure 3.10 – Tangent losses and capacitance versus voltage on Chip 0a (A) and Chip 3a2 (B). Chip 0a was fabricated before Run 1, while Chip 3a2 was fabricated during Run 3. Despite the differences in quality of fabrication, the capacitance values are very similar between the two chips. In Chip 3a2, even across a voltage range of -5 to 5 V, the capacitance shifts only by a few pFarads. The tangent losses in both chips are also similar, although Chip 3a2 has a more pronounced asymmetric behavior. The noise in both the capacitance and tangent losses is less in Chip 3a2 compared to Chip 0a. Overall, the tangent losses are quite low, indicating that the Mo and HfO₂ capacitor is not very lossy.

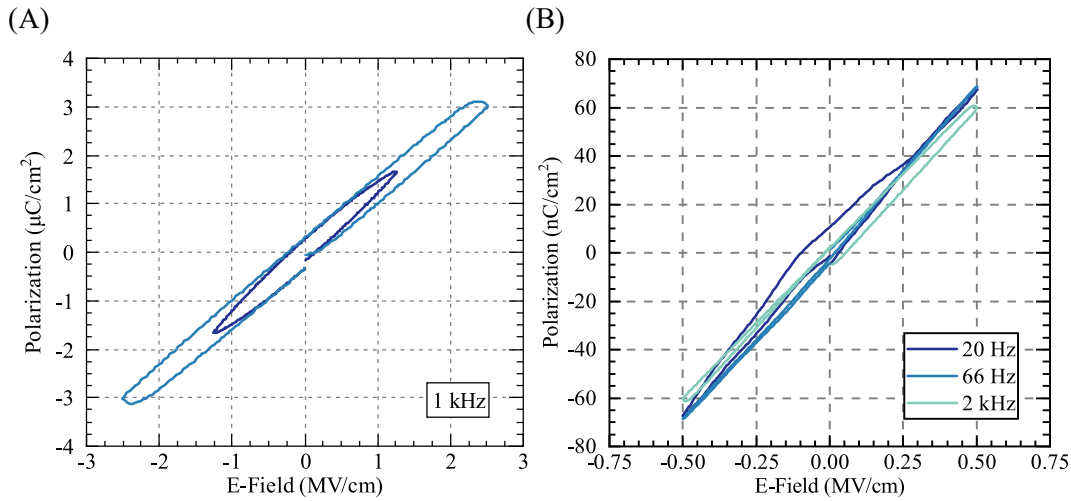


Figure 3.11 – Polarization versus electric field measurements on Chip 3a2. (A) Linear polarization and similar behavior with two different electric field ranges, 1.25 MV/cm and 2.5 MV/cm, confirming the non-ferroelectric properties of the HfO₂ thin film. The opening of the curves and the slight separation at 0 MV/cm suggests some dielectric losses and leakage current, confirming the CV and DC measurements. (B) Polarization versus electric field at three frequencies, showing no significant influence of frequency on polarization behavior up to 2 kHz.

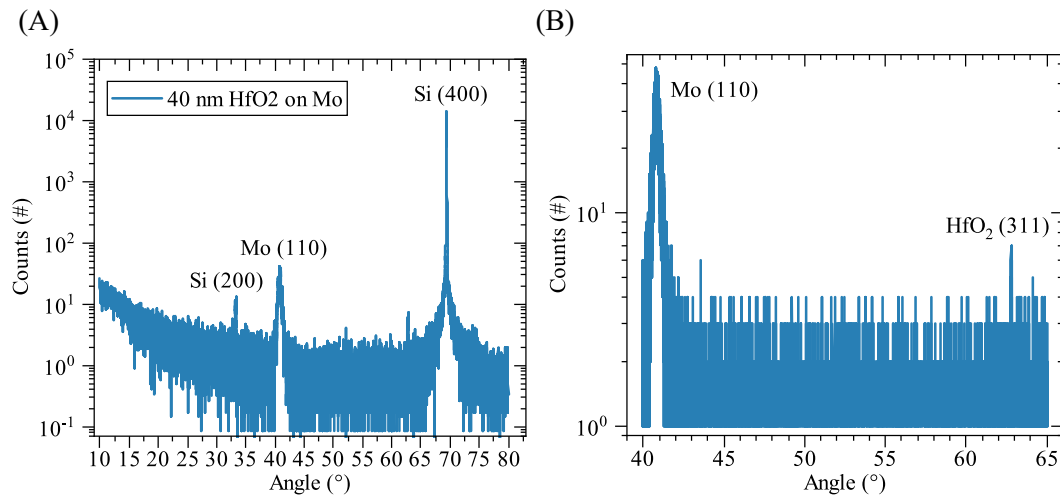


Figure 3.12 – Measured XRD curves for HfO₂ deposited on a Mo thin film. (A) Wide range normal incidence XRD scan showing peaks from the Si substrate and Mo thin film, but no clear peaks from HfO₂. (B) Shorter range, higher resolution XRD scan showing a potential HfO₂ peak from the (311) crystal orientation in monoclinic HfO₂.

The polarization properties of the HfO₂/Mo capacitor were tested with a voltage range between 2-10 V, which generated electric fields up to 2.5 MV/cm within the HfO₂/Mo capacitor. As can be seen in Figure 3.11 A and B, the polarization is linearly dependent on the electric field and mostly independent of the applied field frequency, which indicates that the HfO₂ thin films are non-ferroelectric. Some dielectric losses are visible by the opening of the curves, as well as leakage current through the slight separation at zero electric field. Some leakage and dielectric losses are not unexpected, based on the DC measurements and the capacitance/tangent loss measurements. With different interfaces between the HfO₂ and the top/bottom Mo electrodes, different electrical contacts are expected, which will lead to different leakage currents and slightly asymmetric polarization behavior [246].

It should be noted that the electrodes tested to measure the capacitance, tangent loss and polarization were not ideally designed for the measurement setup, namely, that they were much smaller than would be normally used. Since no microscope was available to contact the measurement probes onto the electrode pads, it was very difficult to correctly place the probes.

3.5 Crystallographic Characterization

To determine the crystallographic properties of the deposited HfO₂ layers, theta2theta XRD curves were taken of HfO₂ deposited on Mo, Si and Pt. An explanation of how these curves were created can be found in Chapter 2. The results of the scans on Mo can be seen in Figure 3.12. While no obvious HfO₂ peaks were measured in a wide theta2theta scan from

10-80° (Figure 3.12 A), a small peak was found when completing a higher resolution scan from 40 to 65° (Figure 3.12 B). Based on powder diffraction scans found in the literature, the diffraction peak at approximately 63° may be from the (311) crystal orientation in monoclinic HfO₂. Since this is the only peak potentially from the HfO₂ layer and it has a very low intensity, the HfO₂ layers used in this thesis work are considered to be amorphous. The broad shoulder at lower scan angles in Figure 3.12 A similarly confirms the presence of an amorphous layer. A higher resolution scan in this range also proved to confirm no HfO₂ diffraction peaks, as can be seen in Appendix A.10. Similarly, on bare Si substrates or Pt-coated Si substrates, no diffraction peaks from HfO₂ were measured. The XRD characterization on Si and Pt can be found in Appendix A.10. To fully confirm the crystallographic properties of HfO₂, transmission electron microscopy and grazing incidence XRD should be completed.

3.6 Flexoelectric Coefficient Characterization

3.6.1 Experimental Setup

The effective flexoelectric coefficient of the amorphous HfO₂ thin films were characterized by optically measuring the deformation generated by an applied electric field, similar to the work completed by Bhaskar et al. [16]. The experimental setup for these measurements can be seen in Figure 3.13. Each chip was attached to a in-house designed printed circuit board (PCB) by a double-sided carbon tape and then grounded by applying silver paste below the chips and annealing at 60°C for one hour. The PCBs were then installed in a vacuum chamber that could be pumped to below 10⁻³ mbar, at which point air damping losses on the actuators will be minimal. The vacuum chamber was installed on an optical table to minimize external vibrations.

An LDV (Polytec OFV-5000) with a maximum measurement frequency of 24 MHz was used in the displacement or velocity mode to measure the deformation of the actuators. In the displacement mode, the maximum deformation that could be measured before saturating the system was 50 nm; to avoid reaching this maximum during measurements, the maximum AC drive was calibrated for each actuator.

The LDV was interfaced with a lock-in amplifier (Zurich Instruments UHFLi), which has a maximum applicable voltage of 1.5 V (DC+AC) and can run frequency sweeps and thermal mechanical noise (TMN) measurements as well as interpret the returning data from the LDV. To measure the deformation of the cantilevers, frequency sweeps were performed that scanned a frequency range around the first flexural mode resonance while driving the cantilevers. The output from these measurements was the amplitude of the flexural mode in volts. The deformation of the cantilevers was translated from volts to meters by measuring the TMN of the cantilevers at the same first flexural mode resonance when not being driven and comparing to the theoretically known TMN, which will be explained in the following section.

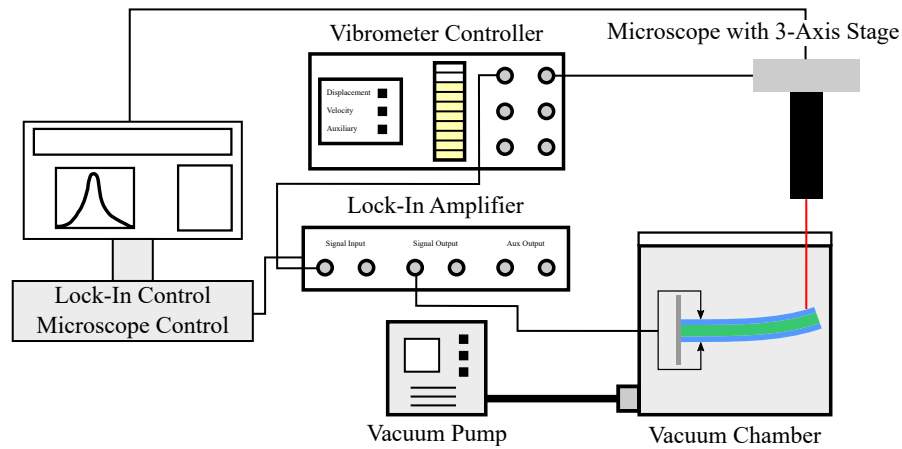


Figure 3.13 – Experimental setup for measuring the deformation of the flexoelectric actuators. Chips with electrodes of released actuators were wire bonded onto a PCB and fixed into a vacuum chamber pumped to below 10^{-3} mbar. A microscope with a three-axis stage was used to move and focus the laser onto the cantilevers. The LDV measured the movement of the actuators, while the lock-in amplifier was used to actuate the cantilevers and process the data from the LDV. A MATLAB program was written to run, collect and analyze all the experimental data.

3.6.2 Method to Measure the Flexoelectric Actuators

The experiments on each cantilever were completed as follows:

- Align laser onto the cantilever and optimize the output signal coming from LDV.
- Determine the fundamental resonance frequency, frequency range and AC drive range for the experiment through test TMN and frequency sweep measurements.
- Complete experiment to measure deformation of cantilever versus five AC drive and five DC bias conditions.
- Fit all frequency sweep and TMN measurements with a Lorentzian function to extract the center frequency, quality factor and peak amplitude.
- Calculate the specific responsivity for each set of five applied AC drives from the TMN measurements and calculate the deformation for all AC drive conditions.
- Compile all results for each cantilever into graphs and data sets.
- Calculate the effective flexoelectric coefficient and effective piezoelectric coefficients.

At a given AC and DC condition, five frequency sweep measurements with 150 points were taken. Most of the experiment time was spent on frequency sweep measurements, so a compromise was made between speed and resolution to keep each experiment within 10-20 minutes.

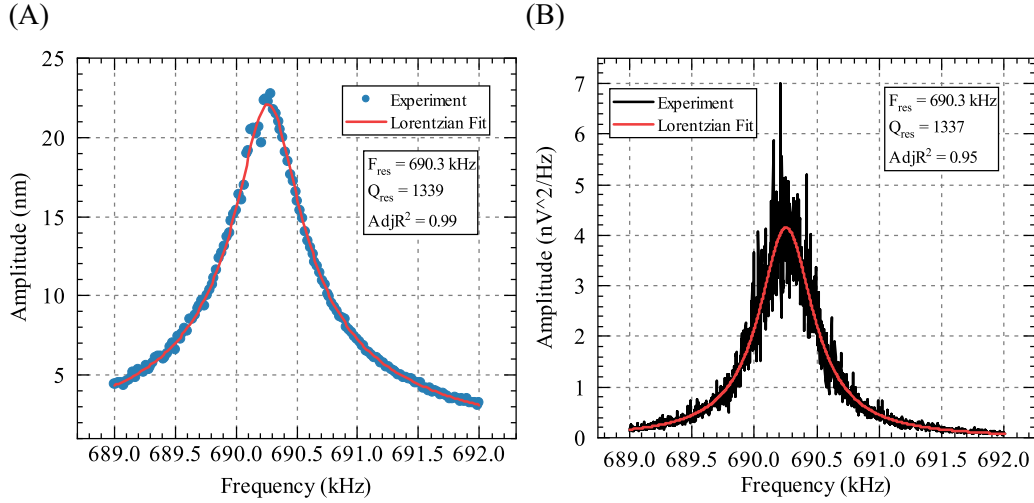


Figure 3.14 – Example of a frequency sweep (A) and a TMN measurement (B) with Lorentzian fits at the first flexural mode resonance on a 10 μm long, 4 μm wide cantilever in Chip 2s. The resonance frequency, quality factor and adjusted R^2 from the Lorentzian fitting can be seen for each measurement.

A Lorentzian fit, the equation of which can be found in Appendix A.1, was used to extract the center frequency, quality factor, peak amplitude and error from each frequency sweep measurement. An example of the Lorentzian fitting on a frequency sweep can be seen in Figure 3.14 A from a 10 μm long cantilever on Chip 2s. After fitting each frequency sweep measurement at a given AC drive and DC bias condition, the results were averaged and the standard deviation of the average as well as from the Lorentzian fitting for each measurement was propagated up.

TMN measurements that were averaged 50 times were taken at the beginning of each experiment, after every five AC conditions, and at the end of each experiment. A measurement of the necessary number of TMN measurements per experiment found that more frequent measurements than six times per experiment was unnecessary. The same Lorentzian fit as for the frequency sweeps was used to fit each TMN measurement to output the maximum amplitude, center frequency and quality factor. An TMN measurement and Lorentzian fit for a cantilever on Chip 2s can be seen in Figure 3.14 B.

Since precise alignment of the LDV laser onto the tip of each cantilever was difficult and the cantilever or laser could move slightly during the 10-20 minute experiments, it was necessary to be able to calculate the responsivity of the measurements during each experiment instead of relying on the 50 nm/V responsivity provided by the LDV equipment. The responsivity was used to translate the signal measured by the LDV in volts into a deformation in meters by calibrating the spectral noise density of the first flexural mode resonance TMN.

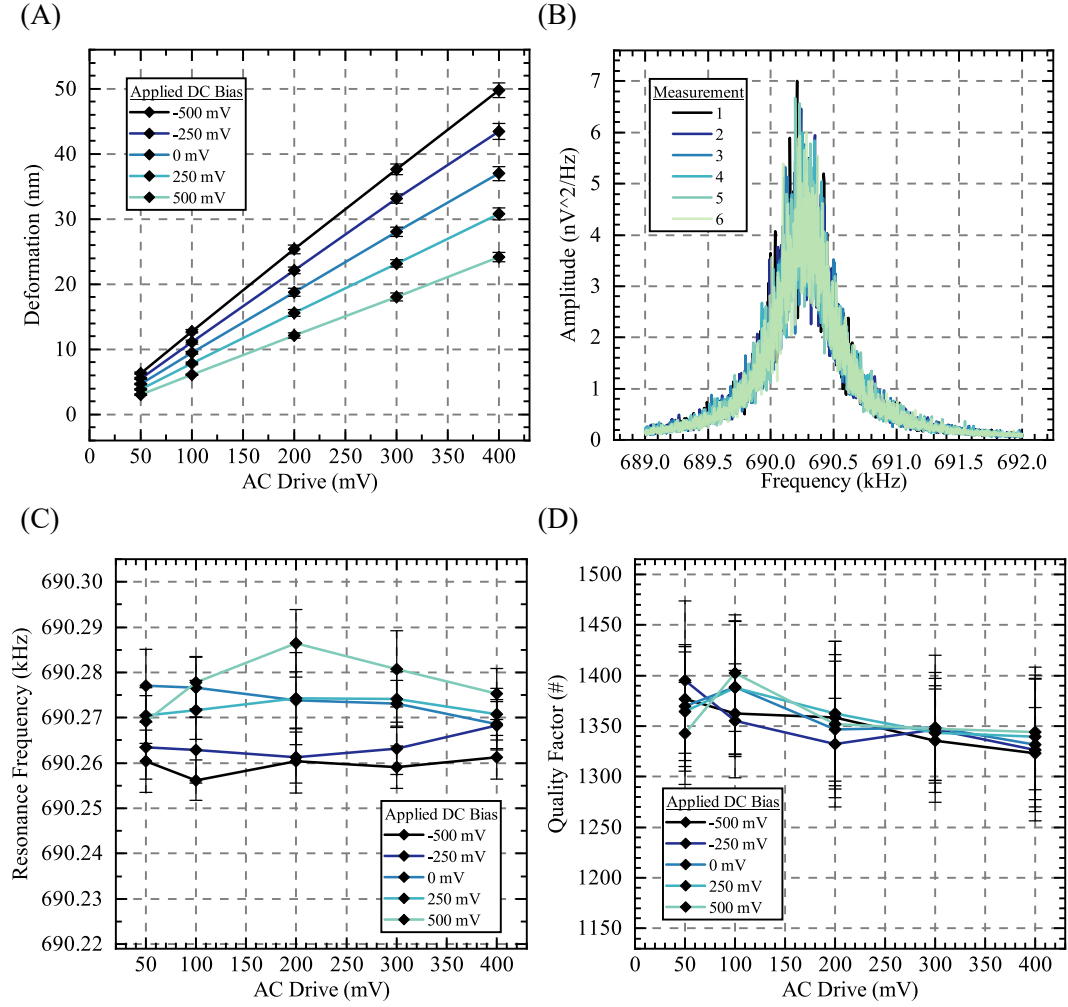


Figure 3.15 – Deformation results from experiment on a 10 μm long cantilever in Chip 2s. (A) Measured deformation during an experiment on a cantilever. Five AC drive and DC bias conditions were tested during the experiment. A linear relationship between the AC drive and deformation was found for each of the DC bias conditions. A maximum deformation of approximately 50 nm was measured for a DC bias of -500 mV and AC drive of 500 mV. (B) Overlap of all TMN measurements during an experiment on a cantilever from Chip 2s, showing very little deviation in amplitude or center frequency during the experiment. (C) Average frequency for frequency sweeps at each DC and AC condition. (D) Average quality factor for frequency sweeps at each DC and AC condition.

After fitting the TMN measurement and extracting the maximum amplitude, the responsivity was calculated for each set of five AC bias conditions by comparing the theoretical and measured TMN maximum amplitudes. The equation for calculating the responsivity can be found in Appendix A.1.6. The deformation measured in volts during the frequency sweeps at each bias condition could then be translated to nanometers by multiplication of the responsivity.

Finally, the calculated deformation, resonance frequency and quality factor were plotted against each DC and AC condition. An example of an experiment on a 10 μm long cantilever in Chip 2s can be seen in Figure 3.15. In the deformation results (Figure 3.15 A), there is an increase in deformation for negative applied DC bias. For most of the cantilevers in Chips 1s, 2s and 2a, the largest deformations were measured for a maximum DC bias of -500 mV. However, the magnitude of the deformation influence due to the DC bias varied widely between different cantilevers, even ones on the same electrode. Therefore, there is an additional deformation occurring due to the DC bias but the quantification of its effect is difficult. In the flexoelectric fitting analysis, the DC bias influence is taken into account by fitting an additional effective piezoelectric coefficient.

To determine if there was a shift in the cantilever or laser during the measurement, all the TMN measurements were plotted together to check their overlap. For example, in Figure 3.15 B, little change in the TMN was measured during the experiment on a cantilever in Chip 2s. The resonance frequency and quality factor, when considering the standard deviation, do not significantly change as well for each DC and AC condition (Figure 3.15 C and D). Several cantilevers were additionally tested on different days, in different LDV measurement modes and with different AC drive and DC bias conditions without showing any significant change in the results.

The resonance frequency and quality factor usually did not significantly change during the experiments. If there was a shift of the cantilever or laser during the experiment, the average adjusted R^2 from the frequency sweeps was below 0.95. During the flexoelectric coefficient calculation, the data from these experiments was not included.

3.6.3 Flexoelectric Coefficient Analysis

To calculate the effective flexoelectric coefficient, the deformation measured in each experiment for the different AC drive and DC bias conditions was fitted by a surface model in MATLAB. The surface fit formula was based on the equations defined in Chapter 1 for flexoelectric curvature (Equation 1.9) and piezoelectric curvature (Equations 1.4). While the HfO₂ thin films are not piezoelectric, secondary phenomena such as electrostriction and the electrostatic force can generate an effective piezoelectric effect. The definition of the effective piezoelectric coefficient due to both effects can be found in Appendix A.1.7. For HfO₂, the effective piezoelectric coefficient due to electrostriction and electrostatic force with a DC bias of 0.5 V was analytically calculated to be equal to 1.7 and 0.3 mC/m², respectively. The effective piezoelectric curvature, based on the calculated coefficients, the neutral axis

displacement and the applied DC bias values, will be approximately one order of magnitude lower than the flexoelectric curvature. However, the effective piezoelectric effect still has an impact on the deformation of the cantilevers, as can be seen in Figure 3.15 A with different DC bias conditions. Therefore, it is important to deconvolute the flexoelectric curvature from the effective piezoelectric curvature to have an more accurate coefficient calculation.

The curvature κ used in the surface fit was defined as:

$$\kappa = \frac{\mu_{eff} V_{AC}}{D_f} + \frac{e_{eff} Z_p V_{AC}}{D_f} \quad (3.1)$$

Where κ is the curvature, μ_{eff} is the effective flexoelectric coefficient, V_{AC} is the applied AC drive, V_{DC} is the DC bias, e_{eff} is the effective piezoelectric coefficient due to electrostriction and electrostatic force, Z_p is the displacement of the neutral axis relative to the center of the HfO_2 layer and D_f is the flexural rigidity.

The curvature is related to the deformation u of a cantilever by:

$$u = 12\chi_n^A Q L_{eff}^2 \cdot \kappa \quad (3.2)$$

Where Q is the quality factor of the first flexural mode resonance and L_{eff} is the effective cantilever length. The proportionality parameter χ_n^A is dependent on the mode shape and is approximately 5.34 for the fundamental resonance mode of a cantilever with electrodes covering the entire length and width [2].

As was seen in Sections 3.3.1 and 3.3.2, the beam supports for the cantilevers were partially released during the chip level fabrication. To take into account the influence of the released beam support on the dynamics of the cantilevers, finite element analysis (COMSOL) was used to model the effective length of the cantilevers, based off comparison of the experimentally measured resonance frequency to the modeled resonance frequency. In chips where the actuator release was through the sacrificial SiO_2 layer alone, the effective lengths of the cantilevers were approximately the same as the designed lengths. On the other hand, when the actuator release was through both the sacrificial SiO_2 layer and Si substrate, the effective length was approximately 1-2 μm longer than the designed lengths and the difference between the design lengths and effective lengths increased as the design length increased. The effective lengths for the cantilevers on each chip can be found in Appendix A.12.

Any data with an average adjusted R^2 below 0.95 for the Lorentzian fit of the frequency sweeps was not included in the coefficient fitting. Lower adjusted R^2 was found to be correlated with issues during the experiment, such as higher noise, a shift in the laser or the cantilever or frequency and deformation of the cantilever was significant different compared to similar counterparts. Changes in frequency or deformation of a cantilever may be due to an

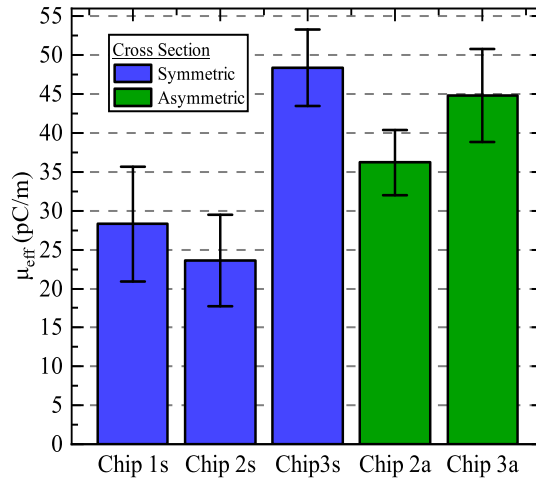


Figure 3.16 – Average flexoelectric coefficient from measurements on five chips, three with a symmetric cross section (blue) and two with an asymmetric cross section (green). One asymmetric cross section chip could not be measured due to collapse of most of the cantilevers (Chip 1a). The error bars are the summation of the error of the surface fit plus the measurement error.

incomplete release or residues on the cantilevers.

In total, seventy-four cantilevers from Chips 1s, 2s, 2a, 3s and 3a were measured, in some cases multiple times. Table 3.4 details the calculated effective flexoelectric and piezoelectric coefficients based on a average of the individual cantilevers measured in each chip. An expanded summary of the flexoelectric and effective piezoelectric coefficients found by averaging the calculated coefficients across each wafer, chip and electrode can be found in Appendix A.13.

The effective flexoelectric coefficients can be seen in Figure 3.16, separated by the type of thickness cross section. The largest flexoelectric coefficients were measured on Chips 3s and 3a; the lowest coefficients were measured on chips with symmetric thickness cross sections (Chips 1s and 2s). The total average HfO₂ effective flexoelectric coefficient is 37 ± 13 pC/m.

A fairly large standard deviation and variation in the flexoelectric coefficient can be seen across the five chips. One source of these variations is the variance in fabrication from different equipment conditions and individual chip handling. Another is that the chips were fabricated in three different fabrication runs, each of which produced slightly different releases of the cantilevers. The effective length of the cantilevers is strongly affected by the type of release and although an effort was made to calculate the appropriate effective lengths for each chip, there may be local variations in the cantilever release which shift their effective length. Having an incorrect effective length affects both the deformation calculation as well as the responsivity calculation. The focus of LDV laser may also shift slightly during measurements. However, the calculation of the responsivity should remove most of the issues surrounding alignment and focusing of the lasers onto the end of the cantilevers.

3.6. Flexoelectric Coefficient Characterization

Table 3.4 – Calculated flexoelectric (μ_{eff}) and effective piezoelectric coefficients (e_{eff}) for five chips. The type of thickness cross section is designated as s and a for symmetric and asymmetric, respectively. The effective piezoelectric coefficient is shown as $e_{eff} \cdot Z_p$ as well as e_{eff} for easier comparison to μ_{eff} . STD stands for standard deviation, which is propagated from both the surface fit as well as the measurement error. The number of beams includes repeat measurements on the same cantilevers.

Cross Section	μ_{eff} (pC/m)	STD (pC/m)	$e_{eff} \cdot Z_p$ (pC/m)	STD (pC/m)	e_{eff} (mC/m ²)	adjR ²	Measured Beams #
Chip 1s	23.6	5.9	-25.5	16.8	-26.4	0.99	13
Chip 2s	28.3	7.4	-11.7	21.9	-12.1	0.99	45
Chip 3s	48.4	4.9	-30.0	13.8	-31.0	0.99	7
Chip 2a	36.2	4.2	-11.1	23.1	-1.6	1.00	19
Chip 3a	44.8	6.0	0.6	12.9	0.1	1.00	28
Total average	37	13					105

It was expected that Chips 2a and 3a, with their asymmetric thickness cross section, would have generated larger effective piezoelectric coefficients than in Chips 1s and 2s, which have symmetric thickness cross sections. However, as can be seen in Table 3.4, the calculated effective piezoelectric coefficients vary both in the sign and the order of magnitude across the measured chips; the standard deviation was almost always larger than calculated effective piezoelectric coefficient itself, making any conclusions on the effective piezoelectric coefficient impossible.

An important note is that Chip 3a, which was fabricated in chip level run 3, demonstrated the largest flexoelectric coefficients and smallest effective piezoelectric coefficients than the other three chips, although being fabricated in a similar fashion as the chips in run 2. In particular, while the other three chips showed a measurable influence of the DC bias on the measured deformation, cantilevers on Chip 3a consistently showed very little influence of the DC bias on the deformation.

One further note is that larger flexoelectric coefficients tended to occur when lower effective piezoelectric coefficients were measured, though it is difficult to fully confirm this behavior with the large standard deviation of the piezoelectric coefficient. More measurements should be completed to confirm that the two coefficients can be properly measured independently of each. One method would be by measuring the generated curvature directly through a digital holographic microscope, thus avoiding the issue of the effective length uncertainty. Further improvements could also be made to the LDV setup to minimize noise.

Overall, the measurements demonstrate an interesting start to the understanding of the effective flexoelectric and piezoelectric coefficients in amorphous HfO₂.

3.7 Conclusion

In this chapter, the fabrication and characterization of dielectric actuators based on HfO₂ was discussed. Based on a four step process flow, several chips were produced with free-standing cantilevers. An electrical characterization found that the HfO₂/Mo electrodes have a high electrical resistance, low capacitance, low dielectric losses and linear polarization behavior versus electric field. Through XRD diffraction, the HfO₂ thin films were found to possess no significant crystal structure. More than seventy flexoelectric actuators in four chips were tested versus twenty-five AC drive and DC bias conditions and their results were analyzed to calculate an average effective flexoelectric coefficient of 437 ± 13 pC/m for 40 nm of amorphous HfO₂.

4 Discussion and Conclusion

In the previous two chapters, the work on optimizing AlN and AlScN piezoelectric thin films as well as flexoelectric thin films based on amorphous HfO₂ was examined in detail. The main results from each chapter will be briefly summarized below as well as future work that can be completed. Then, to understand the impact of the work on these thin films, two topics will be discussed. One will look at how the amorphous HfO₂ flexoelectric coefficient influences the understanding of the flexoelectric coefficient/relative permittivity relationship by analyzing the experimental results from literature across a wide relative permittivity range. The other will compare the potential curvature generation from nanoscale resonators based on piezoelectric and flexoelectric active layers to more realistically quantify which technique would be effective at what length scale. Finally, a conclusion of the doctoral work will be provided.

4.1 Sputtering Optimization of AlN And Al_{0.6}Sc_{0.4}N Thin Films

The efforts to fabricate AlN and AlScN thin films with optimal sputtering parameters and substrate conditions were summarized in Chapter 2.

First, the impact of substrate temperature, sputtering power, Ar gas concentration and multi-step deposition on the rocking curve FWHM of 50 nm thick AlN thin film was characterized. The lowest AlN rocking curve FWHM was measured at a sputtering power of 1500 W and a substrate temperature of 300°C, while the influence of the Ar gas concentration or splitting the deposition time into multiple steps was not significant. The impact of the sputtering parameters on the residual stress could not be determined due to fluctuations within the sputtering system. More deposition experiments with an expanded set of Ar gas concentrations and multistep depositions should be completed to have a better understanding of their influence on the AlN c-axis texture.

The influence of Ti or AlN seed layers deposited at two different temperatures was measured by looking at the change in AlN actuation layer rocking curve FWHM. If the seed layers are deposited at room temperature, there is no significant difference in the generated AlN

actuation layer rocking curve FWHM. When their deposition temperature was increased to 350°C, AlN seed layers were found to generate lower rocking curve FWHM in the AlN actuation layer compared to Ti seed layers. If AlN seed layers were used, their thickness was found to significantly influence the rocking curve analysis of the AlN actuation layer unless the seed layers were much thinner than the AlN actuation layers.

When testing room temperature deposited Pt, Mo and Al electrode layers on Si substrates versus AlN c-axis texture, Pt electrode layers generated the lowest AlN rocking curve FWHM values, independent of the underlying seed layer and sputtering system used to deposit the Pt films. The crystalline texture of the Mo and Al electrode layers was lower than the Pt electrodes; improving their texture may help generate better AlN c-axis texture.

Through the deposition experiments, we achieved 50 nm AlN films with a rocking curve FWHM of 2.0°, a 300% improvement to the earliest deposition tests in our sputtering system, and a piezoelectric coefficient $d_{33,f}$ of 3.5 ± 0.17 pm/V, which is comparable to values demonstrated with micron thick AlN. Some of the reasons for the large piezoelectric coefficient in our AlN thin films include the use of already highly textured Pt thin films on AlN seed layers and the very high residual stresses generated during the sputtering of our AlN thin films (~1-2 GPa). We also confirmed that the influence of several sputtering parameters and substrate conditions on sub-100 nm thick AlN films matched what was seen in the state of the art at micron thicknesses.

A study was completed on the impact of Ar gas concentration and substrate bias voltage on the c-axis texture of 1 µm thick AlScN thin films with 40% Sc concentration. Increasing the Ar gas concentration was found to lower the density of abnormal grains and the AlScN rocking curve FWHM, while the influence on residual stress was inconsistent due to fluctuations in the power sources for the sputtering system. By increasing the substrate bias voltage, the density of abnormal grains was diminished, but on the other hand, the rocking curve FWHM of the AlScN thin films increased. Further work should be completed to confirm the influence of substrate bias voltage. To generate low AlScN rocking curve FWHM values while minimizing the density of abnormal grains, our results indicate that a high Ar gas concentration and medium to low substrate bias voltage should be implemented. We were able to fabricate $\text{Al}_{0.6}\text{Sc}_{0.4}\text{N}$ thin films with a rocking curve FWHM of 1.7°, which is comparable to the state of the art in AlScN thin films with similar Sc concentrations.

One issue during the deposition experiments was the instability of the sputtering parameters, particularly the sputtering power and substrate bias. Since sputtering power and substrate bias were found to significantly affect the properties of the AlN and AlScN thin films deposited in this doctoral work, finding a way to improve the sputtering system, or moving to a more stable system, is paramount. However, despite the sputtering system instability, we were able to deposit highly c-axis textured sub-100 nm AlN films with comparable texture and piezoelectric coefficients as demonstrated in the state of the art.

Future work in AlScN thin films should include the fabrication of AlScN thin films with thicknesses between 50-100 nm and expanded deposition experiments to measure the influence

of sputtering parameters at this thickness scale on the c-axis texture, density of abnormal grains and piezoelectric response. After the sputtering of 50-100 nm AlScN thin films has been optimized, the next step is to implement AlN and AlScN thin films into actuators for potential use in NEMS applications, such as relays, switches or very high frequency filters.

4.2 Flexoelectric Actuation with Amorphous HfO₂

In Chapter 3, the flexoelectric properties of amorphous HfO₂ were investigated. First, a four mask process flow was developed to fabricate actuators with a beam cross section comprised of an amorphous HfO₂ active layer and Mo electrode layers. Two types of thickness cross sections were fabricated: a symmetric one where the Mo bottom and top electrode layer thicknesses are both equal to 25 nm; and an asymmetric one, where the Mo bottom electrode layer thickness was equal to 25 nm and the Mo top electrode layer thickness was equal to 35 nm. In both the asymmetric and symmetric thickness cross sections, a HfO₂ layer thickness of approximately 40 nm was fabricated.

Several fabrication runs were completed to optimize the manufacturing of the thin film stack at the wafer level, while during the chip level fabrication, three fabrication runs were completed, with improved results in each succeeding run. Several chips were processed to fabricate free-standing cantilevers with lengths between 10-30 μm .

Measurements of the electrical properties of the HfO₂/Mo thin films verified the low resistance of the Mo electrode layers (50-100 Ω) and resistance on the order of M-G Ω between the top and bottom electrodes through the HfO₂ layer after wire bonding. The HfO₂ thin films were determined through XRD characterization to be amorphous based on the lack of significant diffraction peaks and the broad shoulder at lower scan angles. Through capacitance-voltage curves, the HfO₂/Mo capacitors were found to have low dielectric losses at 1 kHz. The HfO₂ relative permittivity was measured through capacitance voltage curves to be approximately 15, which is lower than seen in the state of the art [243], but could be due to the amorphous property of the HfO₂ layer. An investigation of the polarization versus electric field found a linear polarization behavior up to electric field values of 2.5 MV/cm, which indicates that the HfO₂ layer is non-ferroelectric.

To characterize the effective flexoelectric coefficient of amorphous HfO₂, the deformation of more than seventy cantilevers at resonance versus different drive conditions was measured by laser Doppler vibrometry. Based on the measurements, an average effective flexoelectric coefficient of 37 ± 13 pC/m was determined for our amorphous HfO₂ thin films.

In terms of the fabrication, an investigation into crystalline HfO₂ thin films should be completed to try to increase the relative permittivity and potentially measure a larger effective flexoelectric coefficient. To better differentiate between the effective flexoelectric and effective piezoelectric effects, actuators with larger neutral axis displacements should be fabricated, for example, by increasing the asymmetry in Mo electrode layer thicknesses or leaving the

sacrificial SiO₂ layer underneath the actuators. The effective piezoelectric coefficient could also be determined through the frequency shift due to DC bias in doubly clamped beams. Another important experiment to complete in the future would be to measure the direct flexoelectric effect in the amorphous HfO₂ flexoelectric actuators to corroborate the inverse flexoelectric effect measurements made in this thesis. Displacement current levels of 10 pA have been calculated to be created due to the direct flexoelectric effect, which is a fairly low value compared to parasitic current, but measurements of charge directly may increase the signal to noise ratio.

In our actuators, it would be possible to indirectly measure the surface piezoelectric effect by altering the interface between the Mo electrode and HfO₂ layers through ion milling. Another way of measuring the surface piezoelectric effect would be by decreasing the HfO₂ thickness to 1-2 nm, though it is possible that HfO₂ will become ferroelectric at those thicknesses [244]. Finally, recent research into doped and ferroelectric HfO₂ could be channeled into fabricating thin films with stronger flexoelectric and/or piezoelectric properties than amorphous or crystalline HfO₂.

4.3 Analysis of Relationship Between Experimental Flexoelectric Coefficients from Literature and Relative Permittivity

As discussed in Chapter 1, several materials, particularly ferroelectrics, relaxors and para-electrics, have been characterized by several groups to measure their experimental flexoelectric coefficients. Higher relative permittivity materials were expected to have large flexoelectric coefficients based on the theoretically derived linear proportionality between the flexoelectric coefficients and relative permittivity (Equations 1.7 and 1.8 in Chapter 1). In many cases, though, the measured flexoelectric coefficient was orders of magnitude larger than expected, particularly when measured near the Curie temperature or temperature of maximum relative permittivity. While Ma and Cross proposed to add a scaling factor γ to help take into account the much larger flexoelectric coefficients at higher relative permittivity values, this was not enough to fully describe the experimental results [208, 209].

Is the relationship between the experimental flexoelectric coefficient and relative permittivity in reality nonlinear? In a study of the flexoelectric effect in PMN, Ma and Cross showed that a quadratic, rather than linear, relationship better matched the experimental data [208]. Do different relationships between the flexoelectric coefficient and relative permittivity arise in different magnitude ranges, or when the materials may have extrinsic contributions to the flexoelectric polarization, such as from domain-related processes or polar regions? And finally, how does the measurement of amorphous HfO₂, with its low relative permittivity compared to the state of the art, influence the analysis of the experimental flexoelectric coefficient/relative permittivity relationship?

4.3. Analysis of Relationship Between Experimental Flexoelectric Coefficients from Literature and Relative Permittivity

To try to answer these questions, the experimental flexoelectric coefficients were extracted from literature for several materials. To more accurately fit the relationship between the flexoelectric coefficient and relative permittivity, only literature that clearly stated or measured the flexoelectric coefficient μ_{12} or μ_{13} versus relative permittivity were used. In the case that the flexoelectric coefficient and relative permittivity were measured versus temperature, the flexoelectric coefficient values were extracted from both the high and low relative permittivity ranges.

The flexoelectric coefficient in the low relative permittivity range was chosen by finding data furthest above the Curie temperature or temperature where the relative permittivity was maximum (but not necessarily above the temperature where polar regions would disappear in certain materials). By extracting flexoelectric coefficients in the lower relative permittivity range, some of the large extrinsic polarization contributions from ferroelectric and/or domain-related processes should be removed. The low and high relative permittivity flexoelectric coefficients used in our analysis, along with the references, can be found in Appendix A.14.

The flexoelectric coefficient and relative permittivity were analyzed by applying linear and power law fits across the low, high and full relative permittivity ranges. For the power law fit, a linear fit was applied on a log-log plot, which should therefore give the following relationship:

$$\mu_{ex} = c\gamma\epsilon_r^k \quad (4.1)$$

Where $c = \frac{e}{4\pi a}$ as seen in Equation 1.7 from Chapter 1 and k is exponent defining the flexoelectric coefficient/relative permittivity relationship.

A power law was found to better match the experimental data in the three relative permittivity ranges. Table 4.1 shows the calculated power k and scaling factor γ with their respective errors, as well as the adjusted R^2 for each fitting. The linear fitting results can be found in Appendix A.15. Except in the case of the high relative permittivity range, the errors were one order of magnitude lower than the calculated variables. The power law fitting in the high relative permittivity range has a high error and low adjusted R^2 , most likely due to the dispersion in the flexoelectric coefficient values in this range, so no conclusions can be made.

Table 4.1 – Best power law fitting parameters in the low, high and full relative permittivity range. The effect of including the effective HfO₂ flexoelectric coefficient on the power law fitting was checked in the low and full relative permittivity ranges.

Relative Permittivity Range	k	Error	γ (10 ⁻³)	Error	AdjR ²
Low, without HfO ₂	1.8	0.3	3.8	0.3	0.70
Low, with HfO ₂	1.9	0.2	2.6	0.2	0.82
High	0.9	0.5	7.5E4	2.0E4	0.15
Full, without HfO ₂	1.9	0.2	2.5	0.1	0.85
Full, with HfO ₂	1.9	0.1	2.0	0.1	0.89

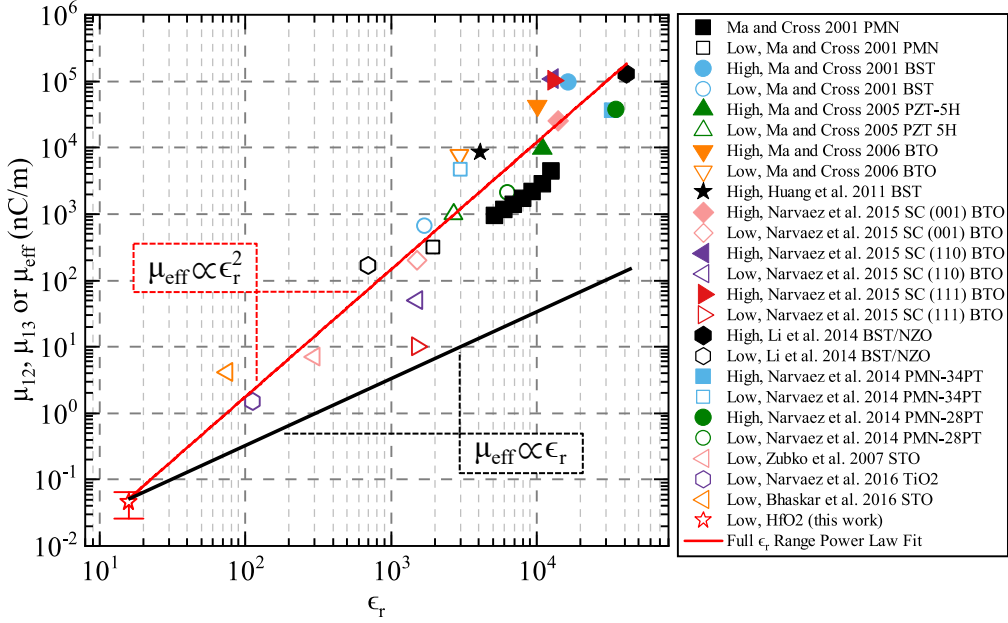


Figure 4.1 – Comparison between a linear proportionality (red line) and quadratic proportionality (black line) between experimental flexoelectric coefficients found in literature and the full relative permittivity range. Flexoelectric coefficients measured in higher and lower relative permittivity ranges are designated by solid and hollow symbols, respectively. The quadratic proportionality provides a better fit of the relationship between flexoelectric coefficients and relative permittivity. Ma and Cross measured a similar relationship within a smaller relative permittivity range for PMN (black squares) [208].

The power law fit versus a linear fit for the full relative permittivity range, which includes our HfO₂ flexoelectric coefficient, are plotted in Figure 4.1. The power law fit, which is close to a quadratic proportionality, provides a much match of the experimental data across the four orders of magnitude in relative permittivity. This quadratic proportionality was measured previously in literature by Ma and Cross in PMN over a smaller relative permittivity range, but no further remarks were made about this result in literature [208]. The scaling parameter γ serves to scale the power law, similar to its earlier inclusion in the linear relationship between experimental flexoelectric coefficients and relative permittivity discussed in literature.

As many experimental results for high relative permittivity materials exist, to strengthen the empirical relationship between experimental flexoelectric coefficient and relative permittivity, more experiments in the low relative permittivity range should be conducted in the future. Through the analysis of the state of the art to extract the measured flexoelectric coefficients, it seems likely that there are three relative permittivity ranges of interest: low, middle and high. The low range would include materials where only the intrinsic dielectric permittivity is associated with flexoelectric polarization, such as Al₂O₃ and HfO₂, as well as paraelectrics measured above temperatures where no polar regions should exist. The middle range would include paraelectric materials that may have some extrinsic polarization contributions, such

4.4. Piezoelectric versus Flexoelectric Curvature Generation at the Nanoscale

as nano polar regions, and the high range would involve materials that are ferroelectric or close to the temperature of maximum relative permittivity.

Some groups have measured the relative permittivity and flexoelectric coefficients of materials across a wide temperature range. A more extensive analysis of their results could also help to improve the understanding in the relationship between experimental flexoelectric coefficients and relative permittivity. If more materials are measured in the mid to low relative permittivity ranges, a better distinction in the power law relationship can be made in those two ranges.

An experimental investigation of dielectrics in the low permittivity range can also lead to a better understanding of the electronic contribution to the bulk flexoelectric coefficient. It has been stated that the electronic contribution should be similar to the ionic contribution in low relative permittivity dielectrics, based on order of magnitude estimates [174]. However, little experimental research has been completed on this topic. The electronic contributions were calculated for some carbon nanosystems [247] and a few dielectrics, such as SrTiO_3 and BaTiO_3 [200], but no further work has been published.

When the effective HfO_2 flexoelectric coefficient is compared to the calculated electronic flexoelectric coefficients [200], the order of magnitude in the coefficients is similar, which may mean that the electronic contribution in amorphous HfO_2 is comparable in magnitude to the ionic contribution. Part of the reason that the magnitude of the electronic contribution may be more comparable to the ionic contribution in our HfO_2 flexoelectric coefficient may be due to the fact that the film is amorphous, not crystalline, and therefore most of the ionic contribution cancels itself out. To the best of our knowledge, no other experimental work has been completed where the magnitude of the electronic contribution would be similar to the ionic contribution.

Measuring the flexoelectric coefficient in more materials with low relative permittivity, both in crystalline and amorphous forms, and particularly with no extrinsic polarization contributions, would shed more light on this topic. On top of this, ab-initio calculations of the electronic and ionic contributions could be compared to the crystalline experimental measurements, thus providing a more complete view on flexoelectric polarization.

4.4 Piezoelectric versus Flexoelectric Curvature Generation at the Nanoscale

The goal of this doctoral work was to piezoelectric and flexoelectric thin films for transduction in NEMS. To that end, 50-100 nm thick AlN films and 40 nm amorphous HfO_2 thin films were fabricated and characterized. How do these active layers compare with the state of the art in curvature generation? What could be done to increase the impact and likelihood of the AlN and HfO_2 thin films being applied in future NEMS? Some answers to these questions will be discussed in the following paragraphs.

Chapter 4. Discussion and Conclusion

One method of gauging different thin films as actuation layers in MEMS and NEMS is by how much curvature the films generate for an applied drive, which is defined as:

$$\frac{\kappa}{V} = \frac{e_{31}Z_P}{D_f} + \frac{\mu_{flex}}{D_f} \quad (4.2)$$

Where the first right-hand term is for the normal piezoelectric effect and the second is for the flexoelectric effect, as discussed in Chapter 1 (Equations 1.4 and 1.9). If piezoelectric thin films are under study, only the first right-hand term should be included in the curvature calculation; similarly only the second right-hand term should be used to calculate the curvature for flexoelectric thin films. By looking at the curvature per applied drive, the influence of both the coefficient mediating the electromechanical effect as well as the total thickness of the actuator necessary to generate the curvature are taken into account.

The piezoelectric term in Equation 4.2 is also mediated by the distance between the neutral axis position and the center of the piezoelectric layer Z_P . Since the flexural rigidity is related to the cube of the thickness (Appendix A.1.1), the piezoelectric curvature's thickness dependence shifts from a t^{-3} to a t^{-2} , while the flexoelectric curvature thickness dependence is maintained as t^{-3} . Therefore, the effect of decreasing the actuation layer thickness will be stronger in flexoelectric actuators than piezoelectric actuators.

To calculate the curvature per applied drive for our piezoelectric AlN layers, we estimated a e_{31} of -1 C/m² based off comparison of our measured piezoelectric coefficient $d_{33,f}$ to the literature on AlN [75]. However, since the e_{31} was not directly measured for these AlN thin films, the calculated curvature generation should only be considered as an order of magnitude estimate. The layers in the curvature calculation for our piezoelectric AlN layer were 15 nm AlN seed layer, 25 nm Pt bottom electrode, 50 nm AlN active layer and 25 nm Pt top electrode, based on the full stack of layers where the piezoelectric response was measured in Chapter 2.

For the HfO₂ curvature calculation, the layers were 25 nm Mo bottom electrode, 40 nm HfO₂ active layer and 25 nm top electrode, similar to the fabricated devices in Chapter 3. The effective flexoelectric coefficient was set as 37 pC/m.

In Figure 4.2, the calculated curvature per applied drive for our flexoelectric HfO₂ and piezoelectric AlN layers is plotted against the state of the art in flexoelectric and piezoelectric actuation layers. Additionally, the curvature generation in an effective piezoelectric Si₃N₄ actuator is included in the figure. As discussed in Chapter 3, an effective piezoelectric coefficient in dielectrics can be created due to electrostriction or the electrostatic force between two electrodes on a dielectric material. Recently, this coefficient was measured in Si₃N₄ [248]; due to the very low thickness of the Si₃N₄ actuation layer, the curvature generation is on par with much thicker piezoelectric actuators. In comparison to actuation layer thicknesses below 100 nm, the effective piezoelectric curvature is much lower.

4.4. Piezoelectric versus Flexoelectric Curvature Generation at the Nanoscale

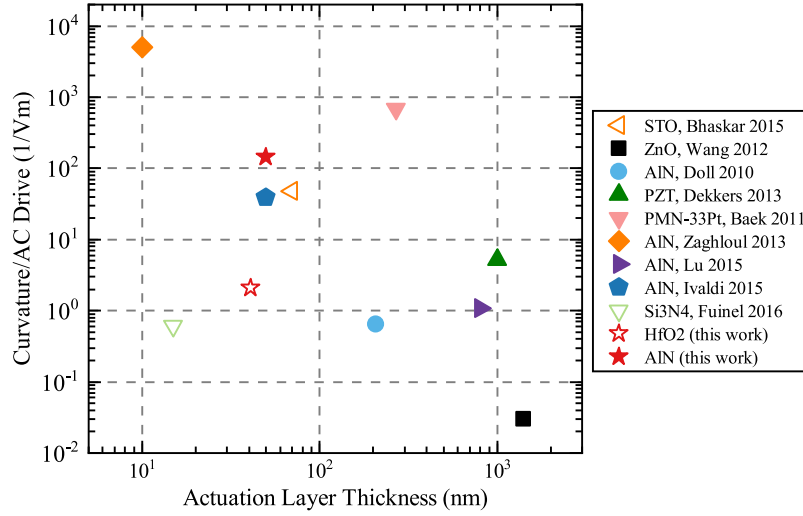


Figure 4.2 – Comparison of curvature generation for an applied drive from flexoelectric and piezoelectric thin films in the state of the art and from the AlN and HfO₂ thin films developed in this doctoral work. The references for the state of the art are: SrTiO₃ [16], ZnO [27], AlN [116, 113, 19, 13], PZT [28] and PMN-33PT [29]. Additionally, the curvature generated by the electrostatic force creating an applied piezoelectric effect in silicon nitride (Si₃N₄) is included [248]. HfO₂ flexoelectric layers were found to have comparable curvature generation to thicker piezoelectric thin films, but still much lower results compared to SrTiO₃ flexoelectric layers and sub-100 nm AlN piezoelectric layers. The AlN value from this work should only be taken as an order of magnitude estimate, since the traverse piezoelectric coefficient e_{31} was not directly measured.

The calculated curvature generation of the HfO₂ flexoelectric layer is not much larger than the Si₃N₄ effective piezoelectric layer, but the difference in the two effects would be more apparent when the HfO₂ thickness is decreased: an order of magnitude difference in curvature generation is achieved. The curvature generation for flexoelectric HfO₂ thin films is comparable to values found for thicker piezoelectric layers, but is approximately one order of magnitude lower than for sub-100 nm thick AlN-based actuators as well as flexoelectric actuators based on SrTiO₃, mostly due to the difference in effective flexoelectric coefficients [16].

The curvature generation based on our AlN thin films is comparable to AlN-based actuators with the same thickness [13] as well as the flexoelectric curvature generation by SrTiO₃ [16]. Only the curvature generation from thinner AlN films, which benefits from a lower flexural rigidity, and thicker PMN-PT films, which have a significantly larger piezoelectric coefficient, exceed the curvature generation in the AlN thin films of this work.

The difference between the curvature per applied drive between our AlN and HfO₂ thin films is approximately two orders of magnitude, which would initially suggest that further investigation in amorphous HfO₂ flexoelectric layers is unnecessary. However, as discussed above, the thickness dependence of flexoelectric actuation makes it possible that thinner flexoelectric actuators can exceed in curvature generation compared to piezoelectric actuators

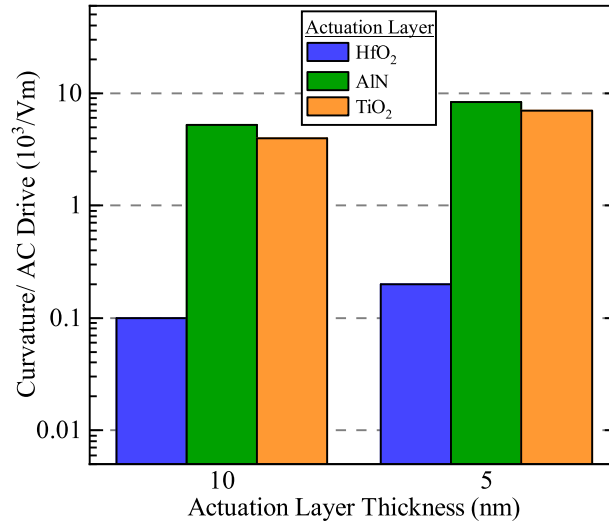


Figure 4.3 – Comparison of curvature generation per applied AC drive for 10 and 5 nm thick HfO₂, TiO₂, AlN films as a part of a capacitor stack. All electrodes are Pt. An additional 10 nm thick AlN seed layer was a part of the AlN capacitor stack. Decreasing the actuation layer thickness does not significantly improve the curvature generation from HfO₂ films versus AlN films. However, a dielectric with a higher relative permittivity, such as TiO₂, may be able to generate similar curvature as AlN thin films.

at a certain thickness scale. Flexoelectric actuation does not require displacement of the neutral axis, which reduces the total actuator thickness compared to piezoelectric actuators.

A demonstration of the above discussion can be seen in Figure 4.3, where curvature per applied AC drive of 5 and 10 nm thick flexoelectric actuation layers based on HfO₂ and TiO₂ were analytically compared to 10 nm thick piezoelectric AlN actuation layers. The metal electrode layers were set as 10 nm Pt to have a realistic thickness that could be consistently fabricated in most sputtering systems. An additional 10 nm AlN seed layer was included in the AlN curvature generation calculation to displace the neutral axis. The same estimated $e_{31,eff}$ for our AlN thin films discussed above in this section is also used for the curvature generation analysis. With decreasing thickness of the actuation layer, it is likely that our AlN piezoelectric coefficient will decrease, but the choice was made to use the highest piezoelectric coefficient expected in the AlN thin films. The data from Figure 4.3 can be found in Appendix A.16.

When the HfO₂ and AlN actuation layer thicknesses are decreased from the experimental values seen in Figure 4.2 (40 nm and 50 nm respectively) to 10 nm, the difference in the curvature generation between the two types of actuation decreases from two to one order of magnitude, which represents a significant improvement in curvature generation from flexoelectric actuation with an amorphous, high-k dielectric. However, further decreasing the HfO₂ actuation layer thickness to 5 nm does not significantly improve the curvature generation. Therefore, the flexoelectric coefficient would need to be increased for the HfO₂ flexoelectric curvature generation to be more comparable to the curvature generated by an AlN layer. To

increase the flexoelectric coefficient in HfO_2 , a crystalline instead of amorphous thin film can be used to increase the relative permittivity as well as the ionic contribution to the bulk flexoelectric coefficient. Additionally, doping HfO_2 or annealing HfO_2 layers with titanium nitride electrodes can induce a ferroelectric response in the thin film, which would greatly increase the curvature generation [249, 244]. To confirm these hypotheses, the flexoelectric coefficients in crystalline and ferroelectric HfO_2 thin films should be measured in the future.

TiO_2 is another high-k dielectric that can be considered for flexoelectric actuation at the nanoscale. If the effective flexoelectric coefficient of TiO_2 is as high at the nanoscale as was seen for bulk samples [193], then the TiO_2 flexoelectric curvature generation at 10 and 5 nm actuation layer thicknesses is comparable to the AlN piezoelectric curvature generation. This is a promising result as TiO_2 is a high-k dielectric that is also easier to fabricate compared to perovskite-based flexoelectric layers at the nanoscale. Similar to HfO_2 , TiO_2 can be deposited through several techniques (ALD, PLD, sputtering, etc.) and has a large relative permittivity of 80-110 [243]. There are, however, some downsides to using TiO_2 instead of HfO_2 , such as lower electrical breakdown field and more fluctuation in the oxidation states, which affects the conductivity [243]. An investigation should be made into nanoscale TiO_2 layers to measure its flexoelectric and electrical properties and determine if TiO_2 flexoelectric layers are a viable alternative to AlN piezoelectric layers in NEMS.

4.5 Conclusion

In this thesis, the use of piezoelectricity and flexoelectricity for the actuation of nanoelectromechanical systems was investigated. In one part of the thesis, 50-100 nm thick AlN thin films were fabricated with crystalline and piezoelectric characteristics similar to micron thick layers by optimizing the reactive sputtering parameters and substrate conditions. An initial investigation into the influence of two reactive sputtering parameters on 1 μm AlScN films with 40% Sc concentration was also completed with promising results. Future work in AlScN thin films involves downscaling the layer thickness and expanding the deposition experiments to confirm the optimal sputtering parameters. After this, it is envisioned to integrate the optimized AlN and AlScN thin films into actuators to investigate their piezoelectric properties.

A second part of the thesis was focused on the fabrication and characterization of a novel flexoelectric actuator based on a 40 nm thick amorphous HfO_2 layer. A four mask process flow was developed to fabricate free-standing cantilevers and doubly-clamped beams and several chips were successfully processed for experiments. The amorphous HfO_2 layers were found to have a high resistance, low dielectric losses and a relative permittivity of 15, as well as a non-ferroelectric polarization behavior up to electric fields of 2.5 MV/cm. By measuring the deformation of the cantilevers at resonance versus different drive conditions with an LDV, the HfO_2 effective flexoelectric coefficient could be calculated. To the best of our knowledge, the amorphous HfO_2 thin films are the lowest permittivity material for which the flexoelectric effect has been quantitatively measured. Several future projects are envisioned after the

Chapter 4. Discussion and Conclusion

initial success of these measurements, including measurements of the direct flexoelectric effect, fabrication and characterization of crystalline HfO_2 -based actuators and experiments to determine if the surface piezoelectric effect can be indirectly measured by modifying the HfO_2 /metal electrode interface.

A Appendix

A.1 Supplementary Formulas

A.1.1 Flexural Rigidity

The flexural rigidity D_f is defined as:

$$D_f = \frac{E_Y t^3}{12(1 - \nu^2)} = \frac{1}{3} \sum_{n=1}^n \frac{E_{Y,n} t_n^3}{(1 - \nu_n^2)} \quad (\text{A.1})$$

Where E_Y is the Young's modulus of the layer, t is the layer thickness, ν is the Poisson's ratio of the layer and n is the number of layers.

A.1.2 Residual Stress Calculation

The residual stress σ of one layer or several deposited thin films can be calculated through Stoney's formula [250]:

$$\sigma = \frac{E_{Si}}{6(1 - \nu_{Si})} \frac{t_{Si}^2}{t_{film}} \left[\frac{1}{R} - \frac{1}{R_0} \right] \quad (\text{A.2})$$

Where E_{Si} and ν_{Si} are the Young's modulus and Poisson's ratio of the Si substrate, t_{Si} and t_{film} are the thicknesses of the Si substrate and deposited thin film(s), and R_0 and R are the radii of curvature before and after the deposition, respectively.

To determine the residual stress of each thin film, the radius of curvature would need to measure after the deposition of each layer. Then, as long as the thickness of each thin film is known, the individual residual stress values can be found by the following equation:

$$\sigma_{fs} t_{fs} = \sum_{n=1}^n \sigma_n t_n \quad (\text{A.3})$$

Where σ_{fs} is the residual stress measured after the deposition of the last layer in the full stack of thin films, t_{fs} is the thickness of the full stack of deposited thin films, σ_n are the residual stress values measured after the deposited of each layer in the full stack and t_n is the thickness of each layer.

A.1.3 Two Term Gaussian for XRD Analysis

To separate the diffraction contributions from the AlN seed and actuation layers to the total (0002) diffraction peak from a theta2theta curve, the following formula was used:

$$A_1 \exp[-(x - A_2)^2 / 2A_3^2] + B_1 \exp[-(x - B_2)^2 / 2B_3^2] \quad (\text{A.4})$$

Where the first and second terms correspond to the seed and actuation layers, respectively. Variables A_2 and A_2 were found by fitting the theta2theta diffraction data from the AlN seed layers alone, while the other variables were left free to be fitted.

A.1.4 Lorentzian Fit

The Lorentzian fit for the sweep and TMN measurements in Chapter 3 is defined as:

$$y_{norm} = y_{offset} + \frac{A_0 f_0}{2\pi Q \left((f - f_0)^2 + \left(\frac{f_0}{2Q} \right)^2 \right)} \quad (\text{A.5})$$

Where y_{norm} is the squared and normalized raw amplitude data from the measurement, $y_{norm,offset}$ is the normalized calculated offset due to background noise, A_0 is the calculated peak amplitude, f_0 is the calculated center frequency and Q is the calculated quality factor. The standard error for each fitted parameter is calculated based off each of their confidence intervals.

A.1.5 Theoretical Thermomechanical Noise Spectral Density

The theoretical TMN noise magnitude at the tip of a mechanical cantilever resonating at the fundamental resonance frequency is defined as [2]:

$$y_{max,theory} = \frac{k_B T Q_{TMN}}{2\pi^3 m_{eff} f_{TMN}^3} \quad (\text{A.6})$$

Where k_B is the Boltzmann constant, T is the temperature of the measurement (approximated to 300K), and Q_{TMN} and f_{TMN} are the quality factor and center frequency from the TMN measurement. The effective mass of the cantilever m_{eff} is approximated by:

$$m_{eff} = 0.25 L_{cant} w_{cant} \sum_{n=1}^n \rho_n t_n \quad (\text{A.7})$$

Where L_{cant} and w_{cant} are the effective length and width of the cantilever, and ρ and

t_{layer} are the volume density and thickness of each layer in the cantilever.

A.1.6 Responsivity in LDV Measurements

If the experimental thermomechanical noise (TMN) is measured as a power spectral density, then responsivity of the measurement system can be obtained by compared the theoretical versus experimental TMN. The responsivity of the LDV in nm/V was calculated through the following equation:

$$R\left(\frac{nm}{V}\right) = \left(\frac{y_{max,exp}}{y_{max,theory}}\right)^{-\frac{1}{2}} \quad (A.8)$$

Where $y_{max,exp}$ is the maximum amplitude found in the Lorentzian fitting of the TMN measurement and $y_{max,theory}$ is the theoretical TMN at the tip of a cantilever. Both parameters have units of power spectral density.

A.1.7 Effective Piezoelectric Coefficients due to Secondary Phenomena

Electrostatic Force

A free-standing beam using electrostatic actuation can be comprised of a dielectric material sandwiched by electrodes. When an electric field is applied between the electrodes, the dielectric will be compressed in the direction of the electric field, which will then, through the Poisson effect, generate a expansion of the dielectric material in the other two directions. If the neutral axis of the beam is shifted relative to the center of the dielectric material and a AC drive is applied, a curvature can be generated. Thomas et al. derived the effective piezoelectric coefficient for free standing beams based on electrostatic actuation as [251]:

$$e_{31,ES} = \frac{\nu_d \epsilon_r \epsilon_0 V_{DC}}{t_d} \quad (A.9)$$

Where ν_d , ϵ_r and t_d denotes the Poisson's ratio, relative permittivity and thickness of the dielectric material and V_{DC} is the applied DC voltage across the dielectric thickness.

Electrostriction

Electrostriction is a second-order electromechanical coupling between strain and polarization existing in all dielectrics. The generalized constitutive equation which include both the piezoelectric and electrostrictive effects is:

$$\epsilon_{ij} = s_{ijkl}\sigma_{kl} + d_{ijk}E_k + M_{ijkl}E_kE_l \quad (\text{A.10})$$

Where the first two right-hand terms are Hooke's law (s and σ are the mechanical compliance and stress tensors, respectively) and the converse piezoelectric effect (d is the piezoelectric tensor and E is the electric field). The last right-hand term denotes the electrostrictive effect. The electrostriction coefficient M , is theorized to be non-zero in all dielectrics. The electrostriction effect is not symmetric; there is no direct electrostriction effect such that the strain squared will generate a polarization [252]. The electrostrictive coefficients have been measured for a variety of materials [253, 254, 255].

The electrostriction coefficient M has been found to be inversely proportional to the relative permittivity and mechanical compliance; it can be approximated by $M = \frac{\epsilon_r \epsilon_0}{E_Y}$ [253], where ϵ_r and ϵ_0 are the relative and vacuum permittivities and E_Y is the Young's modulus of the dielectric material.

For a freestanding beam composed of a dielectric is sandwiched between electrodes, the application of an electric field between the electrodes will produce a strain within the dielectric due to the electrostrictive effect, which will then polarize the material. If the neutral axis of the beam is displaced relative to the center of the dielectric layer and an AC drive is applied, a curvature can be generated due to an effective piezoelectric effect from electrostriction. The curvature equation due to both the piezoelectric and electrostrictive effects is:

$$\kappa = \frac{Z_p t_d E_{AC}}{D_f} (e_{31} + E_Y M E_{DC}) \quad (\text{A.11})$$

Where Z_p is the distance between the neutral axis position and the center of the dielectric/piezoelectric layer, t_d is the thickness of the dielectric/piezoelectric layer, D_f is defined in Appendix A.1, e_{31} is the piezoelectric coefficient, E_{AC} is the applied AC drive to generate the curvature and E_{DC} is the DC bias field used to generate the polarization within the dielectric material.

Based off the above equation, an effective piezoelectric coefficient can be derived based the application of a DC bias V_{dc} on a dielectric sandwiched between electrodes:

$$e_{31,EL} \sim \frac{\epsilon_r \epsilon_0 V_{DC}}{t_d} \quad (\text{A.12})$$

A.2 Matlab Codes used in Doctoral Work

Listing A.1 – Calculates the difference between the neutral axis position and center of the dielectric layer

```

1 function f = beam_Zp(t_array,z0,call)
  %This function will find the difference between the piezoelectric
3 %layer center and neutral axis position for beams with either 1 or 2
  metal
  %layers above the piezoelectric layer (call 1 or 2 respectively)
5 if call == 1
    t_piezo_center = sum(t_array)-t_array(length(t_array))...
7     -t_array(length(t_array)-1)/2;
    f = z0-t_piezo_center;
9 elseif call == 2
    t_piezo_center = sum(t_array)-t_array(length(t_array))-t_array(length
11 (t_array)-1)...
    -t_array(length(t_array)-2)/2;
    f = z0-t_piezo_center;
13 else
    f = 'error';
15 end

```

Listing A.2 – Calculates the flexural rigidity/total thickness/equivalent volume density

```

1 function f = beam_Zp(t_array,z0,call)
  %This function will find the difference between the piezoelectric
3 %layer center and neutral axis position for beams with either 1 or 2
  metal
  %layers above the piezoelectric layer (call 1 or 2 respectively)
5 if call == 1
    t_piezo_center = sum(t_array)-t_array(length(t_array))...
7     -t_array(length(t_array)-1)/2;
    f = z0-t_piezo_center;
9 elseif call == 2
    t_piezo_center = sum(t_array)-t_array(length(t_array))-t_array(length
11 (t_array)-1)...
    -t_array(length(t_array)-2)/2;
    f = z0-t_piezo_center;
13 else
    f = 'error';
15 end

```

Listing A.3 – Calculates the neutral axis location within a thickness cross section

```

1 function f = beam_Z0orEeq(E_array,t_array,call)
   %This function will calculate either the neutral axis location or just
   the
3 %equivalent Young's modulus for a given beam condition.
   if call == 1
5       for n = 1:1:length(E_array)
           if n == 1
7               z0_num = .5*E_array(n)*t_array(n)^2;
               z0_den = E_array(n)*t_array(n);
9               t_tot = t_array(n);
           else
11              z0_num = z0_num +.5*E_array(n)*((t_array(n)+ ...
                  t_tot)^2-(t_tot)^2);
13              z0_den = z0_den +E_array(n)*t_array(n);
                  t_tot = t_tot+t_array(n);
15          end
        end
17        f = z0_num/z0_den;
    elseif call == 2
19        for n = 1:1:length(E_array)
            if n == 1
21                z0_den = E_array(n)*t_array(n);
                t_tot = t_array(n);
23            else
                z0_den = z0_den +E_array(n)*t_array(n);
25                t_tot = t_tot+t_array(n);
            end
27        end
        f = z0_den/t_tot;
29    else
        f = error('Z0 function not working');
31    end

```

Listing A.4 – Fits a Gaussian to a XRD theta2theta or rocking curve

```

1 function [f,gof] = xrdgaussfit(xrddata)
   % This function fits a Gaussian onto a theta2theta or rocking curve peak
3 [sortedX,sortingIndices] = sort(xrddata(:,2),'descend');
   fit1 = fitttype('A*exp(-(x-B)^2/(2*C^2))+D*x+E');
5 options = fitoptions('Method','NonlinearLeastSquares','StartPoint',...
        [sortedX(1) xrddata(sortingIndices(1),1)...
7        0.1 0 0]);
   [f,gof] = fit(xrddata(:,1),xrddata(:,2),fit1,options);
9 end

```

Appendix A. Appendix

Listing A.5 – Calculates the effective flexoelectric and piezoelectric coefficient from the deformation measurements on a cantilever in the first resonance mode

```
1 function coeffs = ldv_coeffcalc(V_DC,V_AC,MaxAmp,beamprop,Length)
2 % Apply a surface fit to calculate the effective flexoelectric and
3 % piezoelectric coefficients based on the deformation experiments.
4 [x,y,z] = deal([]);
5 %conversion from deformation to curvature
6 coeff_conv = 12*beamprop(1)/5.34/Length^2;
7 % set data to be used in fitting
8 for i=1:length(V_DC)
9     x = [x;V_AC']; % x axis is AC drive
10    if length(V_AC) == 3 % y axis is DC bias
11        y = [y;[V_DC(i);V_DC(i);V_DC(i)]];
12    elseif length(V_AC) == 4
13        y = [y;[V_DC(i);V_DC(i);V_DC(i);V_DC(i)]];
14    elseif length(V_AC) == 5
15        y = [y;[V_DC(i);V_DC(i);V_DC(i);V_DC(i);V_DC(i)]];
16    end
17    % z axis is the deformation data
18    z = [z;MaxAmp(i,:)'.*coeff_conv];
19 end
20 XY = [x,y]; % for linear regression function
21 T = [1 0 0;1 1 0]; % denoting the function: b*x+c*x*y
22 fit_lm = fitlm(XY,z,T); % find the solution to the above function
23 % define the coefficients
24 coeffs_fit_lm = fit_lm.Coefficients;
25 coeffs.u_eff = coeffs_fit_lm.Estimate(1);
26 coeffs.e_eff_Zp = coeffs_fit_lm.Estimate(2);
27 coeffs.e_eff = coeffs_fit_lm.Estimate(2)/beamprop(4); %divide by Zp
28 coeffs.adjR2 = fit_lm.Rsquared.Adjusted;
29 %% Standard Deviation Calculations
30 coeffs.u_eff_std = coeffs_fit_lm.SE(1)*sqrt(fit_lm.NumObservations);
31 coeffs.e_eff_Zp_std = coeffs_fit_lm.SE(2)*sqrt(fit_lm.NumObservations);
32 coeffs.e_eff_std = coeffs_fit_lm.SE(2)*sqrt(fit_lm.NumObservations)/
33     beamprop(4);
34 end
```

Listing A.6 – Fits a Lorentzian to the sweep measurement during the deformation experiment

```

1 function results = ldv_lorentzfit_sweep(structs)
  % Modification of Annalisa de Pastina and Damien Maillard's code.
3 % This code takes the data from the files provided by the Zurich
  % Instrument lock-in amplifier from a sweep measurement, makes a
  Lorentzian
5 % fit of the square of the amplitude signal and returns a struct with the
  % fitted and raw results.
7 [~,c] =size(structs); %Get the number of rows and columns
  points=structs{1,1}.samplecount; %Number of points acquired during the
  sweep
9 [RawFreq,RawAmp,NormalAmpSqr,fitlor3] = deal(zeros(points,c));
  [MaxAmp,Q,ResF,adjR2,YOffset] = deal(zeros(1,c));
11 guessQ = 1500; % to help the fit function get accurate results
  for i = 1:1:c
13     RawFreq(:,i) = structs{1,i}.frequency(1,:); % raw frequencies
        RawAmp(:,i) = structs{1,i}.r(1,:); % raw amplitudes
15     NormalAmpSqr(:,i) = (RawAmp(:,i)/max(RawAmp(:,i))).^2; % amplitude
        is normalized and squared
        [maxamp_nor, index] = max(NormalAmpSqr(:,i)); % finds max amplitude
        and index
17     guessamp=pi*RawFreq(index,i)/2/guessQ*maxamp_nor; % guesses the
        normalized max amplitude
        ftype = fitype('off1 + amp*f0/2/pi/Q/((x - f0)^2 + (f0/2/Q)^2)');
19     opts = fitoptions('Method','NonlinearLeastSquares','Algorithm',...
        'Levenberg-Marquardt','TolX',1e-10,'TolFun',1e-10,'StartPoint',
        ...
21     [guessQ guessamp RawFreq(index,i) 0]);
        [fitlor,gof] = fit(RawFreq(:,i), NormalAmpSqr(:,i), ftype, opts); %
        fitting data
23     fitlor3(:,i) = fitlor(RawFreq(:,i))*max(RawAmp(:,i))^2; %
        unnormalized fit data, squared
        confid_inter = confint(fitlor); % confidence intervals
25 end
end

```

A.3 AlN Wafer Catalog

Wafer #	Seed Layer	Bottom Electrode	Bottom Electrode Sputtering System	Bottom Electrode Stress	AlN Substrate Temperature	Applied Sputtering Power	Multistep Deposition	Ar/N ₂ Gas Ratio	Full Stack or AlN+Top Electrode Residual Stress	AlN FWHM	Bottom Electrode FWHM
				MPa	°C	W	s		MPa	°	°
53814	AlN	Pt	Spider	NA	350	1500	50s10s	10/40	-1234	2.9	
53809	AlN	Pt	Spider	NA	350	1500	50s10s	0/50	-1486	2.6	
53808	AlN	Pt	Spider	NA	350	1500	40s20s	10/40	-1601	3.3	
54023	AlN	Pt	Spider	NA	350	1500	40s20s	0/50	-1820	2.8	
53106	AlN	Pt	Spider	NA	350	1500	60s	10/40	-810	2.8	
53877	AlN	Pt	Spider	NA	300	1500	50s10s	10/40	-791	2.6	
53102	AlN	Pt	Spider	NA	200	1500	50s10s	10/40	-1973	2.9	
53111	AlN	Pt	Spider	NA	300	1250	50s10s	10/40	-1486	3.1	
55146	AlN	Pt	Spider	NA	300	1000	50s10s	10/40	-1334	3.6	
74089	AlN	Al	Spider	409	300	1500	105s	10/40	-122	5.5	
74086	AlN	Mo	Spider	1876	300	1500	105s	10/40	-696	5.9	8.8
74088	AlN	Pt	Spider	-935	300	1500	105s	10/40	-389	2.8	4.3
68734	Ti	Mo	Spider	-242	300	1500	105s	10/40	-644	3.6	4.2
68733	Ti	Pt	Spider	-1394	25	1500	105s	10/40	-1044	3.5	4.0
68738	Ti	Pt	Spider	-1369	150	1500	105s	10/40	-575	2.7	4.1
68739	Ti	Pt	Spider	-1159	300	1500	105s	10/40	-396	2.6	4.2
68736	Ti	Al	DP650	-11	300	1500	105s	10/40	-131	4.5	
68735	Ti	Mo	DP650	-452	300	1500	105s	10/40	-711	7.5	9.0
74087	Ti	Pt	DP650	-1081	300	1500	105s	10/40	-266	2.8	6.2

Figure A.1 – AlN catalog with all depositions discussed during Chapter 2.

A.4 Al_{0.6}Sc_{0.4}N Wafer Catalog

Wafer #	Applied Substrate Bias Power W	Measured Substrate Bias Power	Substrate Bias Voltage V	Reflected Power W	Chamber Pressure E-3 mbar	Gas Ratio	Deposition Rate nm/min	Residual Stress MPa	FWHM °	Abnormal Grain Density μm ⁻²
84332	3	2.06	49.72	0.07	5.57	10:40	50.6	-251.2	1.75	9.75
84331	3	2.07	50.7	0.016	4.84	0:50		-162.8	1.92	30.46
83605	3	2.03	60.63	0	5.55	20:30	54.2	-550.1	1.70	0.40
73851	4	3.08	65.44	0	4.83	0:50	45.75	-1019.0	3.00	2.47
73852	4	3.09	73.16	0	5.45	10:40	50.40	-576.0	6.03	0.00
83577	3	2.04	77.22	0	5.98	30:20		-246.5	2.05	0.02
70228	4	3.09	80.47	0	5.15	0:50	37.05	-916.0	3.95	2.25
85576	3	2.08	73.9	0	5.67	10:40	50.9	-332.8	2.25	0.07
73853	5	4.05	83.89	0	4.89	0:50	44.60	-1043.0	4.34	1.69
73854	6	5.07	97.51	0	5.22	0:50	43.10	-1099.0	19.69	0.97
83821	4	3.04	98.1	0	5.76	0:50		-724.6	2.18	1.40
83743	4	3.06	82.5	0	5.71	10:40		-471.8	2.52	1.44
73855	5	4.08	88.24	0	5.63	10:40	49.00	-572.0	Large	0.00
73856	6	5.06	98.34	0.007	5.75	10:40	46.25	-566.0	Large	0.00

Figure A.2 – AlScN (40% Sc concentration) catalog with all depositions discussed during Chapter 2.

A.5 Etch Test Tables

		Etch Rates			
	Etch Test	Filmetric	Average GoF	Ellipsometer	STD (Ellipsometer)
		nm/min		nm/min	nm/min
HfO₂	1:3 40% KOH:H ₂ O (RT, 30°C)	0.00	0.84		
	37% HCl (RT)	-0.01	0.39	0.00	1.21
	STS Pt_etch (20 sccm Cl ₂ /70 sccm Ar)	15.42	0.78	28.52	1.21
	STS W_etch (50 sccm SF ₆)	19.80	0.90	21.07	1.21
	IBE, low recipe (300 W, 500 mA/cm ²)	160.00	0.33	24.00	0.07
	BHF 7:1			5.05	0.01
	1:4 HF 49%:H ₂ O	71.42	0.76	66.16	1.21
	uETCH, recipe 1			-0.14	0.05
		Etch Rates			
	Etch Test	Filmetric	Average GoF	Ellipsometer	STD (Ellipsometer)
		nm/min		nm/min	nm/min
TiO₂	STS Pt_etch (20 sccm Cl ₂ /70 sccm Ar)	31.34	0.67	26.50	1.44
	STS W_etch (50 sccm SF ₆)	149.79	0.37	138.62	1.44
	IBE, low recipe (300 W, 500 mA/cm ²)	16.99	0.44	19.29	0.72
	1:3 40% KOH:H ₂ O (RT, 30°C)	0.06	0.64		
	37% HCl (RT)	0.05	0.67	0.03	1.44
	BHF 7:1			2.17	0.02
	1:4 HF 49%:H ₂ O	96.47	0.40		
		Etch Rates			
	Etch Test	Profilometer	STD (Profilometer)	By Eye	
		nm/min	nm/min	nm/min	
Mo	STS Pt_etch (20 sccm Cl ₂ /70 sccm Ar)			16.00	
	STS W_etch (50 sccm SF ₆)			52.26	
	BHF 7:1	-0.54	-0.087		
	1:4 HF 49%:H ₂ O	-3.9	-0.704		
	uETCH, ultralow recipe	0.24	0.063		
	uETCH, recipe 5	0.11	0.03		

Figure A.3 – Etch test results for HfO₂, TiO₂ and Mo thin films. A spectroscopic reflectometer (FilMetrics F20-UV) and ellipsometer (Sopra GES 5E) were used to measure HfO₂ and TiO₂. Even with fine tuning of the measurement fitting, the reflectometer measurements were not high resolution. The ellipsometer provided much higher resolution and more reasonable error. For the Mo thickness measurements, the profilometer (Bruker Dektak XT) was used for wet etch tests, while the dry etch tests could be completed by eye through a viewing glass. The HF-based etch rate was very low for Mo, which made low error measurements difficult.

A.6 Wafer Level Runcard

Wafer Level Fabrication Runcard			
Substrates: silicon <100>, 100mm, 525um thick, single side polished			
Step N°	Description	Equipement	Program / Parameters
0	<i>Wafer Preparation</i>		
0.1	Oxidation	RCA request	295 um wet oxide, done by Cmi staff
0.2	Measure SiO2 thickness	Z3/Nanospec	Measure 48 pts
0.3	Measure wafer curvature	Z15/Toho	2x in 2 directions
1	<i>PR Deposition for Bottom Electrode Liftoff (Mask 1)</i>		
1.1	PR deposition	Z1/ACS 200	Recipe # 0171 (1.1 um AZ 1512, 0.48 um LOR). Dehydration step for 180 seconds, spin coating LOR 5A, soft baking at 190C for 250 seconds, spin coating AZ1512 HS, soft baking at 100C for 90 seconds
1.2	Exposure	Z5/MLA	70 mJ/cm2, -1, h-line
1.3	PR development	Z1/ACS 200	Recipe # 0971 once. Development contact time with AZ 726 MIF for 66 seconds, hard bake at 100C for 120 seconds.
1.4	Rinse wafers	Z1/Plade Solvent	rinse wafer in water bath to remove wafer backside residues, dry spinning step in SRD
1.5	Uscope analysis	Z1/uscope	Check if fully exposed and developed, measure dimensions
1.6	Check PR thickness	Z3/Nanospec	Si+ECI recipe
2	<i>Bottom Electrode Deposition</i>		
2.1	Bottom Electrode Sputtering	Z11/DP 650	Recipe: RTU_Mo, 37.3 seconds. Room temperature deposition.
3	<i>Liftoff for Bottom Electrode</i>		
3.1	Remover 1165 bath	Z1/Plade Solvent	Put in Remover 1165 bath
3.2	Spray Wafers	Z1/Plade Solvent	After 1-2 hours, spray the wafer front with Remover 1165 to help liftoff
3.3	Remover 1165 bath	Z1/Plade Solvent	Leave in Remover 1165 bath overnight
3.4	Spray Wafers	Z1/Plade Solvent	Spray wafer front with Remover 1165 before moving to ultrasound bath
3.5	Remover 1165 bath	Z1/Plade Solvent	5' wafer flat up, 5' wafer flat 90 degrees rotated
3.6	IPA bath	Z1/Plade Solvent	90" IPA bath
3.7	Wash in FFT	Z1/Plade Solvent	FFT water bath
3.8	SRD	Z1/Plade Solvent	Full SRD
3.9	Uscope	Z1/uscope	Check if liftoff is complete
3.10	Thickness Measurement	Z4/ Dektak	Measure bottom electrode thickness and fences
3.11	Measure resistance	By hand	Multimeter
3.12	SEM for fence images	Z1/Leo	Tilted SEM
4	<i>Dielectric and Top Electrode Deposition</i>		
4.1	ALD deposition	Z4/Beneq TFS200	Recipe: HfO2 200c 50nm LL. Chamber temperature is 200C and reactor temperature is 80C.
4.2	Thickness Measurement	Z3/Ellipsometer	Recipe g-75, a-45, 2pt
4.3	Stress Measurement	Z15/Toho	2x in 2 directions
4.4	Top Electrode Sputtering	Z11/DP 650	Recipe: RTU_Mo, 37.3 seconds. Room temperature deposition
4.5	Square Resistance Measurement	Z4/Omnimap	Pt Recipe
4.6	Stress Measurement	Z15/Toho	2x in 2 directions
5	<i>Top Electrode/Dielectric Etching Photolithography (Mask2)</i>		
5.1	PR deposition	Z1/ACS 200	Recipe # 0223 (1 um ECI, dehy, no EBR). Thermal dehydration before photoresist deposition
5.2	Exposure	Z5/MLA	150 mJ/cm2, -1, h-line, invert the mask

Figure A.4 – Runcard for asymmetric and symmetric thickness cross section fabrication

Appendix A. Appendix

5.3	PR development	Z1/ACS 200	Recipe # 0923, development contact time of 37 seconds
5.4	Rinse wafers	Z1/Plade Solvent	rinse with water hose, dry in SRD
5.5	Uscope analysis	Z1/uscope	Check if fully exposed and developed, measure dimensions
5.6	Descum	Z2/Tepla	O2 low 30"
5.7	Check PR thickness	Z3/Nanospec	Recipe 41
6	Top Electrode/Dielectric Etching		
6.1	Metal etching	Z2/STS	Wait one day after the photolithography and/or bake the wafers at low temperature for at least an hour. Prep etching chamber by etching dummy for 2'. Mo by W_etch: 52 nm/min. HfO2 by W_etch: 21 nm/min.
6.2	Check metal etching	Z2/Multimeter	Check by hand 2-3 places.
6.3	Measure PR thickness	Z3/Nanospec	Recipe 41
6.4	Ellipsometer	Z4/Ellipsometer	Recipe g-75, a-45, 2pt
6.5	Check results in uscope		Confirm Mo removed
6.6	Dielectric etching	Z2/Plade Oxide	HF 49%:H2O 1:4 bath (10% HF), HfO2 etch rate 66 nm/min
6.7	Check dielectric etching	Z2/multimeter	Check by hand 2-3 places.
6.8	Measure SiO2 thickness	Z3/Nanospec	Si+SiO2 recipe
6.9	Check results in uscope		Check that HfO2 is removed
6.10	PR stripping	Z2/UFT Resist and Z2/Tepla	30" high Tepla + normal 1165 bath + 30" high Tepla
6.11	Check results in uscope		Check that PR is removed
6.12	Profilometer	Z4/Dektak	Measure top electrode+dielectric and bottom electrode thicknesses
7	PR Deposition for Pad Liftoff (Mask 3)		
7.1	PR deposition	Z1/ACS 200	Recipe # 0171 (1.1 um AZ 1512, 0.48 um LOR). Dehydration step for 180 seconds, spin coating LOR 5A, soft baking at 190C for 250 seconds, spin coating AZ1512 HS, soft baking at 100C for 90 seconds
7.2	Exposure	Z5/MLA	70 mJ/cm2, -1, h-line
7.3	PR development	Z1/ACS 200	Recipe # 0971 twice. Development contact time with AZ 726 MIF for 66 seconds, hard bake at 100C for 120 seconds.
7.4	Rinse wafers	Z1/Plade Solvent	rinse wafer in water bath to remove wafer backside residues, dry spinning step in SRD
7.5	Uscope analysis	Z1/uscope	Check if fully exposed and developed, measure dimensions
7.6	Check PR thickness	Z3/Nanospec	Si+ECI recipe
8	Pad Deposition		
8.1	Pad Evaporation	Z11/EVA 760	250 _Al_160, dep rate 1.6 nm/s, 100 nm = 62.5"
9	Finish liftoff for pads		
9.1	Remover 1165 bath	Z1/Plade Solvent	Put in Remover 1165 bath
9.2	Spray Wafers	Z1/Plade Solvent	After 1-2 hours, spray the wafer front with Remover 1165 to help liftoff
9.3	Remover 1165 bath	Z1/Plade Solvent	Leave in Remover 1165 bath overnight
9.4	Spray Wafers	Z1/Plade Solvent	Spray wafer front with Remover 1165 before moving to ultrasound bath
9.5	Remover 1165 bath	Z1/Plade Solvent	5' wafer flat up, 5' wafer flat 90 degrees rotated
9.6	IPA bath	Z1/Plade Solvent	90" IPA bath
9.7	Wash in FFT	Z1/Plade Solvent	FFT water bath
9.8	SRD	Z1/Plade Solvent	Full SRD
9.9	Uscope	Z1/uscope	Check if liftoff is complete

Figure A.5 – Runcard for asymmetric and symmetric thickness cross section fabrication

A.7 Wafer Level Mask Design

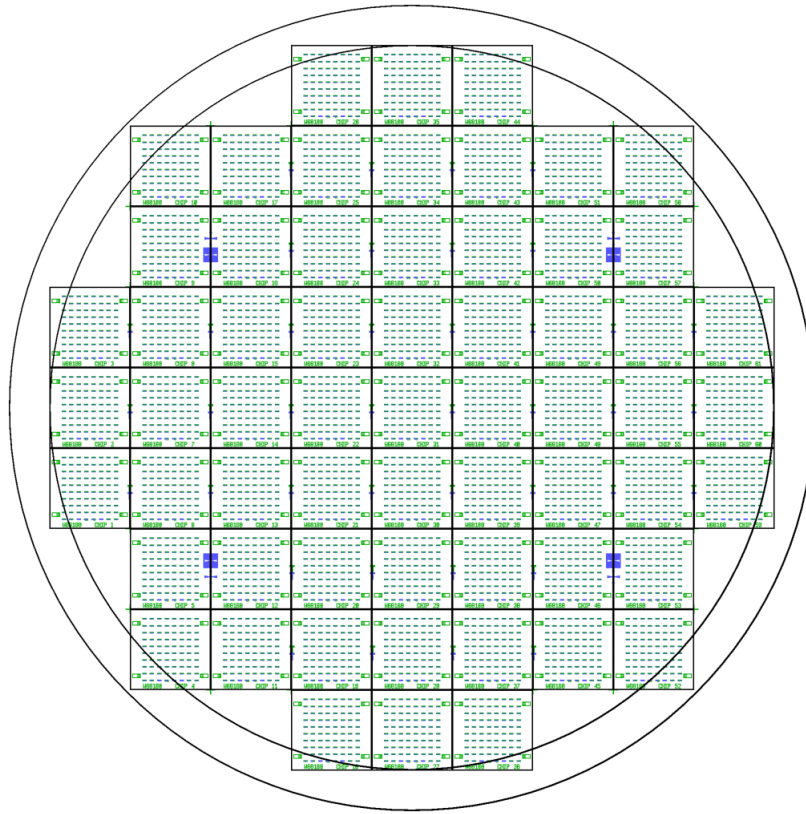


Figure A.6 – Wafer level mask design for asymmetric and symmetric beam cross section fabrication. The bottom electrode layer is in purple, the top electrode and HfO_2 layers in green. Sixty-one chips were patterned on each wafer and labeled with the wafer and chip number in the second photolithography step.

A.8 Supplementary SEM Electrode Images from Flexoelectric Actuator Fabrication

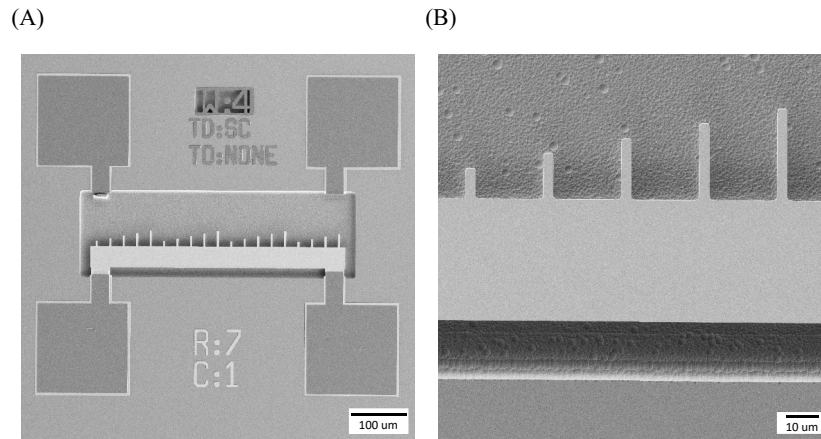


Figure A.7 – (A) Normal SEM image of an electrode with released cantilevers on Chip 3a. The electrode pads (dark squares) below the beam support are used for IV characterization and wire bonding. (B) Close up SEM image on the five cantilevers lengths fabricated on all the processed chips.

A.9 Supplementary Data on DC Measurements

Table A.1 – Resistance and standard deviation of top and bottom electrodes before and after vapor HF release (Chip 7, Run 1) or before and after chip level fabrication (Chips 43, Run 2 and 32, Run 3). Measurements were taken with DC probes in air. The resistance in the top and bottom electrodes either increases after fabrication or stays approximately the same.

Chip	Before (Ω)	STD (Ω)	After (Ω)	STD (Ω)
Top Electrode				
1s	70	28	86	37
2s	49	1.3	63	25
2a	29	0.8	35	0.1
3a	34	1.3	32	12
Bottom Electrode				
1s	79	32	74	25
2s	39	1.3	55	18
2a	36	0.5	45	3
3a	60	25	57	0.02

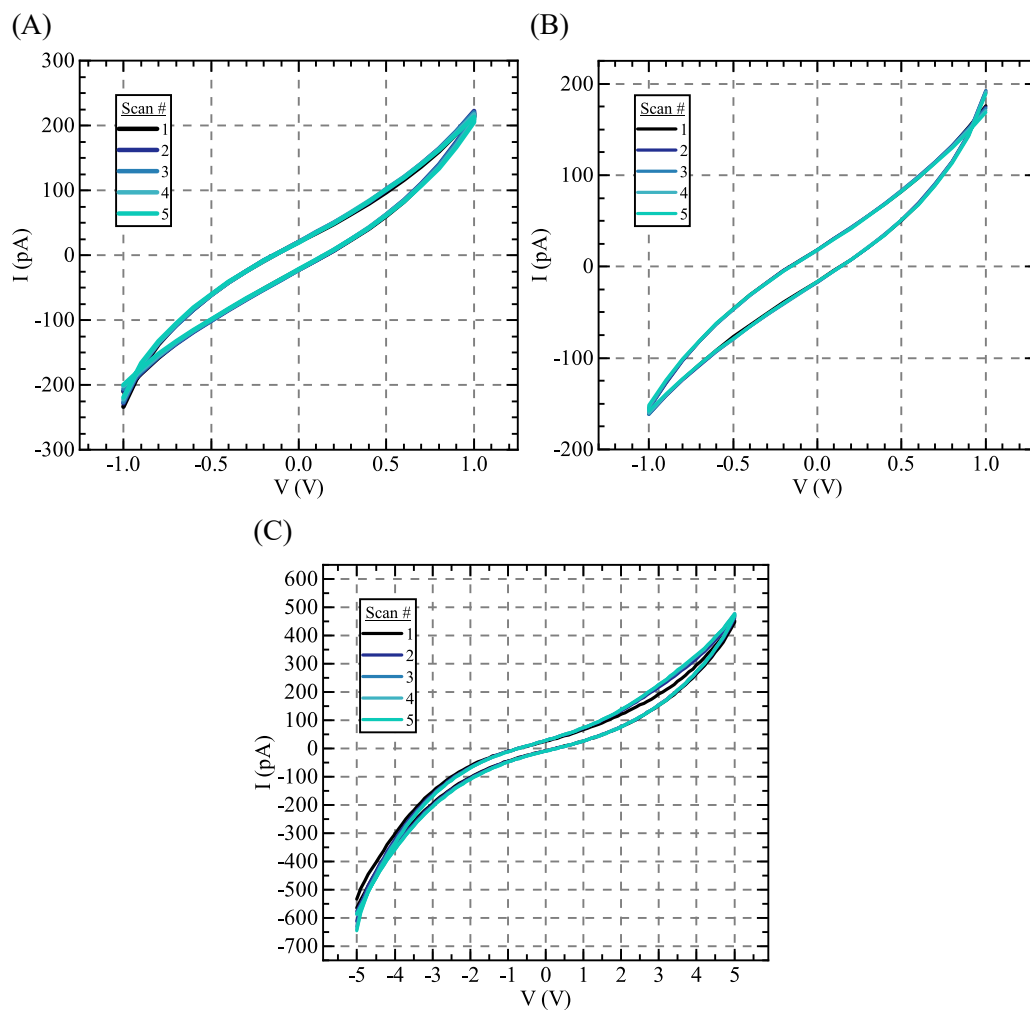


Figure A.8 – (A) Five repeated IV sweeps from -1 to +1 V and back using DC probes. (B) Five repeated IV sweeps from +1 to -1 V and back. (C) Five repeated IV sweeps from -5 to +5 V and back.

A.10 Theta2theta Curves of HfO₂ on Si Substrates and Pt-Coated Substrates

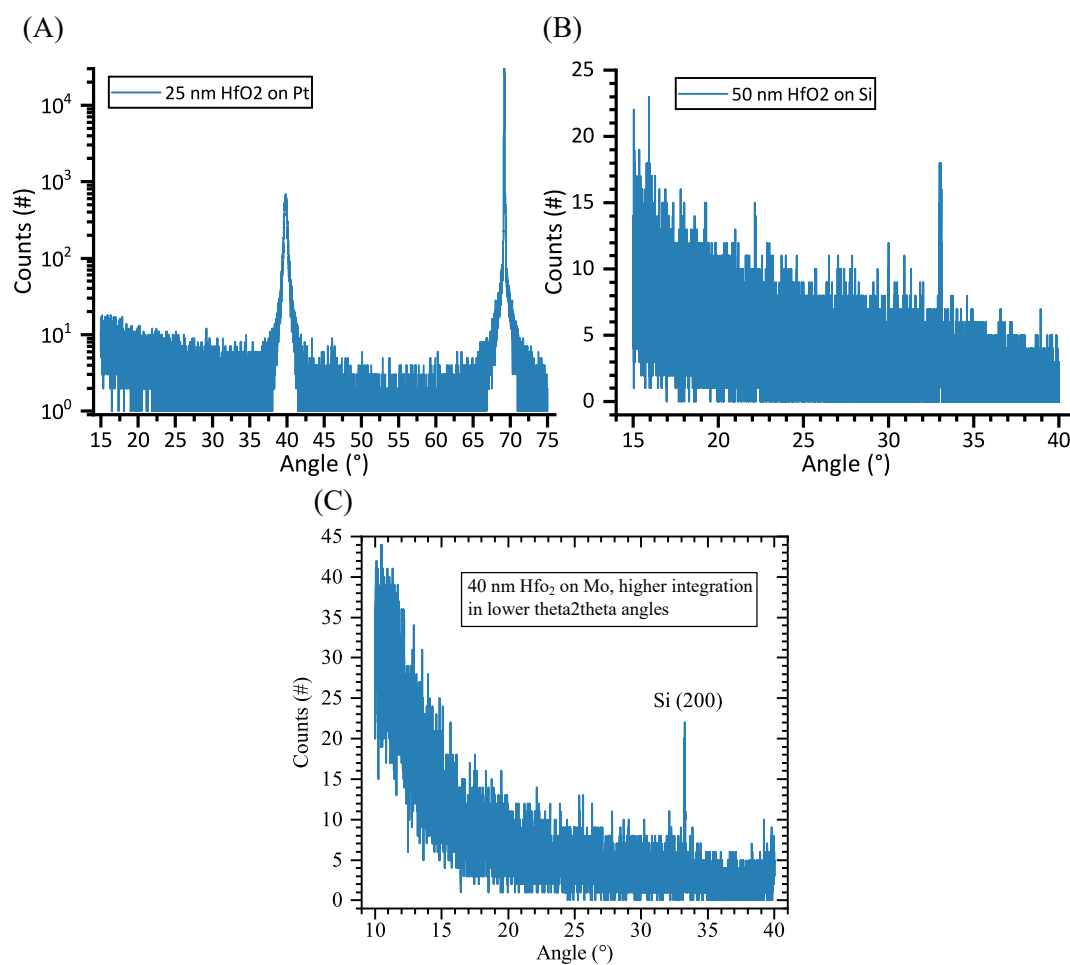


Figure A.9 – (A) Theta2theta curve of 25 nm HfO₂ on a Pt-coated Si substrate. Only peaks from Pt (40°) and Si (69°) are visible. (B) Higher integration theta2theta curve of 25 nm HfO₂ on a bare Si substrate. Only a forbidden Si peak is visible. (C) Higher integration theta2theta curve of 40 nm HfO₂ on a Mo-coated Si substrate. Only a forbidden Si peak is visible.

A.11 Designed versus Measured Cantilever Lengths

Table A.2 – Designed and measured cantilever lengths on Chips 1s, 2s, 2a and 3a by analyzing top view SEM images in ImageJ. Chips 1s and 2s have a symmetric thickness cross section, while Chips 2a and 3a have an asymmetric cross section. The lengths were measured by analyzing the top view SEM images in ImageJ.

SC Designed Lengths μm	Chip 1s μm	Chip 2s μm	Chip 2a μm	Chip 3a μm
10	9.6	10.0	9.8	10.0
15	14.5	15.0	14.9	15.1
20	19.5	19.9	19.9	19.8
25	25.4	24.9	24.8	24.6
30	30.4	29.9	29.6	29.2

A.12 Designed versus Effective Cantilever Lengths

Table A.3 – Designed and calculated cantilever lengths on Chips 1s, 2s, 2a, 3a and 3s using Comsol simulations of the resonance frequency shift. Chips 1s, 2s and 3s have a symmetric thickness cross section, while Chips 2a and 3a have an asymmetric cross section. Empty spaces mean that no cantilevers with that length were measured by the LDV.

SC Designed Lengths μm	Chip 1s μm	Chip 2s μm	Chip 2a μm	Chip 3a μm	Chip 3s
10	10.15	11.05	10.35	10.95	12.4
15	15.15	16.05	15.85	15.55	17.3
20	20.45	21.45	20.7	21.2	22.7
25	24.6	26.7	25.9	26.2	
30	30.4	31.85	31.15	31.25	

A.13 Expanded Flexoelectric and Effective Piezoelectric Coefficient Results

Table A.4 – Calculated flexoelectric (μ_{eff}) and effective piezoelectric coefficients (e_{eff}) based on a average of the individual surface fit results for all cantilevers with an asymmetric or symmetric thickness cross section as well as separately for each measured chip and electrode. The effective piezoelectric coefficient is shown as $e_{eff} \cdot Z_p$ as well as e_{eff} for easier comparison to μ_{eff} . STD stands for standard deviation, which is propagated from both the surface fit as well as the measurement error.

Cross Section	μ_{eff} (pC/m)	STD (pC/m)	$e_{eff} \cdot Z_p$ (pC/m)	STD (pC/m)	e_{eff} (mC/m ²)	adjR ²	Measured Beams #
Symmetric	29.5	10.7	-16.4	30.8	-17.0	0.99	65
Chip 1s	23.6	5.9	-25.5	16.8	-26.4	0.99	13
Electrode 1	18.4	4.0	-16.7	11.4	-17.3	0.98	7
Electrode 2	29.7	4.4	-35.8	12.3	-37.0	0.99	6
Chip 2s	28.3	7.4	-11.7	21.9	-12.1	0.99	45
Electrode 1	30.7	5.2	-15.6	17.0	-16.1	0.99	18
Electrode 2	26.7	5.2	-9.1	13.7	-9.4	0.99	27
Chip 3s	48.4	4.9	-30.0	13.8	-31.0	0.99	7
Asymmetric	41.3	7.4	-4.1	26.5	-0.6	1.00	47
Chip 2a	36.2	4.2	-11.1	23.1	-1.6	1.00	19
Electrode 1	36.3	2.7	-14.9	21.3	-2.1	1.00	12
Electrode 2	35.9	3.2	-4.6	9.0	-0.7	1.00	7
Chip 3a	44.8	6.0	0.6	12.9	0.1	1.00	28
Electrode 1	45.6	5.0	0.2	11.5	0.03	1.00	22
Electrode 2	42.0	3.4	1.8	5.9	0.3	0.99	6
Total average	37	13					105

A.14 Supplementary Data from Chapter 4 Flexoelectric Coefficient Analysis

Table A.5 – All flexoelectric coefficients taken/derived from literature for analysis on the relationship between the experimental flexoelectric coefficients and relative permittivity. Star indicates that value was digitally received from graphs within the literature.

Material	Crystallinity	Phase	μ_{12} or μ_{13} (nC/m)	ϵ_r	Reference
PMN-34PT	single crystal	near temperature of maximum relative permittivity	36,400	33000	[212]
PMN-34PT	single crystal	paraelectric, above polar region temperature	4,700	3000	[212]
PMN-28PT	single crystal	near temperature of maximum relative permittivity	37,200	35000	[212]
PMN-28PT	single crystal	paraelectric, above polar region temperature	2,100	6300	[212]
PMN	ceramic	near temperature of maximum relative permittivity	4,400	12700	[208]
PMN	ceramic	paraelectric	310	1960	[208]
BST/ZNO	ceramic composite	near curie temperature	128,600	41400	[214]
BST/ZNO	ceramic composite	paraelectric	170	700	[256]
BST	ceramic	near curie temperature	96000	16400	[209]
BST	ceramic	paraelectric	650	1700	[209]
BST	ceramic	near curie temperature	8500	4100	[179]
BTO	ceramic	near curie temperature	43200	10200	[207]
BTO	ceramic	paraelectric	7770	2950	[207]
BTO	(001) single crystal	near curie temperature	25400	14000	[192]
BTO	(001) single crystal	paraelectric	200	1500	[192]
BTO	(110) single crystal	near curie temperature	109000	13000	[192]
BTO	(110) single crystal	paraelectric	50*	1500	[192]
BTO	(111) single crystal	near curie temperature	101000	13000	[192]
BTO	(111) single crystal	paraelectric	10*	1500	[192]
PZT-5H	ceramic	ferroelectric, unpoled	9600	11000	[210]
PZT-5H	ceramic	paraelectric	1000	2700	[210]
TiO2	(110) single crystal	dielectric	1.5	110	[193]
STO	single crystal	paraelectric	7	300	[198]
STO	single crystal	paraelectric	4.1	75	[16]

A.15 Supplementary Data from Chapter 4 Flexoelectric Coefficient Analysis

	Influence of constant definition on γ value			
	$c = e/4 \pi a$		$c = e/a$	
Relative Permittivity Range	Gamma (10^{-3})	Error (10^{-3})	Gamma (E-4)	Error (E-4)
All, with HfO2	2.0	0.1	1.6	0.1
All, without HfO2	2.5	0.1	2.0	0.1
Low, with HfO2	2.6	0.1	2.1	0.1
Low, without HfO2	3.8	0.3	3.1	0.3
High	7.5E+04	2.0E+04	6.0E+03	1.6E+03

Linear Fitting Results	Slope (E-9)	Error (E-9)	Intercept (E-6)	Error (E-6)	AdjR2
All, with HfO2	2.3	0.5	3.3	7.7	0.44
All, without HfO2	2.3	0.5	3.5	9.1	0.43
Low, with HfO2	0.7	0.3	-9.00E-03	0.8	0.18
Low, without HfO2	0.7	0.4	-9.00E-03	0.9	0.15
High	1.4	1.2	29.0	25	0.04

Figure A.10 – Influence of the constant definition in the power law fitting of the experimental flexoelectric coefficients versus relative permittivity. Linear fitting results for experimental flexoelectric coefficients versus relative permittivity.

A.16 Data from Chapter 4 Curvature Generation Analysis

Table A.6 – Comparison of flexoelectric and piezoelectric curvature generation for a given electric field with 10 nm thick electrode and actuation layers. All electrodes were Pt. The thickness of the actuation layer is denoted as t_A . The effective flexoelectric coefficient for TiO_2 was taken from [193]. In the case of our AlN thin films, a seed layer of 10 nm AlN was included in the calculation and the AlN e_{31} was an estimated value and therefore only the order of magnitude of the curvature generation should be taken into account.

Actuation Layer	t_A (nm)	$e_{31,eff}$ (C/m ²)	μ_{eff} (nC/m)	Curvature/ AC Drive (10 ⁺³ /Vm)
HfO ₂ (this work)	10		0.037	0.1
HfO ₂ (this work)	5		0.037	0.2
TiO ₂	10		1.5 [193]	4.0
TiO ₂	5		1.5 [193]	7.0
AlN (this work)	10	-1		5.2

Bibliography

- [1] K. L. Ekinici and M. L. Roukes, Rev. Sci. Instrum. **76**, 061101 (2005).
- [2] S. Schmid, L. G. Villanueva, and M. L. Roukes, *Fundamentals of Nanomechanical Resonators*, Springer International Publishing, Cham, 1 edition, 2016.
- [3] M. J. Madou, *Fundamentals of Microfabrication and Nanotechnology. Volume II Manufacturing Techniques for Microfabrication and Nanotechnology*, CRC Press Taylor & Francis Group, Boca Raton, Fl, USA, 3 edition, 2011.
- [4] B. Ilic, S. Krylov, K. Aubin, R. Reichenbach, and H. G. Craighead, Appl. Phys. Lett. **86**, 1 (2005).
- [5] I. Bargatin, I. Kozinsky, and M. L. Roukes, Appl. Phys. Lett. **90**, 1 (2007).
- [6] I. Bargatin, E. B. Myers, J. Arlett, B. Gudlewski, and M. L. Roukes, Appl. Phys. Lett. **86**, 1 (2005).
- [7] X. L. Feng, C. J. White, A. Hajimiri, and M. L. Roukes, Nat. Nanotechnol. **3**, 342 (2008).
- [8] P. A. Truitt, J. B. Hertzberg, C. C. Huang, K. L. Ekinici, and K. C. Schwab, Nano Lett. **7**, 120 (2007).
- [9] A. D. O'Connell et al., Nature **464**, 697 (2010).
- [10] G. Piazza, V. Felmetzger, P. Muralt, R. H. Olsson III, and R. Ruby, MRS Bull. **37**, 1051 (2012).
- [11] J. D. Adams et al., Appl. Phys. Lett. **83**, 3428 (2003).
- [12] S. C. Masmanidis et al., Science **317**, 780 (2007).
- [13] P. Ivaldi et al., J. Micromech. Microeng. **21**, 1 (2011).
- [14] D. L. DeVoe and A. P. Pisano, J. Microelectromech. S. **6**, 266 (1997).
- [15] L. E. Cross, J. Mater. Sci. **41**, 53 (2006).
- [16] U. K. Bhaskar et al., Nat. Nanotechnol. **11**, 263 (2016).

Bibliography

- [17] R. Ruby, The 'how & why' a deceptively simple acoustic resonator became the basis of a multi-billion dollar industry, in *2017 IEEE 30th Int. Conf. Micro Electro Mech. Syst.*, pages 308–313, Las Vegas, Nevada, USA, 2017, IEEE.
- [18] R. Ruby, P. Bradley, Y. Oshmyansky, A. Chien, and J. Larson, 2001 IEEE Ultrason. Symp. Proceedings. An Int. Symp. (Cat. No.01CH37263) **1**, 813 (2002).
- [19] Y. Lu and D. A. Horsley, *J. Microelectromech. S.* **24**, 1142 (2015).
- [20] J. F. Nye, *Physical properties of crystals : their representation by tensors and matrices*, Oxford science publications, Clarendon Press, Oxford, reprinted edition, 2004.
- [21] A. J. Moulson and J. M. Herbert, *Electroceramics*, John Wiley & Sons, Ltd, Chichester, UK, 2003.
- [22] T. Hanada, Basic Properties of ZnO, GaN, and Related Materials, in *Oxide Nitride Semicond. Adv. Mater. Res. vol 12*, edited by T. Yao and S.-K. Hong, pages 1–19, Springer, Berlin, Heidelberg, 2009.
- [23] H. Bhugra and G. Piazza, *Piezoelectric MEMS Resonators*, Microsystems and Nanosystems, Springer International Publishing, Cham, 2017.
- [24] D. Damjanovic, *Reports Prog. Phys.* **61**, 1267 (1998).
- [25] S. S. Gevorgian, A. K. Tagantsev, and A. K. Vorobiev, Dielectric, Mechanical, and Electrical Properties of Ferroelectrics and Piezoelectrics, in *Tuneable Film Bulk Acoust. Wave Reson.*, Engineering Materials and Processes, chapter 2, pages 17–54, Springer London, London, 2013.
- [26] P. Muralt, AlN Thin Film Processing and Basic Properties, in *Piezoelectric MEMS Reson.*, edited by H. Bhugra and G. Piazza, pages 3–37, Springer International Publishing, Cham, 2017.
- [27] *Nanoscale Res. Lett.* **7**, 1 (2012).
- [28] M. Dekkers et al., *J. Micromech. Microeng.* **23**, 025008 (2013).
- [29] S. H. Baek et al., *Science* **334**, 958 (2011).
- [30] P. Muralt et al., "Sensors Actuators, A Phys. **48**, 157 (1995).
- [31] E. Shahrabi et al., Chip-level CMOS co-integration of ReRAM-based non-volatile memories, in *2016 12th Conf. Ph.D. Res. Microelectron. Electron.*, pages 1–4, IEEE, 2016.
- [32] P. Muralt, M. Marzencki, B. Belgacem, F. Calame, and S. Basrour, *Procedia Chem.* **1**, 1191 (2009).
- [33] M.-A. Dubois and P. Muralt, *J. Appl. Phys.* **89**, 6389 (2001).

- [34] K. Tsubouchi, K. Sugai, and N. Mikoshiba, IEEE Trans. Sonics Ultrason. **32**, 634 (1985).
- [35] G. Carlotti, G. Socino, A. Petri, and E. Verona, Ultrason. Symp. Proc. , 295 (1987).
- [36] T. Ikeda, *Fundamentals of piezoelectricity*, Oxford University Press, 1996.
- [37] N. Ledermann et al., Sensors Actuat. A Phys. **105**, 162 (2003).
- [38] S. Gong, Lithium Niobate for M/NEMS Resonators, in *Piezoelectric MEMS Reson.*, edited by H. Bhugra and G. Piazza, chapter 4, pages 99–129, Springer International Publishing, Char, 2017.
- [39] Y. Ohmachi, K. Sawamoto, and H. Toyoda, Jpn. J. Appl. Phys. **6**, 1467 (1967).
- [40] P. Muralt, J. Micromech. Microeng. **10**, 136 (2000).
- [41] R. D. Vispute, H. Wu, and J. Narayan, Appl. Phys. Lett. **67**, 1549 (1995).
- [42] M. Ishihara, Vacuum **59**, 649 (2000).
- [43] H.-Y. Shih et al., Sci. Rep. **7**, 39717 (2017).
- [44] Y. Kim, M. S. Kim, H. J. Yun, S. Y. Ryu, and B. J. Choi, Ceram. Int. **44**, 17447 (2018).
- [45] J. D. MacKenzie et al., Appl. Phys. Lett. **67**, 253 (1995).
- [46] M.-A. Dubois, P. Muralt, and V. Plessky, BAW resonators based on aluminum nitride thin films, in *1999 IEEE Ultrason. Symp. Proceedings. Int. Symp. (Cat. No.99CH37027)*, volume 2, pages 907–910, Caesars Tahoe, NV, USA, 1999, IEEE.
- [47] M. J. Madou, Physical and Chemical Vapor Deposition—Thin Film Properties and Surface Micromachining, in *Fundam. Microfabr. nanotechnology. Vol. II, Manuf. Tech. Microfabr. Nanotechnol.*, chapter 7, pages 391–508, CRC Press Taylor & Francis Group, Boca Raton, FL, USA, 3 edition, 2011.
- [48] E. Alfonso, J. Olaya, and G. Cubillos, Thin Film Growth Through Sputtering Technique and Its Applications, in *Cryst. - Sci. Technol.*, InTech, 2012.
- [49] M. Ohring, Physical Vapor Deposition, in *Mater. Sci. Thin Film.*, chapter 7, pages 79–145, Elsevier, 1 edition, 1992.
- [50] S. Berg and T. Nyberg, Thin Solid Films **476**, 215 (2005).
- [51] B. A. Movchan and A. V. Demchishin, Phys. Met. Met. **28** (1969).
- [52] J. A. Thornton, J. Vac. Sci. Technol. **11**, 666 (1974).
- [53] R. Messier, A. P. Giri, and R. A. Roy, J. Vac. Sci. Technol. A **2**, 500 (1984).
- [54] E. Mirica, G. Kowach, and H. Du, Cryst. Growth Des. **4**, 157 (2004).

Bibliography

- [55] B. Cullity, *Elements of X-ray Diffraction*, ADDISON-WESLEY PUBLISHING COMPANY, Reading, 1978.
- [56] D. Bonnell, S. Kalinin, A. Kholkin, and A. Gruverman, *MRS Bull.* **34**, 648 (2009).
- [57] M. Ohring, Characterization of Thin Films, in *Mater. Sci. Thin Film.*, chapter 6, pages 249–305, Elsevier, 1 edition, 1992.
- [58] Measurement techniques for evaluating piezoelectric thin films, in *1996 IEEE Ultrason. Symp. Proc.*, volume 1, pages 235–242, IEEE, 1996.
- [59] M. Clement, J. Olivares, J. Capilla, J. Sangrador, and E. Iborra, *IEEE Trans. Ultrason. Ferroelectr. Freq. Control* **59**, 128 (2012).
- [60] J. Capilla, M. Clement, J. Olivares, J. Sangrador, and E. Iborra, Influence of AlN quality on the transverse and longitudinal coupling coefficients of acoustic devices, in *2009 IEEE Int. Ultrason. Symp.*, pages 2174–2177, Rome, Italy, 2009, IEEE.
- [61] F. Martin, P. Muralt, M.-A. Dubois, and A. Pezous, *J. Vac. Sci. Technol. A* **22**, 361 (2004).
- [62] E. Iborra et al., Assessment of the piezoelectric response of sputtered AlN films by x-ray diffraction, in *IEEE Ultrason. Symp. 2005.*, pages 1808–1811, Rotterdam, The Netherlands, 2005, IEEE.
- [63] A. L. Kholkin, C. Wüthrich, D. V. Taylor, and N. Setter, *Rev. Sci. Instrum.* **67**, 1935 (1996).
- [64] M.-A. Dubois and P. Muralt, *Sensors Actuat. A Phys.* **77**, 106 (1999).
- [65] J. Hernando et al., *J. Appl. Phys.* **104**, 1 (2008).
- [66] A. Mazzalai, D. Balma, N. Chidambaram, R. Matloub, and P. Muralt, *J. Microelectromech. S.* **24**, 831 (2015).
- [67] E. Iborra et al., *IEEE Trans. Ultrason. Ferroelectr. Freq. Control* **54**, 2367 (2007).
- [68] M. Rinaldi, C. Zuniga, Chengjie Zuo, and G. Piazza, *IEEE Trans. Ultrason. Ferroelectr. Freq. Control* **57**, 38 (2010).
- [69] M.-A. Dubois et al., *IEEE J. Solid-State Circuits* **41**, 7 (2006).
- [70] R. Olsson, K. Wojciechowski, M. Baker, M. Tuck, and J. Fleming, *J. Microelectromech. S.* **18**, 671 (2009).
- [71] A. De Pastina, D. Maillard, and L. G. Villanueva, *Microelectron. Eng.* **192**, 83 (2018).
- [72] Y. Lu, A. Heidari, and D. A. Horsley, *J. Microelectromech. S.* **24**, 904 (2015).
- [73] C. Cassella, Y. Hui, Z. Qian, G. Hummel, and M. Rinaldi, *J. Microelectromech. S.* **25**, 275 (2016).

-
- [74] A. Lozzi, A. De Pastina, E. T.-T. Yen, and L. G. Villanueva, *Appl. Phys. Lett.* **114**, 103502 (2019).
- [75] S. Trolier-McKinstry and P. Muralt, *J. Electroceramics* **12**, 7 (2004).
- [76] M. Gillinger, M. Schneider, A. Bittner, P. Nicolay, and U. Schmid, *J. Appl. Phys.* **117** (2015).
- [77] P. Muralt, *Integr. Ferroelectr.* **17**, 297 (1997).
- [78] P. Muralt, *J. Am. Ceram. Soc.* **91**, 1385 (2008).
- [79] A. Iqbal and F. Mohd-Yasin, *Sensors* **18**, 1797 (2018).
- [80] A. De Pastina and L. G. Villanueva, *J. Micromech. Microeng.* (2019).
- [81] C. C. Enz and A. Kaiser, *MEMS-based Circuits and Systems for Wireless Communication*, Integrated Circuits and Systems, Springer US, Boston, MA, 2013.
- [82] J. D. Larson et al., *Proc. IEEE Ultrason. Symp.* **1**, 869 (2000).
- [83] H. P. Löbl et al., *J. Eur. Ceram. Soc.* **21**, 2633 (2001).
- [84] G. Piazza, P. J. Stephanou, and A. P. (Al)Pisano, *J. Microelectromech. S.* **15**, 1406 (2006).
- [85] C. M. Lin et al., *Appl. Phys. Lett.* **97**, 1 (2010).
- [86] C. M. Lin, Y. Y. Chen, V. V. Felmetser, D. G. Senesky, and A. P. Pisano, *Adv. Mater.* **24**, 2722 (2012).
- [87] D. Horsley, A. Guedes, M.-H. Kiang, R. J. Przybyla, and S. Shelton, Miniature micromachined ultrasonic rangefinder, 2019, US Patent 10,324,181.
- [88] D. Horsley, A. Guedes, S. Shelton, and R. Przybyla, Piezoelectric micromachined ultrasonic transducers having stress relief features, 2019, US Patent App. 16/219,387.
- [89] X. Jiang et al., *Microsystems Nanoeng.* **3**, 17059 (2017).
- [90] V. M. Mastronardi et al., *Appl. Phys. Lett.* **106**, 13 (2015).
- [91] N. Sinha et al., *Appl. Phys. Lett.* **95**, 1 (2009).
- [92] U. Zaghloul and G. Piazza, *IEEE T. Electron Dev.* **61**, 3520 (2014).
- [93] U. Z. Heiba and G. Piazza, Piezoelectric nanoelectromechanical relays, 2017, US Patent App. 15/003,027.
- [94] R. Mahameed, N. Sinha, M. B. Pisani, and G. Piazza, *J. Micromech. Microeng.* **18** (2008).
- [95] M. D. Williams, B. A. Griffin, T. N. Reagan, J. R. Underbrink, and M. Sheplak, *J. Microelectromech. S.* **21**, 270 (2012).

Bibliography

- [96] M. a. Dubois, P. Muralt, H. Matsumoto, and V. Plessky, 1998 IEEE Ultrason. Symp. Proc. Cat No 98CH36102 **1**, 909 (1998).
- [97] H. Okano, Y. Takahashi, T. Tanaka, K. Shibata, and S. Nakano, Jpn. J. Appl. Phys. **31**, 3446 (1992).
- [98] G. F. Iriarte, J. G. Rodríguez, and F. Calle, Mater. Res. Bull. **45**, 1039 (2010).
- [99] Y. Fu et al., Prog. Mater. Sci. **89**, 31 (2017).
- [100] F. Engelmark et al., J. Vac. Sci. Technol. A **19**, 2664 (2001).
- [101] M. Akiyama, K. Nagao, N. Ueno, H. Tateyama, and T. Yamada, Vacuum **74**, 699 (2004).
- [102] M.-A. Dubois, P. Muralt, and L. Sagalowicz, Ferroelectrics **224**, 243 (1999).
- [103] F. Martin, P. Muralt, and M.-A. Dubois, J. Vac. Sci. Technol. A **24**, 946 (2006).
- [104] H. Lobl et al., Piezoelectric materials for BAW resonators and filters, in *2001 IEEE Ultrason. Symp. Proceedings. An Int. Symp. (Cat. No.01CH37263)*, volume 1, pages 807–811, IEEE, 2002.
- [105] J. B. Lee, J. P. Jung, M. H. Lee, and J. S. Park, Thin Solid Films **447-448**, 610 (2004).
- [106] S.-H. Lee, J.-K. Lee, and K. H. Yoon, J. Vac. Sci. Technol. A **21**, 1 (2003).
- [107] V. V. Felmetzger, P. N. Laptev, and S. M. Tanner, Crystal orientation and stress in AC reactively sputtered AlN films on Mo electrodes for electro-acoustic devices, in *Ultrason.*, pages 2146–2149, Beijing, China, 2008, IEEE.
- [108] A. Artieda, M. Barbieri, C. S. Sandu, and P. Muralt, J. Appl. Phys. **105** (2009).
- [109] K. H. Chiu, J. H. Chen, H. R. Chen, and R. S. Huang, Thin Solid Films **515**, 4819 (2007).
- [110] H.-C. Lee, J.-Y. Park, K.-H. Lee, and J.-U. Bu, J. Vac. Sci. Technol. B Microelectron. Nanom. Struct. **22**, 1127 (2004).
- [111] M. Akiyama, N. Ueno, H. Tateyama, K. Nagao, and T. Yamada, J. Mater. Sci. **40**, 1159 (2005).
- [112] T. Kamohara, M. Akiyama, N. Ueno, K. Nonaka, and H. Tateyama, J. Cryst. Growth **275**, 383 (2005).
- [113] U. Zaghloul and G. Piazza, Proc. IEEE Micr. Elect. , 233 (2013).
- [114] U. Zaghloul and G. Piazza, Appl. Phys. Lett. **104**, 1 (2014).
- [115] K. M. Howell et al., J. Vac. Sci. Technol. A **37**, 021504 (2019).
- [116] J. C. Doll, B. C. Petzold, B. Ninan, R. Mullapudi, and B. L. Pruitt, J. Micromech. Microeng. **20** (2010).

-
- [117] E. Yarar et al., AIP Adv. **6**, 075115 (2016).
- [118] M. Akiyama, C.-N. Xu, K. Nonaka, K. Shobu, and T. Watanabe, Thin Solid Films **315**, 62 (1998).
- [119] G. F. Iriarte, F. Engelmark, and I. V. Katardjiev, J. Mater. Res. **17**, 1469 (2002).
- [120] W. J. Liu, S. J. Wu, C. M. Chen, Y. C. Lai, and C. H. Chuang, J. Cryst. Growth **276**, 525 (2005).
- [121] H. Jin et al., J. Electron. Mater. **41**, 1948 (2012).
- [122] A. Ababneh, U. Schmid, J. Hernando, J. Sánchez-Rojas, and H. Seidel, Mater. Sci. Eng. B **172**, 253 (2010).
- [123] A. Artieda, C. Sandu, and P. Muralt, J. Vac. Sci. Technol. A **28**, 390 (2010).
- [124] H. C. Lee and J. Y. Lee, J. Mater. Sci. Mater. Electron. **8**, 385 (1997).
- [125] E. Iborra et al., Sensors Actuat. A Phys. **115**, 501 (2004).
- [126] K. E. Knisely et al., J. Micromech. Microeng. **28**, 115009 (2018).
- [127] G. L. Huffman, D. E. Fahnline, R. Messier, and L. J. Pilione, J. Vac. Sci. Technol. A **7**, 2252 (1989).
- [128] A. Rodríguez-Navarro, W. Otaño-Rivera, J. M. García-Ruiz, R. Messier, and L. J. Pilione, J. Mater. Res. **12**, 1850 (1997).
- [129] V. V. Felmetzger, P. N. Laptev, and R. J. Graham, J. Vac. Sci. Technol. A **29**, 1 (2011).
- [130] H. Liu, F. Zeng, G. Tang, and F. Pan, Appl. Surf. Sci. **270**, 225 (2013).
- [131] J. T. Luo, B. Fan, F. Zeng, and F. Pan, J. Phys. D: Appl. Phys. **42** (2009).
- [132] M. Uehara et al., Appl. Phys. Lett. **111** (2017).
- [133] M. Akiyama et al., Adv. Mater. **21**, 593 (2009).
- [134] F. Tasnádi et al., Phys. Rev. Lett. **104** (2010).
- [135] R. Matloub, A. Artieda, C. Sandu, E. Milyutin, and P. Muralt, Appl. Phys. Lett. **99**, 97 (2011).
- [136] M. Moreira, J. Bjurström, I. Katardjev, and V. Yantchev, Vacuum **86**, 23 (2011).
- [137] K.-y. Y. Hashimoto, S. Sato, A. Teshigahara, T. Nakamura, and K. Kano, IEEE Trans. Ultrason. Ferroelectr. Freq. Control **60**, 637 (2013).
- [138] A. Konno et al., ScAlN Lamb wave resonator in GHz range released by XeF₂ etching, in *IEEE Int. Ultrason. Symp.*, pages 1378–1381, Prague, 2013.

Bibliography

- [139] F. Parsapour et al., Appl. Phys. Lett. **114**, 223103 (2019).
- [140] L. Colombo et al., Investigation of 20% Scandium-doped Aluminum Nitride films for MEMS laterally vibrating resonators, in *2017 IEEE Int. Ultrason. Symp.*, pages 1–1, Washington, DC, 2017, IEEE.
- [141] Z. A. Schaffer et al., Experimental investigation of damping factors in 20% scandium-doped aluminum nitride laterally vibrating resonators, in *2018 IEEE Micro Electro Mech. Syst.*, volume 2018-Janua, pages 787–790, IEEE, 2018.
- [142] A. Lozzi, E. Ting-Ta Yen, P. Muralt, and L. G. Villanueva, IEEE Trans. Ultrason. Ferroelectr. Freq. Control **66**, 146 (2019).
- [143] V. Pashchenko et al., Hybrid BAW/SAW AlN and AlScN thin film resonator, in *2016 IEEE Int. Ultrason. Symp.*, pages 1–4, Tours, France, 2016, IEEE.
- [144] Q. Wang, Y. Lu, S. Mishin, Y. Oshmyansky, and D. A. Horsley, J. Microelectromech. S. **26**, 1132 (2017).
- [145] Y. Kusano, G.-I. Luo, D. Horsley, I. taru Ishii, and A. Teshigahara, 36% Scandium-Doped Aluminum Nitride Piezoelectric Micromachined Ultrasonic Transducers, in *2018 IEEE Int. Ultrason. Symp.*, pages 1–4, IEEE, 2018.
- [146] P. Mayrhofer, E. Wistrela, M. Kucera, A. Bittner, and U. Schmid, Fabrication and characterisation of ScAlN -based piezoelectric MEMS cantilevers, in *2015 Transducers - 2015 18th Int. Conf. Solid-State Sensors, Actuators Microsystems*, pages 2144–2147, Anchorage, AK, USA, 2015, IEEE.
- [147] P. M. Mayrhofer et al., J. Microelectromech. S. **26**, 102 (2017).
- [148] V. Felmetger, Sputter technique for deposition of AlN and ScAlN thin films in mass production, in *IEEE Int. Ultrason. Symp.*, pages 1–1, Washington, DC, 2017.
- [149] M. Sinusía Lozano et al., Mater. Res. Express **5**, 036407 (2018).
- [150] V. V. Felmetger and P. N. Laptev, New generation of s-gun magnetron for aln reactive sputtering, in *The forth international symposium on acoustic wave devices for future mobile communication systems, Chiba, University, Japan*, pages 3–5, 2010.
- [151] V. Felmetger and P. Laptev, Vacuum **74**, 403 (2004).
- [152] S. Fichtner, T. Reimer, S. Chemnitz, F. Lofink, and B. Wagner, APL Mater. **3** (2015).
- [153] C. S. Sandu et al., Phys. Status Solidi **1800569**, 1 (2018).
- [154] M. Akiyama, K. Kano, and A. Teshigahara, Appl. Phys. Lett. **95**, 1 (2009).
- [155] M. AKIYAMA, T. TABARU, K. NISHIKUBO, A. TESHIGAHARA, and K. KANO, J. Ceram. Soc. Japan **118**, 1166 (2010).

-
- [156] M. Akiyama, K. Umeda, A. Honda, and T. Nagase, *Appl. Phys. Lett.* **102**, 0 (2013).
- [157] S. Barth et al., *Microsyst. Technol.* **22**, 1613 (2016).
- [158] O. Zywitzki, T. Modes, S. Barth, H. Bartzsch, and P. Frach, *Surf. Coatings Technol.* **309**, 417 (2017).
- [159] S. Mertin et al., Enhanced piezoelectric properties of c-axis textured aluminium scandium nitride thin films with high scandium content: Influence of intrinsic stress and sputtering parameters, in *IEEE Int. Ultrason. Symp.*, pages 1–4, Washington, DC, 2017.
- [160] S. Mertin et al., *Surf. Coatings Technol.* **343**, 2 (2018).
- [161] M. A. Caro et al., *J. Phys. Condens. Matter* **27**, 245901 (2015).
- [162] R. Matloub, M. Hadad, and P. Murait, 2016 IEEE Int. Freq. Control Symp. IFCS 2016 - Proc. , 2 (2016).
- [163] M. E. Parsapourkolour et al., *Ultrason.* , 5386 (2017).
- [164] S. Fichtner et al., *J. Appl. Phys.* **122**, 035301 (2017).
- [165] A. Zukauskaitė et al., *J. Appl. Phys.* **111**, 1 (2012).
- [166] J. C. Yang, X. Q. Meng, C. T. Yang, and Y. Zhang, *Appl. Surf. Sci.* **287**, 355 (2013).
- [167] P. Mayrhofer, H. Euchner, A. Bittner, and U. Schmid, *Sensors Actuat. A Phys.* **222**, 301 (2015).
- [168] P. M. Mayrhofer et al., *J. Appl. Phys.* **115** (2014).
- [169] Y. Zhang, W. Zhu, D. Zhou, Y. Yang, and C. Yang, *J. Mater. Sci. Mater. Electron.* **26**, 472 (2015).
- [170] Y. Lu et al., *Phys. status solidi* **215**, 1700559 (2018).
- [171] P. M. Mayrhofer, C. Eisenmenger-Sittner, H. Euchner, A. Bittner, and U. Schmid, *Appl. Phys. Lett.* **103** (2013).
- [172] R. B. Karabalin et al., *Appl. Phys. Lett.* **95**, 1 (2009).
- [173] C. Lee, F. Placido, S. Cochran, and K. Kirk, Growth of sputtered AlN thin film on glass in room temperature, in *2002 IEEE Ultrason. Symp. 2002. Proceedings.*, volume 2, pages 1119–1122, IEEE, 2002.
- [174] P. V. Yudin and A. K. Tagantsev, *Nanotechnology* **24** (2013).
- [175] A. K. Tagantsev and A. S. Yurkov, *J. Appl. Phys.* **112** (2012).
- [176] A. Kumar, A. Sharma, R. Vaish, R. Kumar, and S. Chandra, *Appl. Phys. A-Mater.* **0**, 0 (2018).

Bibliography

- [177] A. Yurkov, A. Dejneka, and P. Yudin, *Int. J. Solids Struct.* **162**, 96 (2019).
- [178] W. Huang et al., *Appl. Phys. Lett.* **101**, 252903 (2012).
- [179] W. Huang, K. Kim, S. Zhang, F.-G. Yuan, and X. Jiang, *Phys. status solidi - Rapid Res. Lett.* **5**, 350 (2011).
- [180] S. R. Kwon, W. B. Huang, S. J. Zhang, F. G. Yuan, and X. N. Jiang, *Smart Mater. Struct.* **22** (2013).
- [181] U. K. Bhaskar et al., *Nanoscale* **8**, 1293 (2016).
- [182] V. S. Mashkevich and K. B. Tolpygo, *Sov. Phys. - JETP* **5**, 435 (1957).
- [183] K. B. Tolpygo, *Sov. Phys. Solid State* **4**, 1297 (1963).
- [184] S. M. Kogan, *Sov. Phys.-Solid State* **5**, 2069 (1964).
- [185] V. Indenbom, E. Loginov, and M. Osipov, *Kristallografiy* **26**, 1157 (1981).
- [186] T. D. Nguyen, S. Mao, Y.-w. Yeh, P. K. Purohit, and M. C. McAlpine, *Adv. Mater.* **25**, 946 (2013).
- [187] X. Jiang, W. Huang, and S. Zhang, *Nano Energy* **2**, 1079 (2013).
- [188] A. K. Tagantsev, *Sov. Phys. - JETP* **61**, 1246 (1985).
- [189] A. K. Tagantsev, *Phys. Rev. B* **34**, 5883 (1986).
- [190] R. Resta, *Phys. Rev. Lett.* **105**, 127601 (2010).
- [191] S. Dai, M. Gharbi, P. Sharma, and H. S. Park, *J. Appl. Phys.* **110**, 104305 (2011).
- [192] J. Narvaez, S. Saremi, J. Hong, M. Stengel, and G. Catalan, *Phys. Rev. Lett.* **115**, 1 (2015).
- [193] J. Narvaez, F. Vasquez-Sancho, and G. Catalan, *Nature* **538**, 219 (2016).
- [194] A. K. Tagantsev, *Phase Transitions* **35**, 119 (1991).
- [195] R. Maranganti and P. Sharma, *Phys. Rev. B* **80**, 054109 (2009).
- [196] A. Askar, P. C. Y. Lee, and A. S. Cakmak, *Phys. Rev. B* **1**, 3525 (1970).
- [197] J. Hong, G. Catalan, J. F. Scott, and E. Artacho, *J. Phys. Condens. Matter* **22**, 112201 (2010).
- [198] P. Zubko, G. Catalan, A. Buckley, P. R. L. Welche, and J. F. Scott, *Phys. Rev. Lett.* **99**, 167601 (2007).
- [199] P. Zubko, G. Catalan, A. Buckley, P. R. L. Welche, and J. F. Scott, *Phys. Rev. Lett.* **100**, 199906 (2008).

-
- [200] J. Hong and D. Vanderbilt, Phys. Rev. B **84**, 180101 (2011).
- [201] L. Shu et al., J. Adv. Ceram. **8**, 153 (2019).
- [202] P. Zubko, G. Catalan, and A. K. Tagantsev, Annu. Rev. Mater. Res. **43**, 387 (2013).
- [203] B. Wang, Y. Gu, S. Zhang, and L.-q. Chen, Prog. Mater. Sci. **106**, 100570 (2019).
- [204] A. K. Tagantsev and P. V. Yudin, *Flexoelectricity in Solids*, WORLD SCIENTIFIC, 2016.
- [205] E. V. Bursian et al., Sov. Phys. Solid State **10**, 1121 (1968).
- [206] E. Bursian and N. Trunov, Sov. Phys. Solid State **16**, 760 (1974).
- [207] W. Ma and L. E. Cross, Appl. Phys. Lett. **88**, 232902 (2006).
- [208] W. Ma and L. E. Cross, Appl. Phys. Lett. **79**, 4420 (2001).
- [209] W. Ma and L. E. Cross, Appl. Phys. Lett. **81**, 3440 (2002).
- [210] W. Ma and L. E. Cross, Appl. Phys. Lett. **86**, 1 (2005).
- [211] P. Hana et al., Ferroelectrics **336**, 137 (2006).
- [212] J. Narvaez and G. Catalan, Appl. Phys. Lett. **104**, 78 (2014).
- [213] W. Ma and L. E. Cross, Appl. Phys. Lett. **78**, 2920 (2001).
- [214] Y. Li, L. Shu, W. Huang, X. Jiang, and H. Wang, Appl. Phys. Lett. **105**, 162906 (2014).
- [215] L. Shu et al., Appl. Phys. Lett. **102**, 0 (2013).
- [216] W. Ma and L. E. Cross, Appl. Phys. Lett. **82**, 3293 (2003).
- [217] W. Ma, Phys. Scr. **T129**, 180 (2007).
- [218] A. Biancoli, C. M. Fancher, J. L. Jones, and D. Damjanovic, Nat. Mater. **14**, 224 (2015).
- [219] S. Hashemizadeh, A. Biancoli, and D. Damjanovic, J. Appl. Phys. **119** (2016).
- [220] G. Catalan, L. J. Sinnamon, and J. M. Gregg, J. Phys. Condens. Matter **16**, 2253 (2004).
- [221] G. Catalan, B. Noheda, J. Mcaneney, L. J. Sinnamon, and J. M. Gregg, Phys. Rev. B - Condens. Matter Mater. Phys. **72**, 1 (2005).
- [222] A. Borisevich et al., Nat. Commun. **3**, 775 (2012).
- [223] G. Catalan et al., Nat. Mater. **10**, 963 (2011).
- [224] P. V. Yudin, A. K. Tagantsev, E. A. Eliseev, A. N. Morozovska, and N. Setter, Phys. Rev. B **86**, 134102 (2012).
- [225] V. Lyahovitskaya et al., Phys. Rev. B **71**, 094205 (2005).

Bibliography

- [226] M. S. Majdoub, R. Maranganti, and P. Sharma, *Phys. Rev. B* **79**, 115412 (2009).
- [227] H. Zhou et al., *Phys. B Condens. Matter* **407**, 3377 (2012).
- [228] A. N. Morozovska, E. A. Eliseev, M. D. Glinchuk, L.-q. Chen, and V. Gopalan, *Phys. Rev. B* **85**, 094107 (2012).
- [229] M. S. Majdoub, P. Sharma, and T. Cagin, *Phys. Rev. B* **77**, 125424 (2008).
- [230] D. Lee et al., *Phys. Rev. Lett.* **107**, 057602 (2011).
- [231] Z. Wang et al., *Adv. Funct. Mater.* **23**, 124 (2013).
- [232] M. Gharbi, Z. H. Sun, P. Sharma, and K. White, *Appl. Phys. Lett.* **95**, 142901 (2009).
- [233] M. Gharbi, Z. Sun, P. Sharma, K. White, and S. El-Borgi, *Int. J. Solids Struct.* **48**, 249 (2011).
- [234] C. R. Robinson, K. W. White, and P. Sharma, *Appl. Phys. Lett.* **101**, 122901 (2012).
- [235] S. R. Kwon et al., *Appl. Phys. Lett.* **105** (2014).
- [236] S. Huang et al., *Appl. Phys. Lett.* **110**, 0 (2017).
- [237] L. Shu et al., *Appl. Phys. Lett.* **111** (2017).
- [238] S. Huang et al., *AIP Adv.* **8**, 065321 (2018).
- [239] X. Wen, D. Li, K. Tan, Q. Deng, and S. Shen, *Phys. Rev. Lett.* **122**, 148001 (2019).
- [240] J. Y. Fu, W. Zhu, N. Li, and L. E. Cross, *J. Appl. Phys.* **100**, 024112 (2006).
- [241] L. Shu et al., *Appl. Phys. Lett.* **104**, 0 (2014).
- [242] P. Koirala, C. A. Mizzi, and L. D. Marks, *Nano Lett.* **18**, 3850 (2018).
- [243] J. Choi, Y. Mao, and J. Chang, *Mater. Sci. Eng. R Reports* **72**, 97 (2011).
- [244] P. Polakowski and J. Müller, *Appl. Phys. Lett.* **106**, 232905 (2015).
- [245] G. Franz, R. Kachel, and S. Sotier, *Mater. Sci. Semicond. Process.* **5**, 45 (2002).
- [246] L. Zheng, C. Lin, H. Xu, S. Zou, and M. Okuyama, *Sci. China, Ser. E Technol. Sci.* **40** (1997).
- [247] S. V. Kalinin and V. Meunier, *Phys. Rev. B* **77**, 033403 (2008).
- [248] C. Fuinel et al., High-K thin films as dielectric transducers for flexural M/NEMS resonators, in *2016 IEEE 29th Int. Conf. Micro Electro Mech. Syst.*, volume 2016-Febru, pages 1193–1196, IEEE, 2016.
- [249] J. Müller et al., *Nano Lett.* **12**, 4318 (2012).

- [250] M. Ohring, Mechanical Properties of Thin Films, in *Mater. Sci. Thin Film.*, pages 403–450, Elsevier, 1992.
- [251] O. Thomas, B. Legrand, and C. Fuinel, Optimization of Length and Thickness of Smart Transduction Layers on Beam Structures for Control and M/NEMS Applications, in *ASME 2015 Conf. Smart Mater. Adapt. Struct. Intell. Syst.*, page V001T03A008, Colorado Springs, CO, USA, 2015, American Society of Mechanical Engineers.
- [252] V. Sundar and R. Newnham, Electrostriction, in *Electr. Eng. Handb.*, edited by R. C. Dorf, chapter 50, CRC Press LLC, Boca Raton, 2 edition, 2000.
- [253] R. Yimnirun et al., Electr. Insul. Dielectr. Phenomena, 1998. Annu. Report. Conf. **1**, 240 (1998).
- [254] V. Sundar, J. F. Li, D. Viehland, and R. E. Newnham, Mater. Res. Bull. **31**, 555 (1996).
- [255] R. E. Newnham, V. Sundar, R. Yimnirun, J. Su, and Q. M. Zhang, J. Phys. Chem. B **101**, 10141 (1997).
- [256] Y. Li et al., Appl. Phys. Lett. **103**, 2 (2013).

Bibliography

Acronyms and Abbreviations

AC alternating current. 3, 72–76, 80

AFM atomic force microscopy. 7, 8

Al aluminum. 11, 12, 14, 17, 35, 40–43, 55, 56, 59, 60, 82

Al₂O₃ aluminum oxide. 53, 54, 86

ALD atomic layer deposition. 5, 53, 54, 58, 66

AlN aluminum nitride. xiii, 2, 4–22, 28, 29, 31–44, 46–48, 50, 51, 53, 81–83, 87–91, 115

AlScN aluminum scandium nitride. xiii, 2, 4, 7, 8, 16–22, 31, 33, 34, 43, 44, 46–51, 81–83, 91

Ar argon. 5–7, 13, 15, 19, 22, 31, 34–37, 40, 41, 44, 46–49, 51, 81, 82

Au gold. 12

BaTiO₃ barium titanate. 5, 24–27, 87

BAW bulk acoustic waves. 8, 17

BHF buffered hydrofluoric acid. 62, 63, 66

BST barium strontium titanate. 24, 26, 27

CLMR cross-sectional Lamé resonator. 10

CMOS complementary metal-oxide-semiconductor. 2, 5, 8, 16, 21, 28, 53, 54

CMR contour mode resonator. 8, 9, 17

Cr chromium. 16, 60

Cu copper. 12

DC direct current. 5, 6, 16, 18, 72–76, 79, 80

FBAR thin film bulk acoustic resonator. 9, 10, 16

Acronyms and Abbreviations

FWHM full width at half maximum. 8, 9, 11–15, 18, 19, 32, 33, 36–38, 40–42, 45, 46, 48–51, 81, 82

H₂O water. 58

HF hydrofluoric acid. 55, 56, 59–61, 64, 66, 69

Hf hafnium. 11

HfO₂ hafnium oxide. 2, 28, 29, 53–72, 76–81, 83–92

ICP inductively coupled plasma. 13, 50, 59, 61

IV current-voltage. 67, 68

LDV laser Doppler vibrometer. 8, 72–74, 76, 78, 79, 91

LVR laterally vibrating resonator. 17

MEMS microelectromechanical systems. 1–3, 9, 10, 17, 21, 88

MgNbAlN magnesium niobate-doped AlN. 16

Mo molybdenum. 12, 13, 15, 16, 18, 40–43, 55–66, 68–71, 80, 82–84, 88

N nitrogen. 6, 14–16, 19, 20, 34, 35, 46, 51

NEMS nanoelectromechanical systems. 1–3, 5, 9, 10, 28, 31, 35, 53, 83, 87, 88, 91

O oxygen. 6, 50, 59, 60, 62, 66, 67

PCB printed circuit board. 72

PFM piezoresponse force microscopy. 7, 8

PLD pulsed laser deposition. 5

PMN lead magnesium niobate. 5, 24, 25, 27, 84

PMN-PT lead magnesium niobate-lead titanate. 5, 25, 89

PMUT piezoelectric micromachined ultrasonic transducer. 10, 17

Pt platinum. 8, 9, 11–16, 18, 31, 32, 35–38, 41–44, 51, 55, 56, 60, 71, 72, 82, 88, 90

PVD physical vapor deposition. 5

PZT lead zirconate titanate. 5, 8, 24, 25, 53

- RF** radio frequency. 5, 6, 9, 10, 16, 17, 50
- SAW** surface acoustic waves. 8, 16, 17
- Sc** scandium. 16–21, 43, 44, 50, 51, 82, 91
- SEM** scanning electron microscopy. 7, 8, 20, 31, 33, 34, 44, 47–49, 51, 58, 62–67, 111
- Si** silicon. 8, 9, 11–13, 24, 31–33, 35, 36, 40, 55, 57, 58, 61, 62, 64–66, 71, 72, 77, 82
- Si₃N₄** silicon nitride. 88, 89
- SiO₂** silicon dioxide. 11, 18, 53–55, 57, 59, 61–66, 77, 84
- SMR** suspended microchannel resonator. 10
- SrTiO₃** strontium titanate. 2, 24, 25, 27, 28, 53, 87, 89
- SZM** structure zone model. 6, 7
- Ta** tantalum. 16
- TEM** transmission electron microscopy. 7, 8, 26
- Ti** titanium. 11–15, 37, 40–44, 50, 51, 55, 81, 82
- TiO₂** titanium dioxide. 26, 27, 53, 54, 56, 90, 91
- TMN** thermal mechanical noise. 72–74, 76
- XRD** X-ray diffraction. 7, 8, 20, 31, 33, 71, 72, 80, 83
- ZnO** zinc oxide. 4, 5, 7, 53, 89

Contributions to Doctoral Work

Researcher	Position	Contribution
Tom Larsen	Postdoctoral Researcher	First Matlab Codes for DC characterization
Damien Maillard	Doctoral Assistant	First Matlab Codes for LDV Experiments
Giulio de Vito	Intern	First Matlab Codes for LDV Experiments
Tamara Miteva	Semester Student	Assistance designing LDV measurements
Roman Welz	Semester Student	IV sweeps, Comsol simulations
Muhammad Faizan	Master Student	AlN depositions, characterization
Waqas Bashir	Doctoral Candidate	AlN depositions, characterization
Silvan Stettler	Semester Student	AlN depositions, characterization
Elliot Lauriere	Semester Student	AlScN depositions, characterization
Robin Nigon	Postdoctoral Researcher	AlScN depositions, characterization
		CV, PE measurements, XRD assistance

Photographic Credits

- Figure 1.1 B reprinted with permission from [22]
Copyright 2009 Springer Nature
- Figure 1.2 B from [48]
under Creative Commons Attribution 3.0 License
- Figure 1.3 A reprinted with permission from [61]
Copyright 2004 AIP Publishing
- Figure 1.3 B reprinted with permission from [62]
Copyright 2005 IEEE
- Figure 1.4 A reprinted with permission from [69]
Copyright 2006 IEEE
- Figure 1.4 B reprinted with permission from [68]
Copyright 2010 IEEE
- Figure 1.4 C reprinted with permission from [70]
Copyright 2009 IEEE
- Figure 1.4 D reprinted with permission from [71]
Copyright 2018 Elsevier
- Figure 1.4 E reprinted with permission from [72]
Copyright 2015 IEEE
- Figure 1.4 F reprinted with permission from [73]
Copyright 2016 IEEE
- Figure 1.4 G reprinted with permission from [74]
Copyright 2019 AIP Publishing
- Figure 1.5 A reprinted with permission from [147]
Copyright 2017 IEEE
- Figure 1.5 B reprinted with permission from [142]
Copyright 2019 IEEE
- Figure 1.5 C reprinted with permission from [140]
Copyright 2017 IEEE
- Figure 1.5 D reprinted with permission from [146]
Copyright 2015 IEEE
- Figure 1.5 E reprinted with permission from [144]
Copyright 2017 IEEE

Acronyms and Abbreviations

- Figure 1.5 F reprinted with permission from [139]
Copyright 2019 AIP Publishing
- Figure 1.6 A reprinted with permission from [164]
Copyright 2017 AIP Publishing
- Figure 1.6 B reprinted with permission from [170]
Copyright 2018 John Wiley and Sons
- Figure 2.3 A reprinted with permission from [115]
Copyright 2019 AIP Publishing
- Figures 2.4 A and B reprinted with permission from [115]
Copyright 2019 AIP Publishing

KAITLIN HOWELL

Avenue de Florissant 9
1008 Lausanne
Switzerland

📞 +41 78 691 6454

✉ khowell101918

✉ khowell2013@protonmail.com

in kaitlin-howell



- Microengineer with ISO 5 & 7 Experience
- Experience in Thin Film Deposition and Characterization
- Engaged in Academic Leadership and Project Supervision

EDUCATION

2015 – Present **École Polytechnique Fédérale de Lausanne (EPFL)**

– Doctoral Student in Microengineering

2013 – 2015 **École Polytechnique Fédérale de Lausanne (EPFL)**

– Master in Microengineering

– Specialization in Micro- and Nanosystems

2008 – 2012 **George Mason University**

– Double Bachelor in Physics and Astronomy

– Member of Honors College

CORE EXPERIENCE

2015 – Present **Advanced NEMS Group, EPFL, *Doctoral Thesis***

Investigation of piezoelectric and flexoelectric thin films for nanoscale actuation. Sputtering optimization of AlN and AlScN films to maximize texture and piezoelectric response. Fabrication of flexoelectric actuators to characterize effective flexoelectric coefficient of 40 nm amorphous HfO₂ films. Characterization techniques include x-ray diffraction, scanning electron microscopy, current-voltage sweeps and deformation measurements with a laser Doppler vibrometer. Potential application in electromechanical relays as alternative to CMOS technology

2013 **Detector Technologies (PH-DT) Group, CERN, *Internship* (3 months)**

Design of COMSOL Multiphysics® simulations to study the fracture mechanics of microchannels as well as experiments on fracture of microchannel cooling plates for silicon detectors. Work directly benefited the later installation of microchannel cooling in the NA62 Experiment.

2012 **UC Davis Neutrino Group, UC Davis, *Internship* (3 months)**

Design of simulation code in C++ to study the particle-material interactions in a germanium particle detector.

ADDITIONAL EXPERIENCE

- 2014 – 2015 **Advanced NEMS Group, EPFL, *Industrial-Based Master Thesis*** (6 months)
Design and simulation of novel outlets for microcolumn chips as part of a miniaturized gas analysis system based on micro-gas chromatography. Fabrication and characterization of microcolumn chips with four outlet geometries and SU-8 photoresist-based nozzles at gas outlets. Results show that output signal is directly related to gas velocity, which is dependent on the outlet geometry.
- 2011 **Detector Technologies (PH-DT) Group, CERN, *Internship*** (5 months)
Qualification of fabricated microchannels for cooling silicon detectors of the NA62 Experiment. Coordination of experimental development in a five-person team and optimization of data analysis. Work directly influenced the decision by NA62 Experiment to select microchannel cooling over other competitors.

LEADERSHIP EXPERIENCE

- 2016 – Present **PhD Representative**
– Doctoral Program in Microsystems and Microelectronics, EPFL
- 2016 – 2018 **Student Project Supervision**
– 1 Master Thesis
– 4 Semester Projects
– 1 Summer Internship
- 2012 **Advising Member**
– Dean's Student Advisory Board, College of Science, George Mason University
- 2010 – 2011 **President**
– Physics and Astronomy Club, George Mason University

AWARDS AND SCHOLARSHIPS

- 2013 – 2015 **Excellence Fellowship, EPFL**
- 2010 – 2012 **College of Science Leadership Scholarship, George Mason University**
- 2008 – 2012 **Academic Scholarship, George Mason University**

TECHNICAL SKILLS

Cleanroom Technologies

ISO 5 and ISO7 Cleanroom Experience

Thin Film Deposition

Magnetron Sputtering, E-Beam Evaporation, Atomic Layer Deposition (ALD)

Photolithography

Photoresist Spin Coating and Development, Mask and Laser Exposure

Etching

Plasma, Wet, Ion Beam, Vapor Phase

Techniques

Metal Liftoff, Anodic Bonding

Material Characterization

X-Ray Diffraction (XRD), Scanning Electron Microscopy (SEM), Ellipsometry, Optical Microscopy, Mechanical and Optical Profilometry

Experimental Characterization

Laser Doppler Vibrometry, Semiconductor Parameter Analyzer

IT

Matlab, COMSOL, Windows, MS Office, Python (Level 1: Fundamentals)

LANGUAGES

English	Native Language
French	Intermediate spoken and written B1 Certification
German	Basic spoken and written A0 Certification

EXTRACURRICULAR ACTIVITIES

Sports	Bouldering and Sport Climbing at Grade 6b, Road Biking
Group Activities	Snow Shoeing, Snowboarding, Escape Games, Laser Tag

PERSONAL DETAILS

Age	29
Civil Status	Married
Nationality	American

PUBLICATIONS

K. M. Howell, W. Bashir, A. De Pastina, R. Matloub, P. Murali, and L. G. Villanueva, "Effect of AlN seed layer on crystallographic characterization of piezoelectric AlN," *J. Vac. Sci. Technol. A*, vol. 37, p. 021504, mar 2019.

K. M. Howell, A. De Pastina, A. Lozzi, T. Larsen, M. Faizan, and L. G. Villanueva, "Piezoelectric nanoelectromechanical systems," in *TRANSDUCERS 2017 - 19th Int. Conf. Solid-State Sensors, Actuators Microsystems*, no. 1, pp. 151–154, 2017.

A. Mapelli, P. Petagna, K. M. Howell, G. Nuessle, and P. Renaud, "Microfluidic cooling for detectors and electronics," *J. Instrum.*, vol. 7, no. 1, 2012.